SISSA
Scuola
Internazionale
Superiore di
Studi Avanzati

Physics Area - PhD Course in
Physics and Chemistry of Biological Systems

Structure and Microrheology of Complex Polymer Solutions: from Genome Organization to Active-Passive Mixtures

Candidate:
Andrea PAPALE

Advisor:
Dr. Angelo ROSA

Academic Year 2018-2019

Contents

Introduction

Polymers are intriguing physical systems whose complex properties are at the heart of how viscoelastic substances, materials which under strain manifest a behavior which is intermediate between a liquid and a solid, work. Understanding the properties of these materials is the main goal of the theoretical and computational tools of Polymer Physics.

A particularly important, yet not fully understood, class of polymer materials is represented by concentrated solutions and melts of unknotted and unconcatenated ring polymers: in fact, at odds with the more familiar case of linear polymers which tend to become highly mixed and mutually penetrating, the presence of mutual avoidance and topological constraints (entanglements) between ring polymers force these chains to remain "territorial", i.e. each chain is virtually unmixed from the rest of the others. Because of this feature, solutions of ring polymers display unique material properties, in particular single chains tend to crumple into highly branched conformations and feature marked corrugated surfaces.

Recently, it has been suggested that the spatial configurations of ring polymers in solution can be used as model systems for the organization of chromosome conformations during *interphase*, i.e. inside the nuclei of eukaryotic cells. This surprising analogy is built upon the claim that chromosomes undergo slow relaxation inside the nucleus which results in the spontaneous formation of so-called *territories*, regions of the nucleus which have a profound impact on crucial cellular functions such as gene expression and gene regulation.

In this Thesis, we explore the analogy between ring polymers in solution, their large-scale crumpled 3d structure and interphase chromosomes by employing a combination of the theory of polymer solutions and numerical simulations.

In more detail, we investigate primarily the following aspects:

- The formation of ordered domains on a simple Ising-like toy model for crumpled polymers.

- The analysis of the viscoelastic properties of model chromosome conformations whose stochastic motion is restricted by the presence of external constraints.

- The discussion of the viscoelastic properties of solutions of active vs. non-active rings, where "active" means that polymers are driven out-of-equilibrium by pumping energy inside the system.

The Thesis is then organized as follows:

- In Chapter 1, we present a concise introduction to the fundamental concepts in Polymer Physics, starting from the statistics and scaling behavior of single polymer chains to the behavior of concentrated solutions and melts of linear and ring polymers.

- In Chapter 2, we introduce the relevant phenomenology of eukaryotic genomes. In particular we focus on their marked hierarchical organization, from the so-called topologically-associating domains (TAD's) to chromosome territories. Then we reconnect these aspects to the previous chapter, by highlighting in particular how salient features of chromosome conformations can be understood at the light of generic polymer models.

- In Chapter 3, inspired by previous theoretical and numerical efforts to model the formation of *epigenetic* patterns, we investigate the physics of a minimal polymer model where polymer conformations feature the presence of classical spins on each monomer and where local ordering is enforced by the standard Ising nearest-neighbor coupling.

- In Chapter 4, we introduce the principles of microrheology, a powerful experimental methodology to estimate viscoelastic properties of complex fluids. In particular, we discuss how microrheology can be employed in order to understand the dynamic behavior of entangled polymer solutions and melts.

- In Chapter 5, we apply microrheology in the context of the nuclei of the eukaryotic cells. In particular, we introduce a generic polymer model which takes into account the interactions between the chromatin fibers and the extra-chromosome structure known as the nucleoskeleton.

- In Chapter 6, we focus on a more general problem: namely we discuss an application of microrheology to investigate the viscoelastic properties of polymer melts constituted by a mixture of active (i.e., out-of-equilibrium) and non-active chains. To make the chapter self-consistent, we also provide a brief introduction to the topic of active matter by highlighting in particular its importance in the context of present-day Soft Matter Physics.

Finally, we finish the work by presenting the conclusions and highlighting perspectives for future work.

Chapter 1

General Principles of Polymer Physics

In this Chapter, we will present a concise introduction to Polymer Physics. To start with, we will introduce (section 1.1) fundamental concepts and related notation in order to describe the physics of polymers. Then, we will discuss the statistics and scaling behavior of single polymer chains and the behavior of concentrated solutions and melts of linear and ring polymers. To this purpose, we will mostly follow popular textbooks as [1, 2].

1.1 Introduction to Polymer Physics

1.1.1 Language and Notation

A polymer is a complex structure composed by many simple units, called monomers. Each monomer is connected to its neighbors by a bond. Here, we will consider a simple polymer chain of $N+1$ monomers with positions $\vec{r}_i$, $i \in [0, N]$ and relative distances $\vec{b}_i = \vec{r}_i - \vec{r}_{i-1}$. The main features of a polymer chain can be described using several parameters which we are going to define.

- The contour length, L_c, is defined as the distance along the chain from one end to the other.

- The mean-square end-to-end distance, $\langle \vec{R}_{ee} \rangle$, measures the average size and compactness of the polymer :

$$\langle \vec{R}_{ee}^2 \rangle = \langle (\vec{r}_N - \vec{r}_0)^2 \rangle = \langle (\sum_{i=1}^{N} \vec{b}_i)^2 \rangle = \sum_{i=1}^{N} \sum_{j=1}^{N} \langle \vec{b}_i \cdot \vec{b}_j \rangle.$$

- The Kuhn length, l_K, is a measure for the chain rigidity. It can be described as the shortest segment along the polymer backbone above which thermal fluctuations start bending the polymer significantly. Mathematically, it is

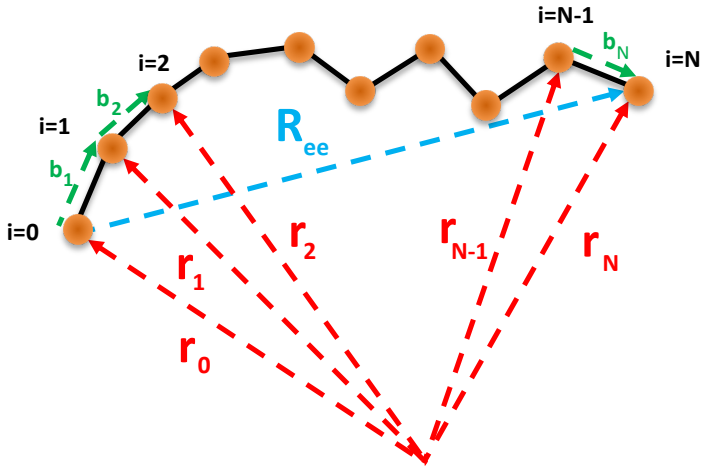

Figure 1.1: A schematic illustration of basic concepts of polymers. A chain is composed by $N+1$ monomers with positions $\vec{r}_i$, $i \in [0, N]$ connected by rigid joints of constant length b. The contour length is $L_c = b\,N$ while the end-to-end vector is $R_{ee} = \vec{r}_{N+1} - \vec{r}_0$ The bond vectors are defined as $\vec{b}_i = \vec{r}_i - \vec{r}_{i-1}$.

defined from the end-to-end vector:

$$l_K = \lim_{L_c \to \infty} \frac{\langle R_{ee}^2(L_c) \rangle}{L_c}. \tag{1.1}$$

- The mean-square radius of gyration, $\langle R_g^2 \rangle$, is another measure of the polymer size which accounts for the average (square) distance of each monomer from the polymer center of mass:

$$\langle R_g^2(N) \rangle = \frac{1}{N+1} \sum_{i=0}^{N} \langle (\vec{r}_i - \vec{R}_{cm})^2 \rangle$$

where $\vec{R}_{cm}$ is the center of mass $\vec{R}_{cm} = \frac{1}{N+1} \sum_{i=0}^{N} \vec{r}_i$.

- The persistence length, l_p gives a measure of the rigidity of a semi-flexible polymer chain. It corresponds to the typical length-scale of the orientation correlation along the polymer contour. Typically, the orientation correlation function decays exponentially along the chain [2] :

$$\langle \vec{t}(s) \cdot \vec{t}(s') \rangle = e^{-\frac{|s-s'|}{l_p}} \tag{1.2}$$

where $\vec{t}(s)$ is the tangent vector to the chain at contour length distance s.

1.1.2 Neglecting Excluded Volume: Ideal Polymers

There are different models describing the conformation of an ideal polymer. The simple model that can be imagined is the freely-jointed chain model (FJC), whose

configurations are realizations of a random walk. FJC assumes the absence of interactions between monomers with the exception of the bonding potential between neighbors. In this case, the distances, $\vec{b}_i$, have with fixed length b and the contour length L_c is simple their sum: $L_c = N\ b$. Since the relative orientations of monomers are uncorrelated, the mean square end-to-end vector is $\langle R_{ee}^2 \rangle = Nb^2 = L_c\ b$. Accordingly, the probability distribution function of the end-to-end vector is a Gaussian distribution with zero mean and variance Nb^2:

$$p_N(\vec{R}_{ee}) = \left(\frac{3}{2\pi N b^2}\right)^{\frac{3}{2}} exp\left(-\frac{3R_{ee}^2}{2Nb^2}\right). \tag{1.3}$$

Using equation 1.1, we find the Kuhn length l_K for a FJC:

$$l_K = \lim_{L_c \to \infty} \frac{\langle R_{ee}^2(L_c) \rangle}{L_c} = \lim_{L_c \to \infty} \frac{L_c\ b}{L_c} = b.$$

The fixed-bond constraint of the FJC model is overcome in the Gaussian Chain (GC) model, where a polymer chain is represented as a sequence of beads connected by harmonic springs. Consequently, the distance between two neighboring monomers is a Gaussian variable of zero mean and standard deviation b. The bond orientation is still uncorrelated from the other bonds: the resulting average mean-square end-to-end distance of a GC is the same obtained for a FJC, $\langle R_{ee}^2 \rangle = Nb^2$.

Ideal chain models, like FJC or the Gaussian model do not take into account the correlation between neighboring monomers. On the contrary, the correlation has been introduced in the worm-like chain (WLC) model: it describes a semi-flexible polymer chain as a continuous string of constant bending elasticity [3, 4]. The orientation correlation function decays exponentially along the chain as in equation 1.2 whose length-scale is the persistence length, l_p. For sufficiently long chains $L_c \gg l_p$, persistence length and Kuhn length are equivalent $l_K = 2l_p$. The mean square end-to-end vector for WLCs is

$$\langle R_{ee}^2(L_c) \rangle = 2l_p\ L_c \left[1 - \frac{l_p}{L_c}\left(1 - e^{-\frac{L_c}{l_p}}\right)\right]. \tag{1.4}$$

According to this relation, worm-like chain behaves as a rigid rod over short length scales ($\langle R_{ee}^2(L_c \ll l_p) \rangle \approx L_c^2$) and as ideal chains at large length scales ($\langle R_{ee}^2(L_c \gg l_p) \rangle \approx 2l_p L_c$).

1.1.3 Introducing Excluded Volume: Flory Theory

In real polymers, monomers occupy mutually avoiding, non-overlapping spatial positions. The physical consequences of self-avoidance between different monomers is that the polymer chain has an average size which turns to be much larger compared to the value estimated by using the theory for ideal chains (section 1.1.2). The inclusion of excluded volume effects in polymer models make them complicate from the mathematical point of view. For these reasons, here we resort to the mean-field-like Flory theory [2, 5, 6, 7] which, although approximate, provide remarkably

accurate predictions for the typical scaling behavior of the average size of polymers with excluded volume effects.

The equilibrium size of a real chain is the result of the balance between the effective excluded volume which tends to swell the chain, and a entropy loss for this variation. Flory theory considers a polymer chain with N monomers in a good solvent with typical size R: the monomers are uniformly distributed within a volume of size R^d, where d is the space dimensionality. For the seek of generality, we treat the problem for any $d > 0$. Correlations between monomers positions are neglected. Given a monomer, the probability of another monomer to be within its excluded volume v is product of the excluded volume v and the number density of the monomers in the initial volume. Consequently, its energetic cost is $k_B T v/R^d$ per monomer. Considering the entire chain composed by N monomers, the interaction free energy is

$$F_{int} \approx k_B T v \frac{N^2}{R^d}.$$

The theory considers the entropy computed to stretch an ideal chain to end-to-end distance R (see equation 1.3) [2].

$$F_{entropy} \approx k_B T \frac{R^2}{N l_k^2}.$$

Then, the resulting free energy of a real chain in the Flory theory is is the sum of its energetic interaction and its entropic free energy:

$$F = F_{int} + F_{entropy} \approx k_B T \left(v \frac{N^2}{R^d} + \frac{R^2}{N l_k^2} \right).$$

The minimum of the energy, set by the condition $\partial F/\partial R = 0$, corresponds to the typical size of the real chain $R = R_F$ according to Flory theory:

$$R_F^{d+2} \approx \frac{d}{2} v l_k^2 N^3.$$

The Flory theory leads to the a fundamental result: the typical size R_F has an universal power law dependence on the number of monomer N:

$$R_F \sim N^\nu$$

where $\nu = \frac{3}{d+2}$ is the Flory scaling exponent which characterizes polymer conformations. When $d = 3$, the scaling exponent is $\nu = 3/5$ for real chains while for ideal chains is $\nu = 1$. Comparing the last two cases and using the size of ideal chains $R_0 = l_k N^{1/2}$, the size R_F for a real chain in $d = 3$ results much larger:

$$\frac{R_F}{R_0} \approx \left(\frac{v}{l_k^3} N^{\frac{1}{2}} \right)^{1/5}.$$

The predictions of the Flory theory are in good agreement with other theories (e.g. renormalization group theory), experiments and simulations [8].

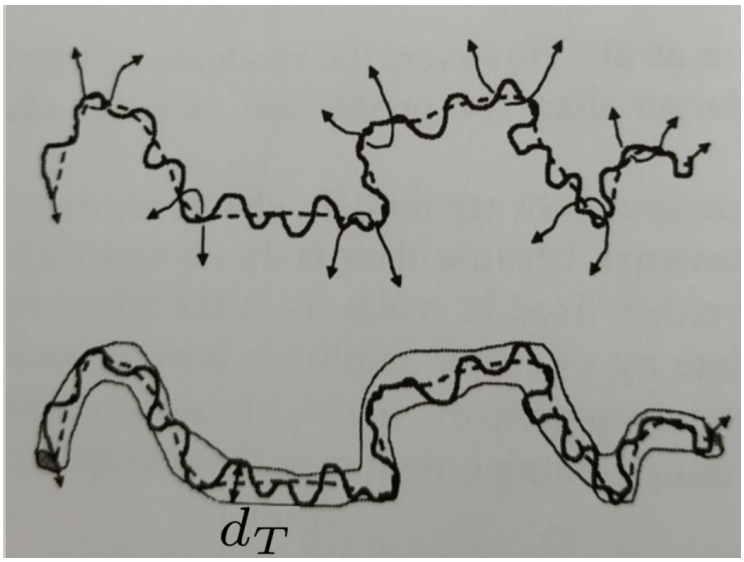

Figure 1.2: A schematic illustration of the concept of *primitive path* in the context of the Edwards tube model. Reproduced from reference [2].

1.1.4 Polymer Solutions of Linear Chains: Entanglements

So far, we have considered only the structural properties of single, isolated chains in good solvent conditions. A polymer solution is a system consisting of many polymer chains dissolved within the same solvent. If the concentration of the polymers is so high that the concentration of the solvent is negligible, then we have a so-called polymer melt. In both cases, the average volume spanned by a single chain is, in general, penetrated by the surrounding chains.

A theoretical description of polymer solutions or melts requires the contribution of many-body effects. Yet, as realized a long ago by Flory [2], intra-chain excluded volume interactions are effectively screened because of the presence of the other chains and single-chain statistics is well described as a random-walk with mean end-to-end distance $R_{ee} \sim N^{1/2}$.

Two chains that share the same volume are subject to topological constraints: the two chains cannot cross each other and their movements are severely restricted. These topological constraints are called *entanglements*. Edwards [1] showed that entanglements effects can be quantitatively described by assuming that chain dynamics is effectively constrained within a tube-like region which arises as due to the presence of the other chains (see figure 1.2). The center-line of the tube is the so-called *primitive path* of the chain: indeed, the chain is constrained to lie within a tube-like region whose center is the primitive path. Monomers can fluctuate in the direction perpendicular to the primitive path driven by the thermal energy k_BT. The balance between the constraints and thermal fluctuations sets the width of the confining tube, which is called *tube diameter* d_T. The tube diameter can be considered as the end-to-end distance of entanglement strand composed by N_e monomers

with a ideal chain statistics (since the excluded volume interactions are screened):

$$d_T \approx l_p N_e^{1/2}. \tag{1.5}$$

From this tube model, De Gennes [9] introduced the reptation model. According to his model, an entangled linear chain with N monomers can diffuse along their tube, analogously to the motion of a worm, which is characterized by a Rouse friction coefficient $N\gamma$. In particular, a chain composed by N_e monomers moves a distance of order of its own size R in a typical time

$$\tau_e \approx \frac{\gamma l_p^2}{k_B T} N_e^2 \tag{1.6}$$

with a diffusion coefficient:

$$D_{rep} \approx \frac{k_B T}{\gamma} \frac{N_e}{N} \tag{1.7}$$

1.1.5 Polymer Solutions of Unconcatenated and Unknotted Ring Polymers: the Physics of Crumpling

As seen so far, linear polymers in entangled solutions follow ideal statistics because of the screening of excluded volume at large scales [1, 10]. The effect of constraints on linear polymers is limited to slow down their dynamics and is a transient: polymer chains cannot cross through each other, they have to slowly slide past each other. The mechanism is different for melts of nonconcatenated unknotted ring polymers. Indeed, chain conformations have to respect global constraints requiring that all chains remain permanently unlinked and unknotted at the expense of entropic loss [11].

How physical quantities of a ring polymer, like its size, are affected by topological constraints is definitely nontrivial. When two rings interact, they will increasingly tend to repulse each other. The consequence is an entropic repulsion between the rings since the available conformations of the system decreases. Consequently, topological constraints between close-by rings induce chain conformations to fold into compact (*i.e.*, "territorial" [12]) structures which are reminiscent of the "crumpled" (or "fractal" [13]) globule [14, 15, 16, 17]. Recent numerical work of topologically constrained unconcatenated ring polymers in concentrated solutions and melts [18, 19, 20] has confirmed this feature and, thus, demonstrated that the typical end-to-end mean-square spatial distance between chain monomers with contour separation L_c is given by:

$$\langle R_{ee}^2(L_c)\rangle \approx \begin{cases} L_c^2\,, & L_c \lesssim \ell_K \\ \ell_K L_c\,, & \ell_K \lesssim L_c \lesssim L_e \\ \ell_K L_e \left(\frac{L_c}{L_e}\right)^{2/3}, & L_c \gtrsim L_e \end{cases} . \tag{1.8}$$

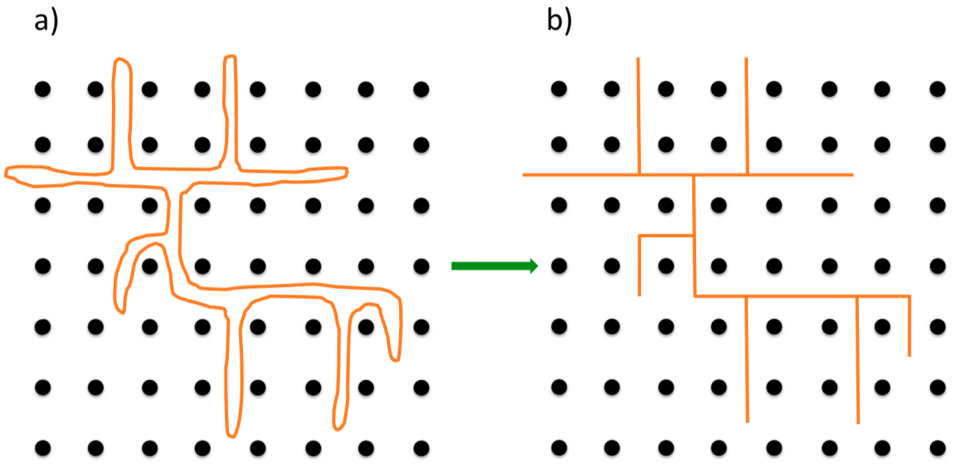

Figure 1.3: Schematic illustration of a two-dimensional ring (orange) in a matrix of impenetrable fixed obstacles (black dots). Ring reaches a transiently branched shape (a) to maximize the conformational entropy. It can be mapped in a lattice tree polymer (b) with annealed connectivity. Reproduced from reference [23].

ℓ_K is the Kuhn length of the polymer describing chain stiffness [2]. L_e, which depends on ℓ_K and solution density ρ [21, 22], is the so-called *entanglement* length marking the onset of entanglement effects. The corresponding end-to-end spatial distance between entanglement strands $d_T \approx (\ell_K L_e)^{1/2}$ (the "entanglement distance") is also called the "tube diameter" by analogy to systems of linear chains [1].

Among their noticeable features and in spite of compactness, rings do not expel close-by rings: on average in fact their surface remains "rough" and shares many contacts with neighbors [17, 20, 24, 25]. Indeed, rings interpenetrate as "threading" conformations [26, 27] similar to interacting "branched structures" [18] with long-range (loose) loops [28, 29]. This scenario has been largely investigated in the case of a ring polymer diffusing in a regular lattice of obstacles. In this situation, ring tents to maximize the entropy preserving its topological constraints despite the presence of obstacles. The ring forms self-similar randomly branched conformations of double-folded loops, which preserve its topology, and can be mapped in a lattice tree without loops [28, 30, 31], see figure 1.3.

Random tree models have been historically studied [32, 33] but exact results have been achieved only for the ideal case, non-interacting trees, where $R \sim N^{1/4}$. In particular, they are more compact if compared with ideal linear polymers, where $R \sim N^{1/2}$. As for the linear chain, random tree models including excluded volume interactions have not a simple solution. Only the self-avoiding tree model in $d = 3$ has been solved exactly [34] and the scaling exponent for the average tree size of $R \sim N^{\nu}$ is $\nu = 1/2$.

In general, random tree models have been investigated with several approaches, including scaling argument [35] and Flory theory [6, 8, 23]. The Flory theory approach has given useful insights [8], both for annealed, whose topology can change,

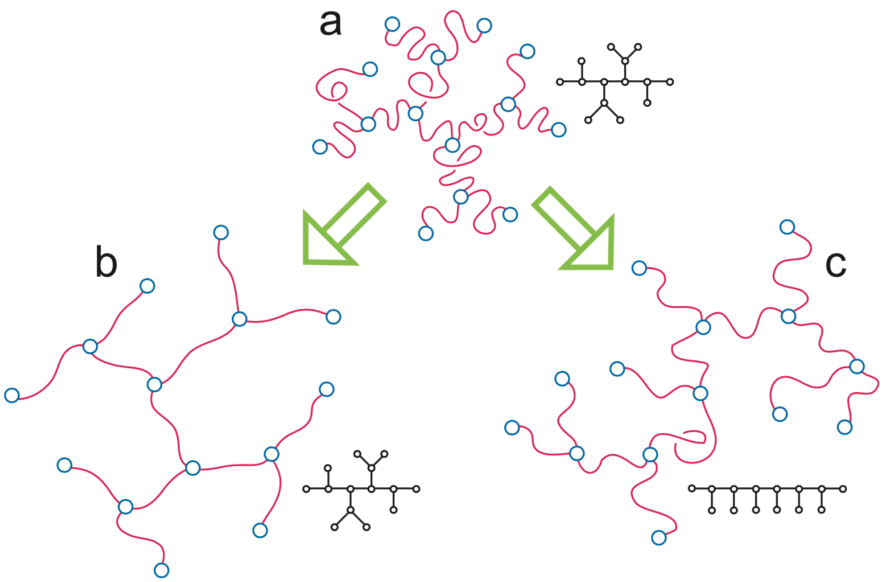

Figure 1.4: Schematic illustration of the two independent forms for interacting trees (a). (b) Quenched connectivity: the topology of the polymer is fixed. (c) With annealed connectivity: branching polymers can also modify their connectivity. Reproduce from reference [8].

and quenched, whose topology is fixed (see figure 1.4). The predictions of Flory theory have proved to be in agreement with the numerical investigations [23]. In particular, the asymptotic scaling of the average tree size, $R \sim N^{\nu}$, results $\nu = 1/d$, suggesting that the trees behave as compact, territorial fractals. Moreover, these results, compared to ideal trees, suggest that excluded volume interactions are only partially screened in melts of annealed trees [23].

Along this Thesis, we will investigate complex systems where the polymer models, which we have described in this chapter, can give interesting insights. In particular, we will focus on models developed for DNA arrangement and dynamics within the nuclei of eukariotic cells. Then, we will consider polymeric system in the context of active matter.

Chapter 2

Genome Organization: phenomenology and modeling

In this Chapter we provide an introduction to genome organization in the nucleus of eukaryotic cell: we will refer constantly to it in the course of this Thesis when we will compare theoretical models to experimental observations.

Firstly, we will begin by introducing the fundamental aspects of DNA. Then, we will focus on its local structure and on the hierarchical compartmentalization which have been observed within the nucleus during interphase [36, 37, 38, 39, 40, 41].

2.1 Nuclear Organization and Chromatin in Eukaryotic Cells

The cells of eukaryotes are partitioned into distinct compartments (see figure 2.1); each of them is dedicated to well-defined functions, and delimited by a single or double lipid layer membrane. The nucleus is one of these compartments: it consists of a roughly spherical region confined by a lipid bilayer, the *nuclear envelope*, which is externally connected to the cytoplasm, while its internal layer connects to the nuclear lamina. Importantly, the structure of the envelope helps the nucleus to sustain its shape. A fundamental role of the nucleus is to isolate the DNA double-helix from the rest of the cell and to protect it from physical and/or chemical damage.

Inside the nucleus, the genetic information carried by DNA is decoded and then post-processed to fulfill the cellular processes. In particular, the genome is organized into discrete functional units called *chromosomes*. Each chromosome consists of a single and long filament of double helix DNA associated with proteins devoted to fold and pack it into a more compact structure. In addition to the proteins involved in packaging the DNA, chromosomes are also associated with many proteins involved in the processes of gene expression, DNA replication, and DNA repair. The complex of DNA and proteins is called *chromatin* [42].

Traditionally, chromosomes are used to be depicted in the familiar X-shaped dense structure [43]. This peculiar configuration occurs only during the mitosis: indeed, a compact form is more suitable for transport inside the cytoplasm during

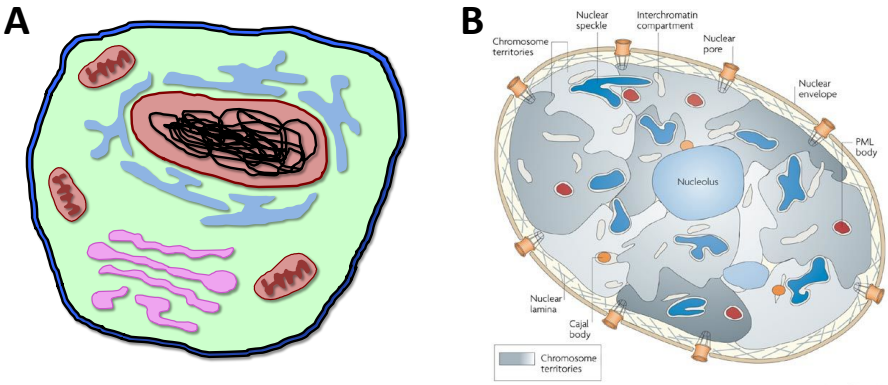

Figure 2.1: (A) Schematic representation of a typical eukaryotic cell organized in physically separated compartments. The nucleus, containing the DNA (the black rope), is localized in the cell's center. (B) Detailed representation of the nucleus: in its inside there exist regions void of chromatin ("interchromatin" compartments) and chromosomes condense into "territories". Moreover, a large collection of substructures is present including the nuclear lamina, nucleoli, PML and Cajal bodies, and nuclear speckles, and various components for transcription or repression are non-homogeneous distributed in the nucleoplasm. Reproduced from reference [36].

the duplication process. In contrast, the scenario changes significantly during the interphase, the longest stage in the eukaryotic cell cycle, when DNA needs to be locally accessible for transcription, replication or recombination: during this phase, in fact, chromosomes decondense from the compact mitotic form and swell inside the nucleus. However, an accurate understanding of the spatial organization of DNA in the nucleus during interphase is still lacking.

2.1.1 Genome Organization during Interphase

The correct expression of the genetic information encoded in the linear sequence of DNA is the result of appropriate folding of the double-helix inside the nucleus in order to accomplish their functional role [42]. In a typical human nucleus, about two meters (corresponding to $\approx 6 \times 10^9$ basepairs (bp)) of DNA are packed into distinct chromosomes, where each chromosome is made of a unique filament of chromatin fiber. Chromatin results from the association of the double-helix to specific protein complexes, called nucleosomes. A simple nucleosome is constituted of approximately 147bp of DNA wraped around the histone complex (an octamer protein complex made of two copies of each of the four core proteins, H2A, H2B, H3, H4) which extends in width for about 10nm and in thickness for about 6nm [46] (see figure 2.2, panel A). Consecutive nucleosomes are linearly connected into the so-called "10nm" fiber by $\approx$ 50bp of "linker" DNA [44]. Thereby, the typical distance between the centers of neighboring nucleosomes is the order of $\approx$ 25nm. The contour length density of the 10nm fiber is hence "200bp/(25nm) = 8bp/nm" which is ≈ 3 times more compact than bare DNA. In spite of the considerable experimental work

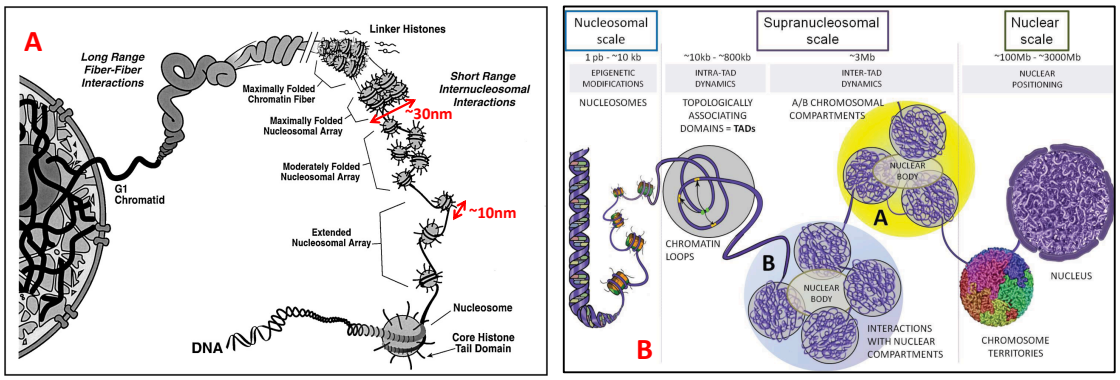

Figure 2.2: (A) Schematic illustration of DNA and chromatin fiber structure in nuclei of eukaryotic cells. The chromatin fiber originates from the wrapping of DNA around the nucleosome complex which produces the necklace-like structure known as the 10nm fiber, and the folding of 10nm fibers into 30nm fibers. The nature and very existence of the latter remains highly debated. (B) Hierarchical organization of chromatin structure, from the multi-megabase scale (Chromosome Territories, Lamina Associated Domains) to the kilobase scale (gene-enhancer loops and epigenetic clusters). Reproduced from reference [44] (panel A) and reference [45] (panel B).

of the last decades, there is little consensus concerning how chromatin folds above the 10nm fiber. In general, *in-vitro* studies of reconstituted nucleosomal arrays have pointed out the role of nucleosome-nucleosome interactions in mediating the formation of helical-like structures with diameter in the range $30 - 40$nm and a contour length density of $\approx$ 100bp/nm, *i.e.* $\approx 30\times$ more compact than bare DNA [44]. This so-called "30nm" fiber has been proposed as an essential element of the three-dimensional structures of interphase and mitotic chromosomes *in-vivo*. Yet, its true existence remains highly controversial.

In fact, recent experimental studies by Maeshima and coworkers based on small-angle X-ray scattering (SAXS) on HeLa cells [47] in combination with computational modeling essentially detected no structural features beyond the 10nm fiber. Based on these results, the same authors proposed [48] then an alternative model where chromosomes in interphase nuclei look like an interdigitated polymer melt of nucleosome fibers lacking the 30nm chromatin structure. Very recently, these results have been substantially confirmed by chromEMT [49], a novel high-resolution experimental technique combining electron microscopy tomography (EMT) with a labeling method (ChromEM) that selectivity enhances the contrast of DNA. ChromEMT supports the picture where chromatin fibers form disordered structures packed together at different concentrations in the nucleus. Interestingly, although chromatin compaction is locally changing in time, measurements of density fluctuations at high-resolution reveal that nuclear chromatin behaves like a compact and dynamically "stable" *fractal* medium [50].

During the observation of living cells, chromatin conformation is highly variable between different cells, but it is not randomly organized. Indeed, ordered

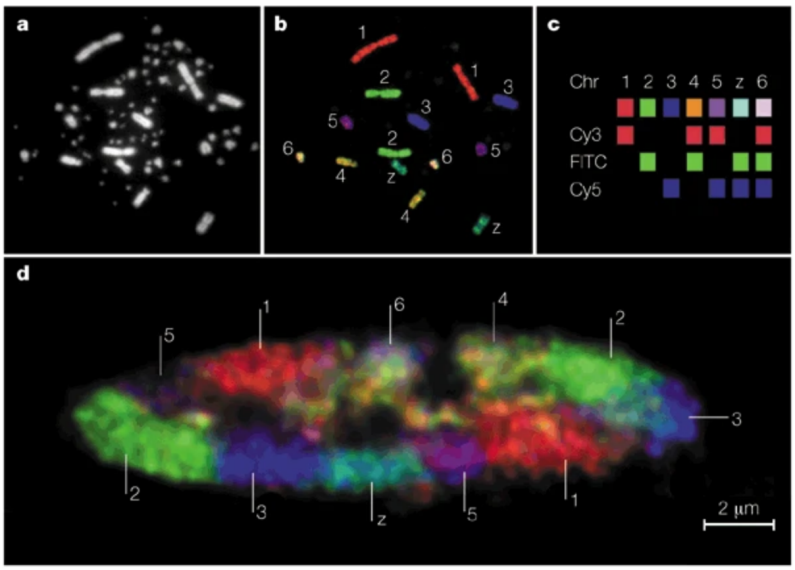

Figure 2.3: Chromosomes during interphase are compartmentalized into discrete domains called *chromosome territories*, firstly observed using "fluorescence *in-situ* hybridization" (FISH) [43]. Their averaged positions within the nucleus is non-random: gene poor/rich chromosomes have been observed systematically closer to the nuclear envelope/center [51]. Reproduced from reference [43]

three dimensional structures manifests themselves at various scales, from the multi-megabase (Mb) scale to the kilobase scale, suggesting the presence of underlying functional organization along the nucleus (see figure 2.2, panel B).

On the nuclear scale, chromosomes do not mix during interphase, but instead they are compartmentalized into discrete domains. These regions, firstly observed using "fluorescence *in-situ* hybridization" (FISH), are called *chromosome territories* (see figure 2.3) [43]. The spatial arrangement of territories is probabilistic, describing the tendency of the chromosome to occupy a definite average position inside the nucleus of a cell population: however, the location of a single chromosome can vary greatly from cell to cell. Also the two copies of the same chromosome can have different positions and even different neighbours [37, 52].

In general, neighboring chromosome territories can overlap to establish enhanced functional interactions between mixing loci located on different chromosomes [38]. The presence of these same functional interactions are observed also in the daughter cells despite the physical separation of chromosomes during cell division: this feature suggests the presence of some molecular mechanism that establishes and maintains the chromosomes' positions [37].

Moreover, the spatial distance of each territory from the nuclear envelope is non-random, with gene poor/rich chromosomes being systematically closer to the nuclear envelope/center [51], suggesting a correlation between the location of loci in the nucleus and the gene expression. However, inside chromosome territories, chromatin is not uniform: transcriptionally inactive segments tend to condensate and to localize at the nuclear periphery, around nucleoli or at subnuclear structures

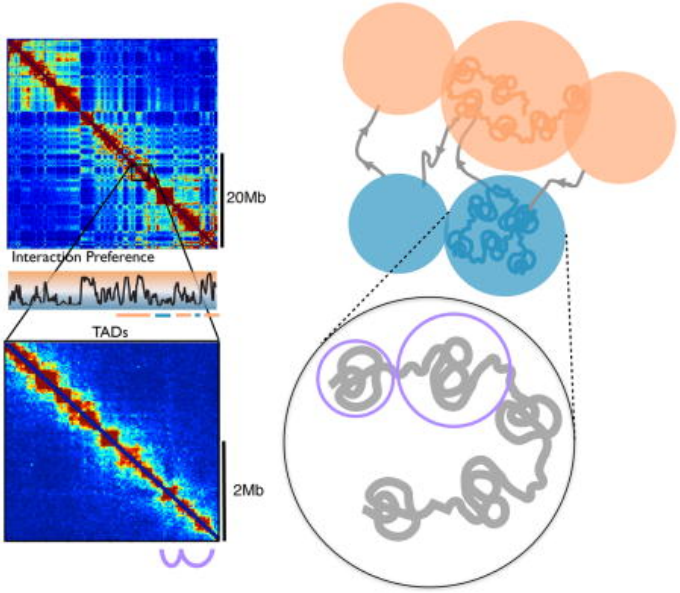

Figure 2.4: HiC maps show an extensive network of chromatin-chromatin contacts within the genome. These interactions can be represented in the form of matrices showing a characteristic patterning into tissue-specific macro-domains ($\gtrsim$ 1 megabasepairs (Mbp)) of active/inactive (A/B) chromatin [13], and tissue-independent micro-domains ($\lesssim$ 1 Mbp) termed TADs [53]. DNA interact more frequently intra-TAD than inter-TAD. Reproduced from reference [38].

such as Polycomb bodies (e.g. Drosophila melanogaster) [38].

The introduction first of Chromosome Conformation Capture (3C) in 2002 [54], and then the development of its high-throughput version Hi-C [13], which allows to detect all pair-wise interactions through genomes, gives the possibility to explore deeply the intricate relationship between genome structure and function within the nucleus, providing more and more accurate data for chromosome interactions. Indeed, chromatin-chromatin contacts detected by Hi-C have shown an additional level of genome organization within chromosome territories [13]: a preferential interaction between chromosome sequences alternating along the chromosomes, with a typical size of a few megabasepairs (Mbp), called *A/B compartments*, has been observed (see figure 2.4). These compartments can be identified in each chromosome by using principal component analysis on the interaction map [13]. The Hi-C data indicate that regions tend be closer in space if they belong to the same compartment than if they do not. Assigning the A or B label to a compartment is not simply an arbitrary or exchangeable state but is correlates with indicators of transcriptional activity, such as DNA accessibility, gene density, replication timing, GC content and several histone marks [38]. Indeed, A/B compartments correlate with (tissue-dependent) active/inactive chromatin: sequences in A compartments are gene rich, more accessible and with higher expression than B sequences [55].

In addition, at the scale of $\lesssim$ 1 Mbp, chromosomes result partitioned into *topologically-associating domains* (TADs, see figure 2.4), built-up from chromatin

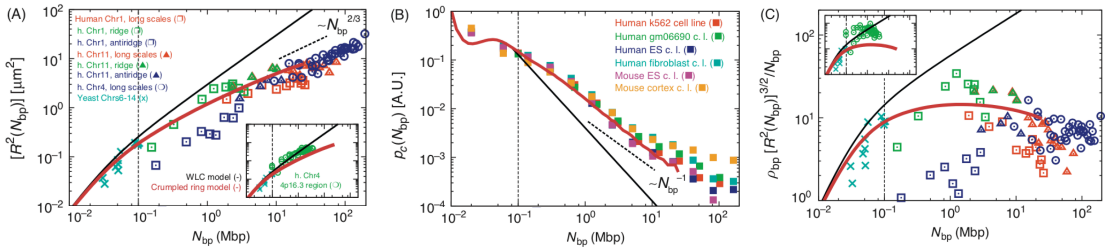

Figure 2.5: Experimental data for interphase chromosomes (symbols) compared to polymer models (solid lines). (A) Mean-square internal distances, $\langle R^2(N_{bp})\rangle$, between two loci at a genomic distance N_{bp} Mbp along the chromatin fiber. Experimental data: interphase yeast [59] and human chromosomes [60, 61] are obtained using FISH (symbols). Data have been compared with WLC model (black line) and the crumpled ring model (red line) [18]. (B) Average probability of contact $P_c(N_{bp})$ between two loci at a distance N_{bp}. Experimental data for human and mouse chromosomes in different cell lines have been measured using HiC [53, 13] (symbols). Data are compared with the WLC model and the crumpled ring model (solid lines). (C) Overlap parameters corresponding to the data shown in (A). Reproduced from reference [62]

itself and characterized by highly enriched intra-domain interactions [13, 53]. TADs constitute regulatory regions where loci and their associated regulatory elements interact frequently with each other and are isolated from the rest of the genome. Remarkably, TADs appear well conserved across tissues *within* the same species [56] and even *between* different species [57]. Moreover, the correct establishment of TAD structure prevents the formation of inappropriate gene-enhancer contacts and its disruption can induce carcinogenesis [58].

To conclude, the phenomenology described can be so summarized: nuclear chromatin fibers form an intricate polymer-like network at small chromatin scales, with "vague" echoes of ordered structures starting from intermediate to large spatial scales (TADs → A/B-compartments → territories).

2.2 Chromatin Fiber Entanglement

In the previous Chapter 1, we have introduced general features of Polymer Physics while along this Chapter we have seen experimental evidences for the polymer-like nature of chromatin within the nucleus of eukariotic cells. It arises naturally to wonder which kind of polymer model can describe how meters of DNA can be packed inside the $5-\mu m$ diameter nucleus of a cell and which kind of DNA structures emerge [63, 62].

Chromatin can be described, within an approximated picture, as a homopolymer formed by DNA wrapped into nucleosomes, where monomers are all identical, with the same size, excluded volume and other interactions, chains have constant density and flexibility along the chain. Other kinds of models include heterogeneity (in

density, interactions, dimensions) using heteropolymer [64, 65, 66].

We have seen that polymer model characterizes chains by their contour length, L_c and their Kuhn length, l_K, as a measure of the chain stiffness. Using experimental data, we can evaluate that for $30 - nm$ chromatin fibers, the contour length $L_c = 0.01\ N_{bp}$ nm and Kuhn length $l_K = 300$ nm (Bystricky et al., 2004), where N_{bp} is the number of basepairs. The same evaluation is possible for $10 - nm$ chromatin fibers, $L_c = 0.125\ N_{bp}$ nm and $l_K \approx 25$ nm (Bystricky et al., 2004).

In this context it is interesting to consider some general features:

- the mean-square spatial distance $\langle R^2(N_{bp})\rangle$ between two loci at a genomic distance N_{bp} Mbp along the chain (measured using fluorescent in situ hybridization, FISH), plotted in figure 2.5, panel A;
- the probability of contact $P_c(N_{bp})$ between two loci at a distance N_{bp} (calculated from the chromatin capture data), plotted in figure 2.5, panel B;
- the overlap parameter, $\Omega(N_{bp}) \equiv \frac{\rho_{bp}}{N_{bp}}\langle R^2(N_{bp})\rangle^{\frac{3}{2}}$, to evaluate N_e for entangled chains when reaches a characteristic threshold, $\Omega = 20$ [21, 18, 67], plotted in figure 2.5, panel C.

The models for $10 - nm$ and $30 - nm$ chromatin fibers is in agreement with the random walk regime as the mean-square internal distances $\langle R^2(N_{bp}\rangle \approx 3N_{bp}nm^2$ [68]. Moreover, the WLC model (black lines in figure 2.5) can be used to describe sequence-, cell-type, and species-averaged experimental data for genomic distances up to ≈ 100 kbp and even the equilibrated telomeric regions up to the Mbp scale [69]. The effects of topological constraints can be seen beyond the entanglement length, N_e (which can be evaluated from the overlap function $\Omega(N_{bp})$, panel C). In particular, considering a typical nuclear densities of $\rho_{bp} = 0.011bp/nm^3$, the entanglement length for genomic DNA is of the order of $N_e = 1.2 \times 10^5 bp$ for both chromatin fiber models [69]. In details, the effect of entanglements emerges clearly from the experimental data. Indeed, comparing panels A and B in figure 2.5, the deviations from the WLC behavior correspond to the cases in panel C where the overlap parameter exceeds the entanglement threshold of 20.

2.2.1 "Topological" Origin of Chromosome Territories

In spite of their intrinsic complexity, the general behavior of interphase chromosomes is remarkably well described by generic polymer physics [62, 39, 55, 61, 63, 70, 71, 72, 73].

Under these conditions and supported by experimental observations on the polymer-like nature of the chromatin fiber (section 2.1.1, the theory of semi-dilute polymer solutions [2] represents a good starting point for a quantitative description of chromosome organization inside the nucleus.

At the beginning of interphase, each chromosome evolves from its initial, compact mitotic conformation and starts swelling inside the nucleus (figure 2.6, panel A). Rosa and Everaers [69] argued that the time to reach the *complete* mixing of all

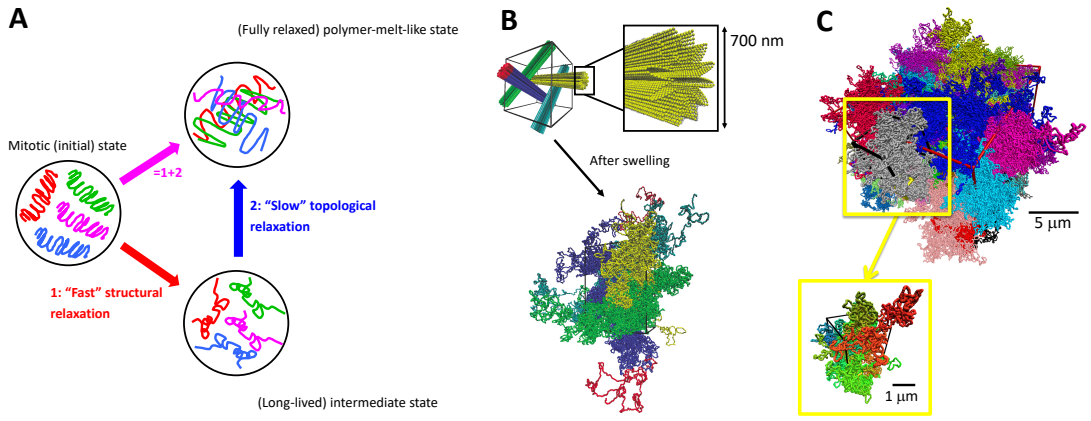

Figure 2.6: "Topological" model for chromosome territories. (A) At the beginning of interphase, condensed mitotic chromosomes start swelling. The path to full relaxation and complete mixing cannot take place on natural time scales due to "slow" relaxation of the topological degrees of freedom [69]. Chromosome structures thus remain effectively quenched into separated territories which retain "memory" of the initial conformations. (B) Numerical implementation of the model by Molecular Dynamics (MD) computer simulations [69]. Model chromosomes are initially prepared into non-overlapping mitotic-like structures. MD simulations show the rapid relaxation of polymer length scales up to the tube diameter d_T, while larger length scales fold into a crumpled structure resembling the behavior of ring polymers. Each color corresponds to a single model chromosome. Reproduced from reference [69]. (C) The analogy between solutions of ring polymers and chromosome territories can be systematically exploited owing to an efficient coarse-grain protocol [18] which allows to obtain hundreds of independent model conformations of mammalian-sized chromosomes. The model can be mapped to *real* time and length scales (see bars) with no free parameter [69, 18]. The snapshot here provides a typical view for a model human nucleus. Reproduced from reference [18].

Physical parameters of the "bead-spring" polymer model by Rosa and Everaers [69, 18].	
ρ_{DNA}	$0.012\mathrm{bp/nm}^3$
$\rho_{30\mathrm{nm}}$	$1.2 \cdot 10^{-4}/\mathrm{nm}^2$
ℓ_K (30nm fiber)	$300\mathrm{nm} = 30\mathrm{kbp}$
ξ	90nm
$\frac{L_e}{\ell_K} = \left(\frac{20}{\rho_{30\mathrm{nm}}\,\ell_K^2}\right)^2$	$4\ell_K = 1200\mathrm{nm} = 0.12\mathrm{Mbp}$
$d_T = \sqrt{\frac{\ell_K L_e}{6}}$	245nm
τ_e	32s

Table 2.1: ρ_{DNA}, DNA density calculated for an "average" human nucleus of 5μm radius; $\rho_{30\mathrm{nm}}$, 30nm chromatin fiber density assuming fiber compaction of 100bp/nm (section 2.1.1); ℓ_K, Kuhn length of the 30nm fiber [59]; ξ, average distance from a monomer on one chain to the nearest monomer on another chain ("correlation length" [2]); L_e, entanglement length obtained from the condition of "optimal packing" of 20 chains per entanglement volume by Kavassalis and Noolandi [21]; d_T, average spatial distance between entanglements ("tube diameter" [2]); τ_e, time scale marking the onset of entanglement effects.

chromosomes starting from the fully *unmixed* state can be estimated by assuming ordinary reptation dynamics [1, 2] for linear polymers in concentrated solutions: $\tau_{mix} \approx \tau_e \left(\frac{L_c}{L_e}\right)^3$ where $\tau_e \approx 32$ seconds and $L_e \approx 0.12$ megabasepairs (Mbp) are, respectively, the entanglement time and entanglement length of the chromatin fibers solution (Table 2.1). With typical mammalian chromosomes of total contour length L_c of the order of 10^2 Mbp, τ_{mix} is exceeding by orders of magnitude the typical cell life time. As a consequence, the spatial structures of chromosomes remain effectively stuck into territorial-like conformations retaining the topological "memory" of the initial mitotic state.

These considerations were adapted into a generic bead-spring polymer model [69] taking into account the density, stiffness and local topology conservation of the chromatin fiber (Table 2.1). Extensive Molecular Dynamics computer simulations then showed that the swelling of model mitotic-like chromosomes (figure 2.6, panel B) leads to compact territories with physical properties akin to crumpled conformations of ring polymers in entangled solutions. The analogy between chromosome territories and ring polymers motivated the formulation of the efficient multi-scale algorithm described in [18] which is capable of generating hundreds of putative chromosome conformations (see figure 2.6, panel C for a single example) in negligible computer time. The polymer model was shown to reproduce the experimentally observed behavior of (sequence-averaged [62]) properties of interphase chromosomes: these include chromosomes spatial positions measured by FISH, chromatin-chromatin interaction data and time mean-square displacements of chromosome loci [69, 74, 68, 62].

For illustration purposes, the single chromosome structure is described through

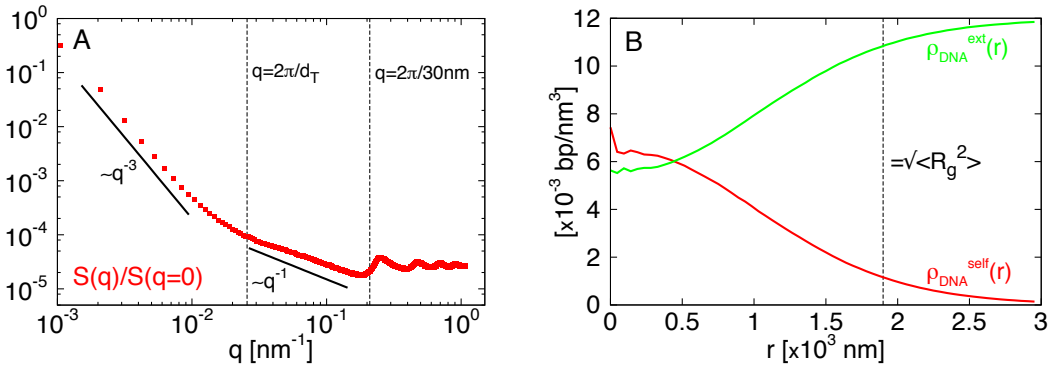

Figure 2.7: Predicted spatial structure of model mammalian chromosomes [69, 18]. (A) Structure factor $S(\vec{q})$ *vs.* the norm of the wave vector $q \equiv |\vec{q}|$. The two regimes q^{-1} (rod-like) and q^{-3} (compact-like) are for spatial scales, respectively, below and above the tube diameter, $d_T \approx 245$nm, of the chromatin fiber. The wavy behavior at large q is an artifact due to the discrete bead-spring nature of the model. (B) Average DNA density at spatial distance r from the chromosome center of mass: $\rho^{\rm self}_{\rm DNA}(r)$, self-density contribution from the given chromosome; $\rho^{\rm ext}_{\rm DNA}(r)$, external contribution from the surrounding chromosomes. The sum of the two equals the average DNA density $= 0.012$bp/nm^3 (Table 2.1). For reference, the dashed line corresponds to the predicted average size of a single chromosome territory.

the structure factor [2] $S(q) \equiv \langle e^{i\vec{q}\cdot(\vec{r}_i - \vec{r}_j)} \rangle$ as a function of the norm of the wave vector $q \equiv |\vec{q}|$ (figure 2.7(A)). $\vec{r}_i$ are the spatial positions of chromosome loci and average is taken over all chromosome conformations. For wave vectors $q \lesssim \frac{2\pi}{d_T}$ where $d_T \approx 245$nm is the tube diameter of the chromatin fiber [69, 74] $S(q) \sim q^{-3}$, which corresponds to the expected result for a compact, scale-free polymer.

While $S(q)$ provides information on single-chain properties, it is instructive to look at the spatial relationship between different territories. To this purpose, we consider the average DNA density at spatial distance r from the chromosome centre of mass and its two components (figure 2.7, panel B): the self-density contribution from the given chromosome ($\rho^{\rm self}_{\rm DNA}(r)$) and the external contribution from the surrounding chromosomes ($\rho^{\rm ext}_{\rm DNA}(r)$). The plots demonstrate that chromosomes are rather "soft": as for common polymer systems [75], the core of each chromosome contains a significant amount of DNA protruding from close-by chains. In summary territoriality is not a preclusion for chromosome strands to intermingle with each other, in agreement with cryo-FISH experiments [76].

2.3 Epigenetics

As described in the previous section, the three-dimensional genome structure has been recognized to regulate gene expression and ordered structures emerge at various scales suggesting a functional arrangement of the nuclear space. The nonrandom or-

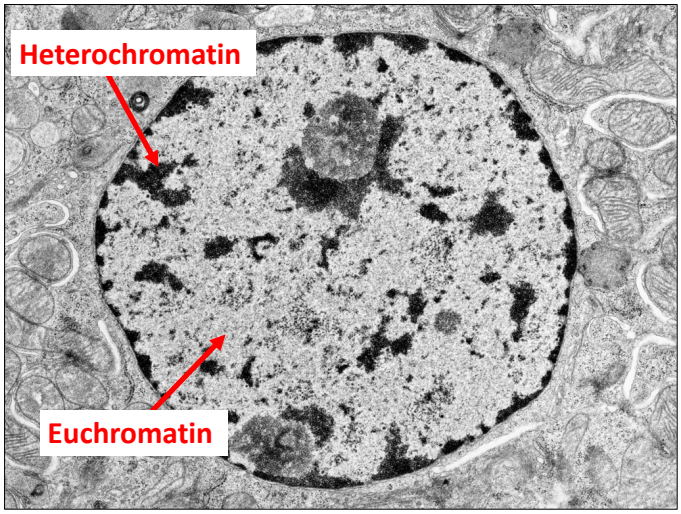

Figure 2.8: Chromatin is organized into epigenomic domains which contains only a specific chromatin type and isolated from other domains. The most frequent are called euchromatin, composed by active genes and which appears less condensed, and heterochromatin, which contains inactive genes, late replicating and inhibitory to transcriptional machinery and typically appears highly condensed. Reproduced from the Yale Histology Gallery (link).

ganization appears also with local compartmentalization: active and inactive genome regions are separated from each other, enhancing the efficiency of gene expression or repression. Such compartmentalization might also give a concrete contribution to bring co-regulated genes into physical proximity to coordinate their activities. Indeed, the ability of organisms to precisely regulate gene expression is central to their development, requiring the activation of transcription during the appropriate developmental stage. In facts, all cells have the same genome but in each cell only a subset of genes is expressed: depending on the specific environment, cells can differentiate into a variety of cell types. The cell type is inherited by the daughter cells. How heritable phenotype is functionally relevant without any alteration of the genomic sequence is the core of *epigenetics* [77, 78].

The local organization and the gene activity of the genome is strictly related to its genotype. Indeed, the chromatin state depends on local conditions, like the nucleosome density and positioning, the covalent modifications of DNA and histones tails and the insertion of histone variants. Moreover, statistical analysis of epigenomic patters across the genome of eukaryotic cell have shown that chromatin is organized in *epigenomic domains* (domains with a typical size which can vary fror kilobases to few megabases,) containing only a specific chromatin type and isolated from other domains. In particular, several kinds of domains have been observed, the most frequent are *euchromatin*, which contains high density of early replicating and active genes and appears less condensed, and *heterochromatin*, which contains inactive genes, late replicating and inhibitory to transcriptional machinery and typically appears highly condensed (see figure 2.8).

In many higher eukaryotes, also other chromatin types has been identified, the constitutive HP1-like heterochromatin, the facultative (developmentally regulated) Polycomb-like heterochromatin and ultra-repressive heterochromatin enriched in genes that are expressed in very few tissues, the so-called void or black chromatin [79, 78].

There are several mechanisms which can be involved in the transmission of epigenetic information like DNA methylation, histones post-translational modifications (PTMs), chromosome coating with noncoding RNAs as in X inactivation, messenger RNA silencing by interaction with micro RNAs, or the coupling between epigenetics and supercoiling [77]

Historically speaking, the first stable epigenetic mark which has been recognized is the DNA methylation. DNA methylation is the substitution of a methyl ($-CH_3$) group to the carbon atom in position 5 at the cytosine base. The patterns of DNA methylation in the genome are established in early stages of development and then inherited through mitosis without modification in the sequence [80]. The biological role of DNA methylation is not completely understood and depends on the context in which it may be found [81, 82]. DNA methylation is directly involved in gene silencing [83, 84], in X-chromosome inactivation [85, 86], and gene imprinting [87]. At the same time, it has been also related to active gene bodies [88]. Moreover, also the structure of nucleosomes is affected by methylation [89]: methylation leads to an enhanced rigidity of DNA around the histones and to more compact and closed nucleosomes [90]. Also histone PTMs are fundamental in the transmission of epigenetic information. In the previous section, we have introduced the nucleosomes, composed by a DNA segment wrapped around an histone complex. In particular, histone tails have a crucial role in the structure of nucleosome arrays and are the main target of post-translational modifications on histones. Epigenetic marks are deposited on or removed from histone tails by dedicated enzymes, so-called "writers" and "erasers", devoted to lysine methylation or lysine acetylation of histones tails [91, 77]. These two mechanism can affect the chromatin architecture and state of activity: acetylation directly affects nucleosome-nucleosome interactions and is associated to loss of a positive charges while methylation affects indirectly chromatin recruiting additional architectural proteins [77].

Chapter 3

Epigenetics-Inspired Physics: the Ising Model in Branched Lattice Polymers

The content of this Chapter[1] focuses on the properties of the classical Ising model with nearest-neighbor interaction for spins located at the monomers of long polymer chains in 2 and 3 dimensions. There are two main motivations for carrying such a study:

- As shown in Chapter 1, chromosomes can be modelled by means of generic polymer physics. In particular, the large scale behavior of chromosome conformations is well accounted for by the same Physics which describes the folding of branched crumpled polymers in dense solutions.

- Second, several (polymer) models [64, 65, 66] employ the (local) epigenetic state of chromatin as an internal degree of freedom with local nearest-neighbor interactions.

Moving from these considerations, in this Chapter we introduce and study by classical mean-field techniques and systematic computer simulations a minimal polymer model with classical spins located on monomers' spatial positions and where local ordering is enforced by standard Ising coupling.

To compare the effects of polymer conformations vs. Ising interactions, we will compare results for two ensembles of polymers with very different single chain properties: (1) *swollen*, self-avoiding linear polymer chains in good solvent conditions and (2) *compact*, space-filling randomly branching polymers in melt. Thus, we will show that swollen polymers can not sustain an ordered phase. On the contrary, compact polymers may produce an observable phase transition. Finally, we will briefly consider the statistical properties of the ordered phase by comparing polymer chains within the same universality class but characterized by very different shapes.

[1]The material described in this Chapter has been published in: Papale A., Rosa A., European Physical Journal E. **41**: 144 (2018) [92]

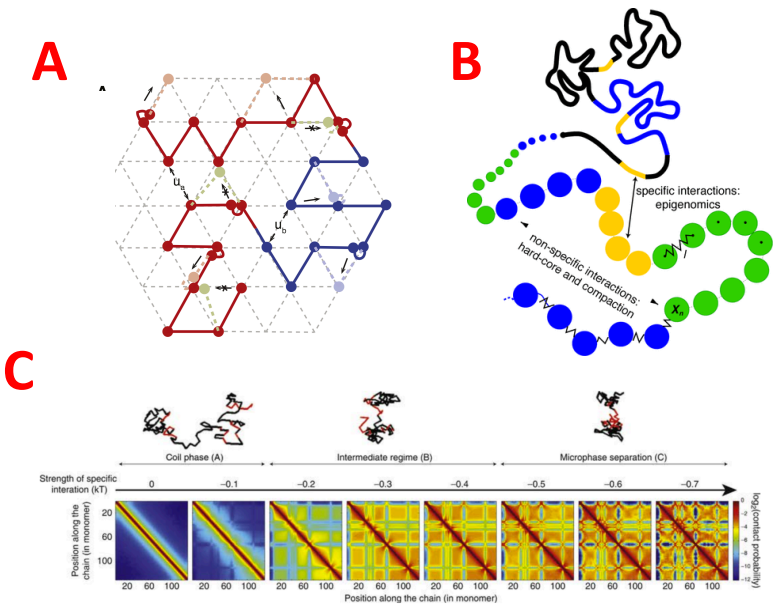

Figure 3.1: (A) Chromatin has been modeled as a block copolymer on a triangular lattice. (B) Each block contains consecutive monomers with an identical chromatin state. (C) The interaction takes into account excluded volume and an attractive short-range interactions between monomers of the same state. Various phases has been observed tuning the strength of state-dependent interaction, from microphase separation (attractive interactions, monomers with the same state occupied separate spatial regions) to a coil phase (no interactions, unstructured phase). Reproduced from reference [65] (panel A), from reference [64] (panel B) and from reference [62] (panel C).

3.1 Epigenetics and Ising Model

Lately, experimental data based on chromosome conformation capture techniques have shown the presence of functional structures of nuclear organization of chromatin depending on the epigenetic state.

As described in section 2.3, the epigenetic state of chromatin regulates not only the local gene activity but also its spatial organization: A/B compartments are correlated with the inhomogeneous local activity of chromatin. Preferential interaction emerge within active regions (A compartment, gene rich and more accessible regions, correlates with high density of euchromatin) and region with inactive or repressive hererochromatin (B compartment) [93].

According to these observations, the correlation between the 1D chromatin epigenetic states and the 3D chromatin spatical organization is the starting point for several model based on heteropolymer where couplings depend explicitly on the local states of chromatin [64, 65, 66, 78, 94]. These kind of model assumes an effective specific short-range interactions between genomic loci mediated by chromatin-binding proteins with sequence- or epigenetic-specific affinities [62].

Just as an example, a recent model developed by Jost and co-workers [65] concerning heteropolymer with epigenetic-dependent interaction has shown the emergence of domains like the TADs inside chromosome territories (see figure 3.1).

Chromatin is modeled as a block copolymer lying on a triangular lattice where each block corresponds to consecutive monomers with an identical chromatin state (see figure 3.1, panel B). The dynamics is defined considering thermal fluctuations, excluded volume and an attractive short-range interactions between monomers of the same state. The block copolymer model has characterized by various phases (see figure 3.1, panel C) tuning the strength of state-dependent interaction. A microphase separation appears with strong attractive interactions, monomers with the same state occupied separate spatial regions, like a checker-board arrangement. On the contrary, with weak interactions there is a phase characterized by unstructured, coils. The intermediate regime is more dynamical: the system exhibits a continuous crossover between the coil and the microphase regimes. Firstly blocks collapse in TAD-like domains and then a weak long-range interactions between TADs of the same state emerges. Clearly the phase diagram is strongly dependent on the initial arrangements of the blocks of chromatin states on the copolymer. Moreover, the numerical results have been also compared with experimental data relative to the Drosophila melanogaster genome [65]. The intermediate regime where chromatin blocks have partially collapsed into TADs and where blocks of the same state transiently merge together are compatible with the experimental HiC data [62].

3.2 The Ising Model

The Ising model, introduced in the early '20's [95, 96] of the XX century as a generic toy model for understanding the para-/ferro-magnetic phase transition in terms of the cooperativity of a lattice arrangement of molecules with nearest-neighbor interactions, has become since then a cornerstone of Statistical Physics [97, 98]. On top of that, owing to its simplicity it has become of fundamental importance for the generic description of cooperative phenomena in other fields, including disorderd systems [99], neuroscience [100] and econophysics [101].

The model is formulated in terms of $V = R^d$ binary spin-like variables $s \equiv (s_1, s_2, ..., s_V)$ with $s_i = \pm 1$, located at the nodes of a d-dimensional hyper-cubic lattice of linear size R with short-range interactions. The Hamiltonian of the Ising model in the presence of an external field h is defined by:

$$\mathcal{H}(h; s) = -\frac{J}{2} \sum_{i,j=1}^{V} s_i \, \Delta_{i,j} \, s_j - h \sum_{i=1}^{V} s_i \,, \tag{3.1}$$

$\Delta_{i,j} = 1$ if sites i and j are nearest neighbors on the lattice and zero otherwise. The fist term represents the interaction energies which favours an ordered ferromagnetic state (if $J > 0$). The second term describes the interaction between the applied external field h and the spin system, for paramagnetic systems.

In the canonical ensemble the partition function can be easily written as

$$\mathcal{Z}_N = \sum_{\{s\}} e^{-\beta \mathcal{H}(h;s)} \tag{3.2}$$

where the sum is over all the possible configurations of spin variables. Then, the magnetic free energy per site in the thermodynamic limit is:

$$F(\beta, h) = \lim_{N\to\infty} \left(\frac{1}{N} \, ln \, \mathcal{Z}_N \right) \tag{3.3}$$

.

In dimension $d = 1$, it is possible to obtain an analytical expression for the free energy, for example using the technique of the transfer matrices [102]. This case is peculiar: the energy turns out to be an analytic function of temperature T and external field h (except at the trivial point $t = h = 0$) and there is no phase transition or spontaneous magnetization (see Yang-Lee theorem, reference [103]).

The transfer matrices technique can be written also in higher dimensions but an analytical solution was obtained by Lars Onsager [104] for the 2-dimensional case on a square lattice, with nearest neighbor interactions and in the absence of an external field. He demonstrated the existence of a phase transition at a critical temperature $\kappa_B T_c/J = 2/ln\left(1+\sqrt{2}\right)$. For dimension $d > 2$, the ferromagnetic phase has been characterized by a large number of approximated (mean-field) and exact (renormalization group) techniques as well as numerical methods (Monte Carlo).

3.3 The Ising Model in Swollen and Compact Polymers

While the Ising model on the regular hyper-cubic lattice is well characterized [98], it is an interesting and non-trivial question to ask if and how its properties change in lattices with more complex geometries and architectures. In the past, there has been a lot of work in this direction for the case where the spin variables are located on the monomers of a single isolated polymer chain with excluded volume interactions [105, 106, 107, 108, 109]. Spin-spin interactions add up whenever pairs of corresponding chain monomers are close in space either because they are close along the polymer sequence or, more generally, as a consequence of chain folding in the embedding space. As the average number of neighbors per polymer site is larger than two, these systems are considered as in between the one-dimensional linear chain (for which no ordered phase at zero external field exists [98]) and the expected [98] critical Ising behavior in $d > 1$ dimensions.

Here, we take one step further in this direction and we consider the case where the binary Ising variables reside on the nodes of randomly branching polymers (modelled as lattice trees [23]) in two- and three-dimensional melts.

There are several reasons behind our motivations to extend the Ising model to this particular class of polymers: (i) Randomly branching polymers were introduced back in the '80-'90's [14, 30, 110] for describing the large-scale folding and

dynamics of a single ring polymer in an array of uncrossable point obstacles. More recently [17, 18, 23], they have aroused new interest because they provide a good quantitative model to understand the fractal-like, space-filling folding of mutually interacting unknotted and untangled ring polymers in melts and the "territorial" behavior of DNA and chromosomes inside the nuclei of eukaryotic cells [18, 69, 111]. (ii) To remain on the ground of the spatial behavior of chromosomal DNA, Ising-like models have been recently employed to characterize one-dimensional long-range correlations of nucleotides in the human DNA sequence [112], as well as to describe the appearance of local ordered phases (micro-phases) inside the nuclei of the cells [64, 65, 78] (see section 3.1). To date though, there is no comprehensive study addressing the properties of the Ising model on branched, complex polymer architectures, as the ones which are expected to emerge in the context of DNA and chromosomes biology.

In the following section, we will show a systematic analysis on the physics of the Ising model in melts of randomly branching polymers, and we compare the results to corresponding ones obtained for the "classical" [105, 106, 107, 108, 113] case of ordinary self-avoiding linear polymers.

We study the statistical properties of the Ising model separately for each of the ensembles considered (self-avoiding linear *vs.* melts of randomly branched polymers). In other words, Ising nearest-neighbor interactions are completely defined according to the statistics of the given polymer ensemble: this is then different from the model presented in reference [109] where polymer folding is "driven" by the Ising coupling.

The work is organized in two main directions: first we consider an analytical yet approximate mean-field-like approach, and then we compare and generalize the obtained results by employing Monte Carlo computer simulations for the Ising model in lattice polymer chains in 2 and 3 spatial dimensions.

3.3.1 Mean-Field Approach

Our mean-field approach is mainly based on the work by Garel *et al.* [109]. However, at odds with this publication, here we restrict the statistics of polymer conformations under the assumption that they belong to a given, well-defined ensemble. Of course, the opposite case where polymer configurations change according to the Ising nearest-neighbor interactions is equally interesting and worth of future investigations.

A mean-field approach to the Ising model in polymer chains made of N monomers and confined in a volume V starts from the partition function $\mathcal{Z}_N$ defined by [109]:

$$\mathcal{Z}_N = \sum_{\mathrm{w}\in\mathrm{walks}} \sum_{\{s_i=\pm 1\}}^{\mathrm{w}} \exp\left(\frac{\beta J}{2}\sum_{i,j=1}^{V}\sigma_i^{\mathrm{w}}\,\Delta_{i,j}\,\sigma_j^{\mathrm{w}} + \beta\sum_{i=1}^{V}h_i\,\sigma_i^{\mathrm{w}}\right), \qquad (3.4)$$

where: (a) the first sum goes through all possible polymer conformations or walks, and (b) the second sum goes over all possible spin configurations for the given polymer (walk) conformation. $\beta = 1/\kappa_B T$ is the usual Boltzmann factor and T is

the temperature. For time being and for the sake of generality, the magnetic field is assumed to be also a function of the spatial position on the lattice.

By expressing the variables $\sigma_i^{\rm w}$ $(i = 1, ..., V)$ in terms of the product $\sigma_i^{\rm w} = s_i\,\theta_i^{\rm w}$ where s_i takes binary values ± 1 and $\theta_i^{\rm w} = 1$ if lattice site i is occupied by a monomer and $= 0$ otherwise and performing standard Hubbard-Stratonovich [114] transformation, $\mathcal{Z}_N$ can be written in terms of generic field variables ϕ_i as:

$$\begin{aligned}
\mathcal{Z}_N &= \sqrt{\frac{(1/2\pi\beta J)^V}{\det\Delta}} \int \prod_{i=1}^{V} d\phi_i\, e^{-\frac{1}{2\beta J}\sum_{i,j}\phi_i(\Delta^{-1})_{i,j}\phi_j} \times \sum_{\rm w\in walks} \sum_{\{s_i=\pm 1\}}^{\rm w} \prod_{i=1}^{V} e^{(\beta h_i+\phi_i)\,\sigma_i^{\rm w}} \\
&= \sqrt{\frac{(2/\pi\beta J)^V}{\det\Delta}} \int \prod_{i=1}^{V} d\phi_i\, e^{-\frac{1}{2\beta J}\sum_{i,j}\phi_i\,(\Delta^{-1})_{i,j}\,\phi_j} \times \sum_{\rm w\in walks} \prod_{i=1}^{V} \cosh\left((\beta h_i+\phi_i)\,\theta_i^{\rm w}\right) \\
&\equiv \sqrt{\frac{(2/\pi\beta J)^V}{\det\Delta}} \int \prod_{i=1}^{V} d\phi_i\, \exp(-\beta\mathcal{L}(\{\phi,h\}))\,,
\end{aligned} \tag{3.5}$$

where

$$\mathcal{L} = \frac{1}{2\beta^2 J}\sum_{i,j}\phi_i\,(\Delta^{-1})_{i,j}\,\phi_j - \frac{1}{\beta}\log\sum_{\rm w\in walks}\prod_{i=1}^{V}\cosh\left((\beta h_i+\phi_i)\,\theta_i^{\rm w}\right)\,.$$

Then [114], the mean-field theory can be derived by looking for the saddle point approximation of the integral in Eq. 3.5. This is obtained by imposing $\left.\frac{\partial\mathcal{L}}{\partial\phi_k}\right|_{\phi_k=\bar{\phi}_k} = 0$, $\forall k$:

$$\begin{aligned}
0 = &\frac{1}{\beta^2 J}\sum_i(\Delta^{-1})_{k,i}\,\bar{\phi}_i \\
&-\frac{1}{\beta}\frac{\sum_{\rm w\in walks}\theta_k^{\rm w}\sin\left((\beta h_k+\bar{\phi}_k)\,\theta_k^{\rm w}\right)\prod_{i=1}^{V}{}^{i\neq k}\cosh\left((\beta h_i+\bar{\phi}_i)\,\theta_i^{\rm w}\right)}{\sum_{\rm w\in walks}\prod_{i=1}^{V}\cosh\left((\beta h_i+\bar{\phi}_i)\,\theta_i^{\rm w}\right)}.
\end{aligned} \tag{3.6}$$

Consequently, the corresponding magnetization at lattice site k, M_k, is given by:

$$\begin{aligned}
M_k &\equiv -\frac{\partial\mathcal{L}(\{\bar{\phi},h\})}{\partial h_k} \\
&= \frac{\sum_{\rm w\in walks}\theta_k^{\rm w}\sin\left((\beta h_k+\bar{\phi}_k)\,\theta_k^{\rm w}\right)\prod_{i=1}^{V}{}^{i\neq k}\cosh\left((\beta h_i+\bar{\phi}_i)\,\theta_i^{\rm w}\right)}{\sum_{\rm w\in walks}\prod_{i=1}^{V}\cosh\left((\beta h_i+\bar{\phi}_i)\,\theta_i^{\rm w}\right)} \\
&= \frac{1}{\beta J}\sum_i(\Delta^{-1})_{k,i}\,\bar{\phi}_i\,.
\end{aligned} \tag{3.7}$$

With $h_k = h$ constant on the lattice and assuming *translational invariance*, $\theta_k^{\rm w}$ is equal to the average polymer occupancy $\rho \equiv \frac{N}{V}$ and we can substitute the site-dependent quantities with their corresponding averages: $\bar{\phi}_k = \langle\phi\rangle$, $M_k = \langle M\rangle$. Thus, the polymer-dependent term in both Eqs. 3.6 and 3.7 simplifies, and we get the following simple equations:

$$\langle\phi\rangle = \beta J q \rho \tanh\left(\rho(\beta h + \langle\phi\rangle)\right) \tag{3.8}$$

$$\langle M\rangle = \frac{1}{\beta J q}\langle\phi\rangle \tag{3.9}$$

where q is the coordination number of lattice ($q = 2d$ for a cubic lattice in d-dimensions). Eqs. 3.8 and 3.9 can be combined into a single self-consistent expression for the average magnetization *per monomer*, $m = M/\rho$:

$$\langle m\rangle = \tanh\left(\beta\rho\left(h + Jq\rho\,\langle m\rangle\right)\right)\ . \tag{3.10}$$

Since polymer size R increases as a power law [2] of the number of monomers N, $R \sim N^{\nu}$, the average polymer occupancy in d dimensions $\rho = N/V$ goes as $\sim N^{-(d\nu-1)}$. Thus, according to Eq. 3.10, for any $\nu > 1/d$ and zero external field h we should expect no spontaneous magnetization (*i.e.*, $\langle m\rangle \neq 0$ at some finite $T = T_c > 0$) in the thermodynamic limit. In particular, this is true for linear polymer chains in good solvent conditions where [2] $\nu \approx 3/(d+2) > 1/d$ for $1 < d \leq 4$. In spite of the simplicity of the mean-field method, this result agrees with more rigorous (and more complicate) renormalization-group arguments [107, 108] indicating a vanishing $T_c \to 0$ for this particular class of polymers. Conversely space-filling compact polymers, having $\nu = 1/d$, are expected to sustain a finite magnetization at some $T = T_c$.

Eq. 3.10 deserves a few comments. First the formula is different from the original result Eq. 13 presented in reference [109]. In fact, in the latter publication the argument in the "tanh"-term does not contain the ρ factor. On the other hand, this has interesting consequence: In fact, the behavior of the "critical" temperature in the $N \to \infty$ thermodynamical limit is $T = T(N) \equiv Jq\rho^2$, *i.e.* it depends quadratically on ρ. This expression is particularly attractive as it displays the same functional behavior of the "classical" two-body interaction term per unit volume of the Flory theory [2, 8], which is known to describe excluded volume effects in polymers.

In the next section, we challenge the mean-field approach by employing Monte Carlo computer simulations of the Ising model in $2d$ and $3d$ swollen *vs.* space-filling (or compact) polymers. For the former case, we consider self-avoiding walks describing linear polymers with excluded volume interactions [2]: they represent the "classical" polymers which were extensively examined in the past [105, 106, 107, 108, 109]. For the latter, we employ melts of randomly branching polymers, an entirely *novel* [17, 23, 115] class of polymers who have been shown relevant to model the large-scale behavior of ring polymers in topologically constrained environments [18, 17, 116] and chromosome territories in eukaryotes [69, 111]. Notably, these polymers segregate owing to purely topological interactions between polymer strands and not because of a change in the quality of the solvent as in the classical coil-globule

transition [2]. The present work then extends the Ising model to an "unusual" polymer ensemble.

3.3.2 MonteCarlo Computer Simulations

In this section we focus on the statistical properties of the Ising model separately for each of the ensembles considered, self-avoiding linear walks (SAW) and melts of randomly branched polymers (RPS), with the help of a numerical approach based on Monte Carlo simulation.

As described in appendix A.1.1, the average linear size or gyration radius of self-avoiding linear walks (SAW's) with excluded volume interactions (good solvent conditions [2]) in d dimensions increases with the number of monomers N as $R_g \sim N^{\nu}$ with $\nu = 3/(d+2)$ and, hence, single polymer conformations are not space-filling. Spatial conformations of single SAW's in 2 and 3 dimensions were generated according to the dynamical Metropolis Monte Carlo algorithm known as the *pivot* algorithm, see for details reference [117]. By applying repeatedly the described algorithm, we have generated ensembles of 10^4 statistically independent self-avoiding polymer chains made of $16 \leq N \leq 4096$ bonds.

At the same time, the average gyration radius of randomly branching polymers (RBP's) in melt conditions increases with the number of monomers N as $R_g \sim N^{\nu}$ with $\nu = 1/d$ [17, 18, 23], thus they constitute typical examples of compact, space-filling polymers (see appendix A.1.2)

Spatial conformations of RBP's made of $N+1$ monomers in $2d$ and $3d$ melts composed of M chains were generated according to the lattice tree model as described in references [23, 118, 115]. Here, we consider $2d$ and $3d$ trees in melt with Kuhn density $\rho_K l_K^d = 2$. We have considered polymer chains made of $10 \leq N \leq 900$ bonds, with a total number of chains in the range $32 \leq M \leq 384$ and 100 independent melt configurations. For each single polymer chain of the different simulated ensembles, we have generated equilibrated configurations of Ising spin variables at temperature T and null external applied field h by employing the Wolff algorithm [119, 120] (for further details see appendix A.2) which is known to be especially efficient at low temperatures. The nearest-neighbor interactions of the Ising model, Eq. 3.4, are computed between monomer sites whose spatial distance is $\leq$ the lattice spacing. As we are interested to the connection between single-chain structure and the magnetic properties of the polymer, spin-spin interactions in branched polymers in melt are calculated only between spins on monomers of the same chain. Finally, the total number of spin configurations per single polymer chain is 10^4 for computations of averages on the corresponding full polymer ensemble (section 3.3.4) and 10^6 for averages taken on selected single polymer conformations (section 3.3.5).

3.3.3 Results and Discussion

In this section, we discuss our results for the Ising model in randomly branching polymers in $2d$ and $3d$ melts and illustrate how the magnetic properties of these polymers differ from self-avoiding walks.

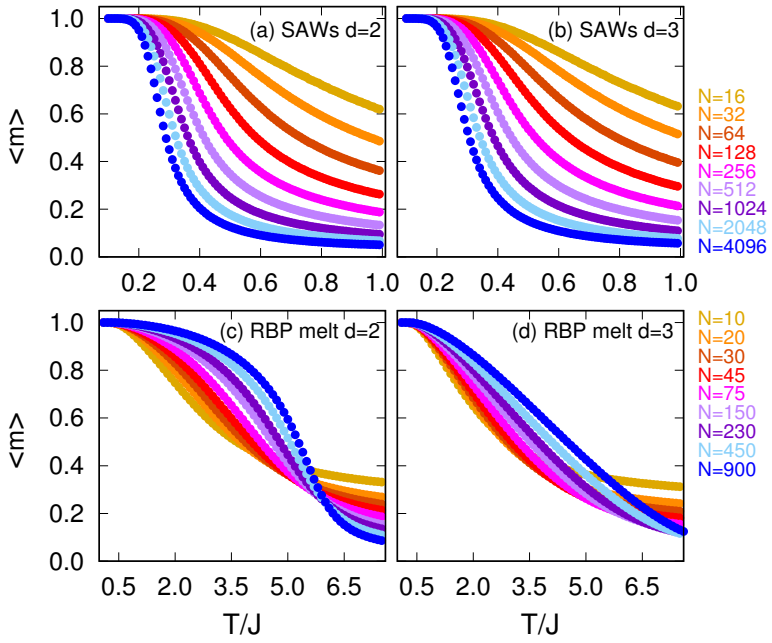

Figure 3.2: Average magnetization per monomer, $\langle m \rangle = \langle m(T) \rangle$, as a function of temperature T, see definition Eq. 3.11, for self-avoiding walks (SAW's, top panels) and melt of randomly branching polymers (RBP melt, bottom panels). Temperature values have been chosen by sampling uniformly along the shown intervals.

We divide the analysis in two parts: We first consider ensemble-average properties (section 3.3.4), where we discuss the temperature behavior of typical observables [98] like the average magnetization ($\langle m \rangle = \langle m(T) \rangle$) and the average susceptibility ($\langle \chi \rangle = \langle \chi(T) \rangle$). Each observable is averaged first on distinct Ising configurations at fixed polymer conformation, and then we combine together the results from different conformations, see definitions Eqs. 3.11 and 3.12 below. In section 3.3.5, we discuss statistical fluctuations of these observables between single chain conformations within the same universality class but characterized by very different shapes. For the sake of the notation, in this second section we employ the symbols $m^{\mathrm{w}}(T)$ and $\chi^{\mathrm{w}}(T)$ for, respectively, the magnetization and susceptibility calculated on specific polymer walks.

3.3.4 Ensemble-Average Properties

For $h = 0$, the system is invariant under symmetry $\sigma_i^{\mathrm{w}} \to -\sigma_i^{\mathrm{w}}$ (see Eq. 3.4). Then, the average magnetization per monomer, m, is computed as [120]:

$$\langle m \rangle = \frac{1}{N} \frac{\sum\limits_{\mathrm{w} \in \mathrm{walks}} \sum\limits_{\{s_i = \pm 1\}}^{\mathrm{w}} |\sum\limits_{i=1}^{V} \sigma_i^{\mathrm{w}}| \; e^{\frac{\beta J}{2} \sum_{i,j=1}^{V} \sigma_i^{\mathrm{w}} \Delta_{i,j} \sigma_j^{\mathrm{w}}}}{\mathcal{Z}_N(h=0)} \,. \tag{3.11}$$

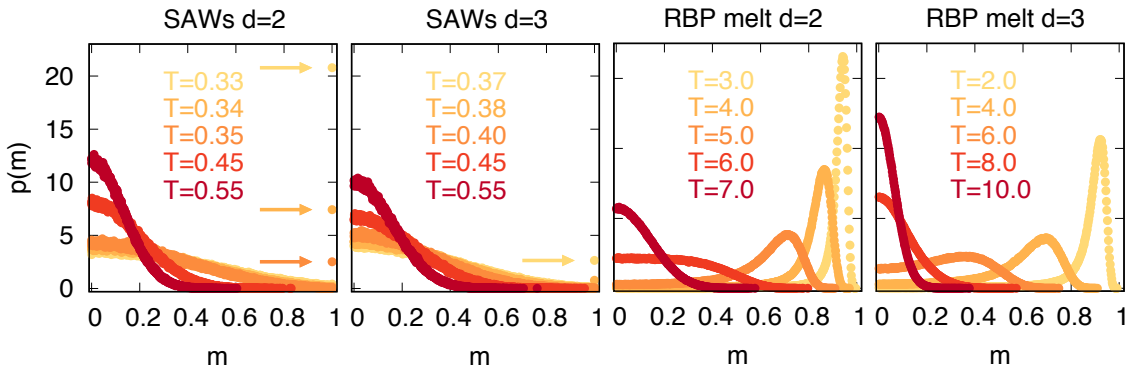

Figure 3.3: Probability distribution functions of magnetization per spin, m, and different temperature T. We notice the different behavior between SAW's and randomly branching polymers in melt. The arrows indicate the position of the "trivial" maxima for $m = 1$ at low temperatures. These curves were calculated for the largest polymer sizes available for each ensemble.

Results for $\langle m \rangle$ as a function of temperature T and for the different systems are shown in figure 3.2. Qualitatively, they appear consistent with the predictions of the mean-field theory: at increasing N, the range of temperatures where $\langle m \rangle \neq 0$ becomes steadily narrower for self-avoiding walks, with little differences between $2d$ and $3d$ systems. Melt of trees, instead, display the opposite trend: this is particularly evident for the $2d$ case where excluded-volume effects are stronger and, then, single chain compact behavior is more pronounced [23] than in the $3d$ case. Then, for consistency, we have calculated the probability distribution functions for m (figure 3.3). As expected, curves for SAW's are not consistent with the possibility of a phase transition having the maximum at $m = 0$ steadily decreasing. Conversely, curves for compact trees show the characteristic shape observed for (second-order) phase transitions [98], in particular the appearance of a non-trivial stationary point at low-enough temperatures.

Then, we have studied the scaling behavior of the critical temperature, $T_{max} = T_{max}(N)$, which is defined in correspondence of the maximum, $\langle \chi_{max} \rangle = \langle \chi_{max}(N) \rangle \equiv \langle \chi(T_{max}(N)) \rangle$, of the susceptibility per monomer, $\langle \chi \rangle = \langle \chi(T) \rangle$:

$$\langle \chi \rangle = \frac{1}{N} \frac{\sum_{\mathrm{w} \in \mathrm{walks}} \sum_{\sigma_i = \pm 1}^{\mathrm{w}} \left(|\sum_{i=1}^{N} \sigma_i| - N\langle m \rangle \right)^2 e^{\frac{\beta J}{2} \sum_{i,j=1}^{V} \sigma_i^{\mathrm{w}} \Delta_{i,j} \sigma_j^{\mathrm{w}}}}{\mathcal{Z}_N(h=0)} \,. \tag{3.12}$$

Typical curves for $\langle \chi \rangle$ on the same ranges of temperatures as in figure 3.2 are displayed in figure 3.4, while plots for $T_{max}(N)$ and $\langle \chi_{max}(N) \rangle$ are given in figure 3.5. Qualitatively, the temperatures (panel A) show the general trend predicted from the mean-field theory: while self-avoiding walks decay as $\sim N^{-0.143 \pm 0.007}$ and $\sim N^{-0.155 \pm 0.002}$ for $2d$ and $3d$ systems respectively, dense branched polymers seem to point towards a non-zero value of the critical temperature when $N \to \infty$, with $T_c(d = 2) > T_c(d = 3)$ as expected based on the larger number of contacts per

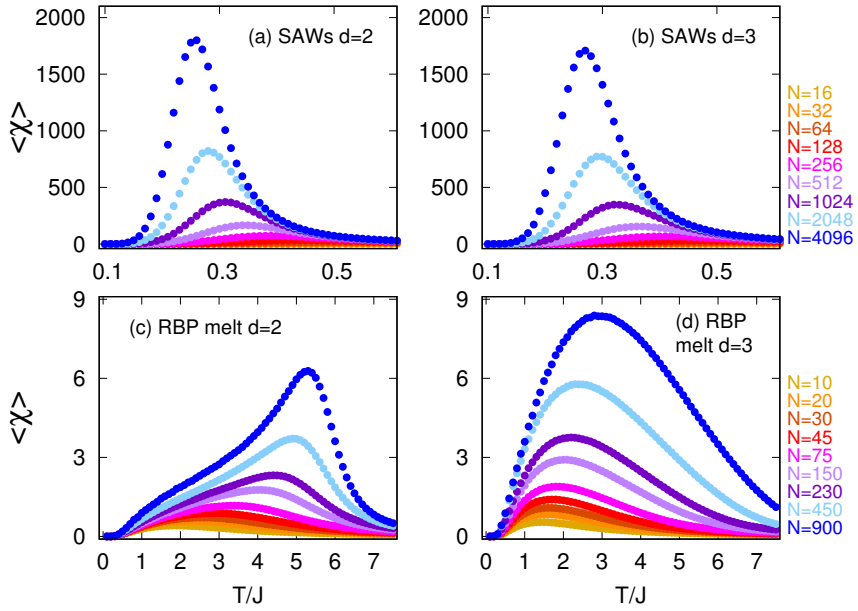

Figure 3.4: Average susceptibility per monomer, $\langle\chi\rangle = \langle\chi(T)\rangle$, as a function of temperature T, see definition Eq. 3.12. Symbols and color code are as in figure 3.2.

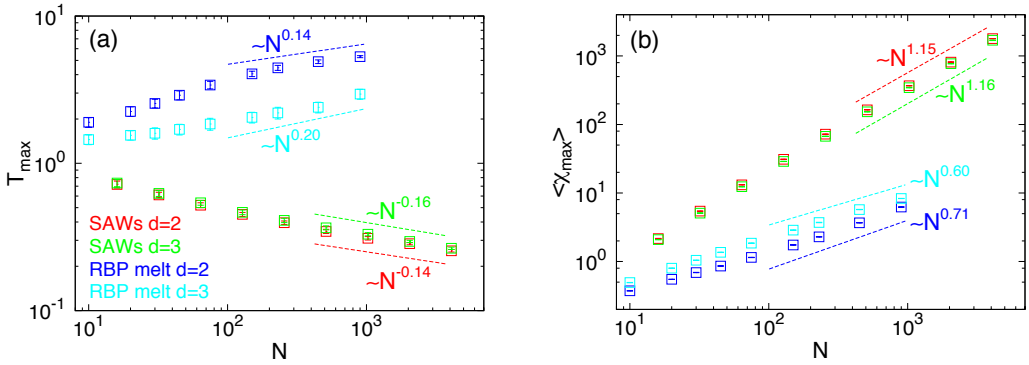

Figure 3.5: (a) N-dependence of temperatures, $T_{max}(N)$, at which the magnetic susceptibility is maximal. (b) Corresponding maximal values of the susceptibility $\langle\chi_{max}(N)\rangle \equiv \langle\chi(T_{max}(N))\rangle$. The slopes correspond to fits to single power law behavior using data with $N > 400$ (SAW's) and $N > 100$ (RBP melts).

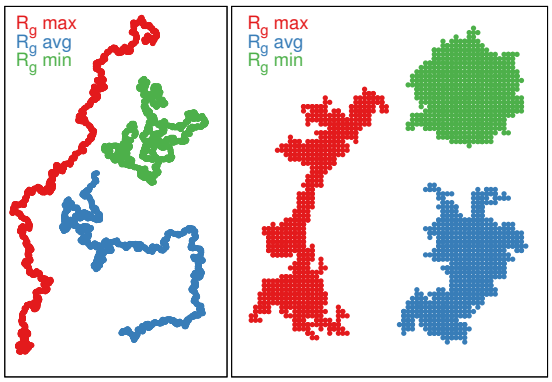

Figure 3.6: Examples of polymer conformations in $2d$, sorted according to minimal (green), close-to-average (blue) and maximal (red) gyration radius R_g. (Left) Self-avoiding linear walks ($N = 4096$). (Right) Randomly branching polymers in melt ($N = 900$).

monomer [115] displayed by $2d$ systems. Unfortunately, the quality of the data (especially for $3d$ systems) does not allow a reliable extrapolation of the critical temperature for the infinite system. This is probably due to the limited size of the polymers which can be simulated ($N \lesssim 900$). In the future then, it would be interesting to extend the present analysis to much bigger systems. Then (panel B), we have considered the scaling properties of $\langle \chi_{max}(N) \rangle$ *vs.* N: our analysis shows markedly different behavior of self-avoiding polymers ($\chi_{max}(N)_{2d} \sim N^{1.148 \pm 0.005}$ and $\chi_{max}(N)_{3d} \sim N^{1.161 \pm 0.008}$) in comparison to compact trees ($\chi_{max}(N)_{2d} \sim N^{0.71 \pm 0.01}$ and $\chi_{max}(N)_{3d} \sim N^{0.60 \pm 0.02}$). Curiously, the properties of the Ising model within the same class of polymers result to be only mildly affected by the dimension of the embedding space, for instance results for $2d$ and $3d$ SAW's are practically indistinguishable. This suggests that the local details of chain connectivity play a more crucial role in establishing whether a given polymer ensemble underlies a critical Ising transition.

3.3.5 Fluctuations

Notoriously [121], polymers are physical objects with fluctuating shapes. As the Ising model is constructed on the spatial vicinity of monomers, it is a relevant question asking how its properties change with respect to polymers belonging to the same ensemble but with very different shapes and/or linear sizes. Typical examples of $2d$ polymer conformations for SAW's and randomly branching polymers in melt are illustrated in figure 3.6, where we have considered the particularly instructive cases of chains with largest (*max*, red), closest-to-average (*avg*, blue) and smallest (*min*, green) gyration radius, $R_g \equiv \sqrt{1/(N+1)\sum_{i=1}^{N+1}(\vec{r}_i - \vec{R}_{cm})^2}$ where $\vec{R}_{cm} = 1/(N+1)\sum_{i=1}^{N+1}\vec{r}_i$ is the center of mass of the chain whose monomers have spatial coordinates $\vec{r}_i$. Unless otherwise specified, we are going to discuss results for the largest polymers available, namely $N = 4096$ for SAW's and $N = 900$ for melt of

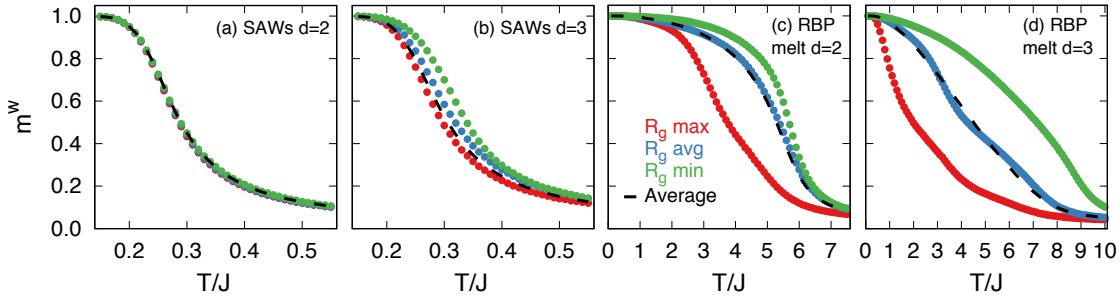

Figure 3.7: Average magnetization per monomer, $m^{\mathrm{w}} = m^{\mathrm{w}}(T)$, as a function of temperature T for polymer conformations with different gyration radii (color code is as in figure 3.6). The dashed black curve corresponds to the polymer ensemble average, $\langle m(T) \rangle$. The curves for SAW's show no ($2d$) or very little differences ($3d$), while the curves for melt of randomly branching polymers exhibit much larger fluctuations.

trees, and, for any given ensemble, we are going to consider the Ising model for the three conformations illustrated in figure 3.6.

Magnetization and susceptibility – Figures 3.7 and 3.8 show the magnetization ($m^{\mathrm{w}}(T)$) and susceptibility ($\chi^{\mathrm{w}}(T)$) curves (red, green, blue) for the selected polymer conformations as in figure 3.6 and the corresponding averages ($m(T)$ and $\chi(T)$) for the full polymer ensembles. We report none or only very little differences between these curves for the case of self-avoiding walks. As self-avoiding walks can be quite elongated and then almost one-dimensional (see figure 3.6), again this result points against the possibility of an ordinary phase transition taking place in these systems. Conversely, melts of randomly branching polymers exhibit much larger fluctuations: this is particularly evident for $\chi^{\mathrm{w}}(T)$ where the ratio between the values corresponding to the peaks of the curves may even exceed one order of magnitude.

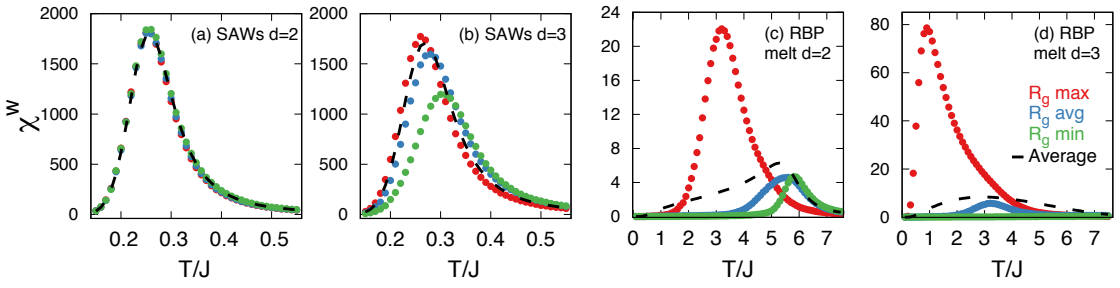

Figure 3.8: Average susceptibility per monomer, $\chi^{\mathrm{w}} = \chi^{\mathrm{w}}(T)$, as a function of temperature T for polymer conformations with different gyration radii (color code and symbols are as in figure 3.7). Curves for melts of randomly branching polymers exhibit large differences, the heights of the corresponding peaks being separated by more than one order of magnitude.

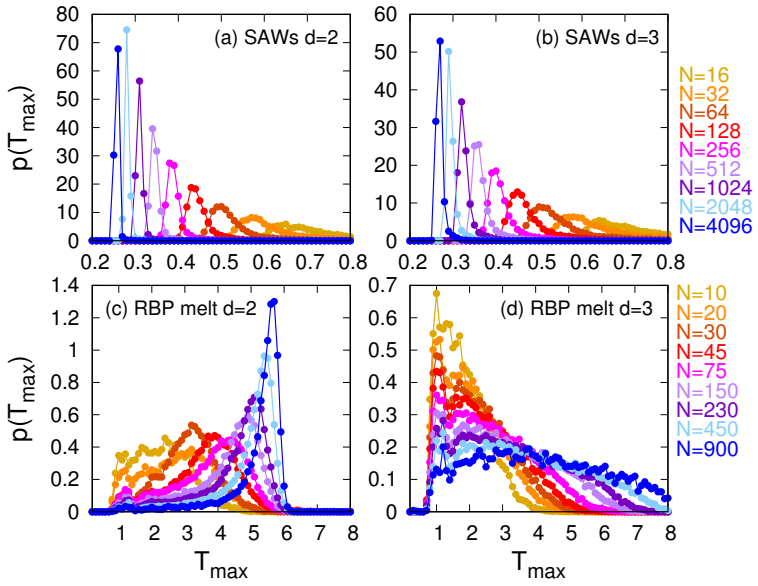

Figure 3.9: Probability distribution functions, $p(T_{max})$, of temperatures T_{max} defined in correspondence of the largest values of $\chi^{\mathrm{w}}(T)$.

Accordingly to figure 3.9, corresponding distribution functions, $p(T_{max})$, of temperatures at which the different $\chi(T)$'s attain the maximum value appear very different for the different ensembles. For $2d$ and $3d$ SAW's, distributions are strongly peaked with the value in correspondence of the peak shifting towards smaller values. This is in agreement with the results presented in section 3.3.4. Results for branched polymers display, instead, a more complex pattern: $2d$ systems also display peaked distribution, but now, and again in agreement with the results of section 3.3.4, the value of the maximum shifts towards *larger* T_{max}'s. For $3d$ systems, the shape of $p(T_{max})$ tends to become rather flat for the largest simulated systems: this makes extrapolation of the critical temperature for $N \to \infty$ difficult (see related results in figure 3.5). Again, the reason behind no clear trend is likely due to the limited size (up to $N = 900$) of polymer chains.

Statistics of spins clusters – Finally, we concentrate briefly on the statistical properties of *clusters* of spins. Here, a cluster is defined in terms of the spatial proximity of monomers whose spins have the same sign (either $+$ or $-$). Starting from a monomer of each polymer chain, nearest-neighbor spins are assigned to the same cluster if they have the same sign of the initial monomer. The process is repeated on the new monomers assigned to the cluster and stops when no further monomers can be added. Then, the monomers not belonging to the cluster are used as seeds for the construction of new clusters and so on.

To analyse the properties of the clusters, we study the following two quantities: the distribution function, $p(n_*)$, for cluster size, $n_* = n_+$ or $n_* = n_-$, and the distribution function of the total number of clusters, $p(n_{cl})$, per polymer chain. To fix the ideas, we have studied this quantity by fixing the temperature $T = T_{1/2}$ for which the ensemble-average magnetization per monomer $\langle m(T = T_{1/2})\rangle = 1/2$. Again, we

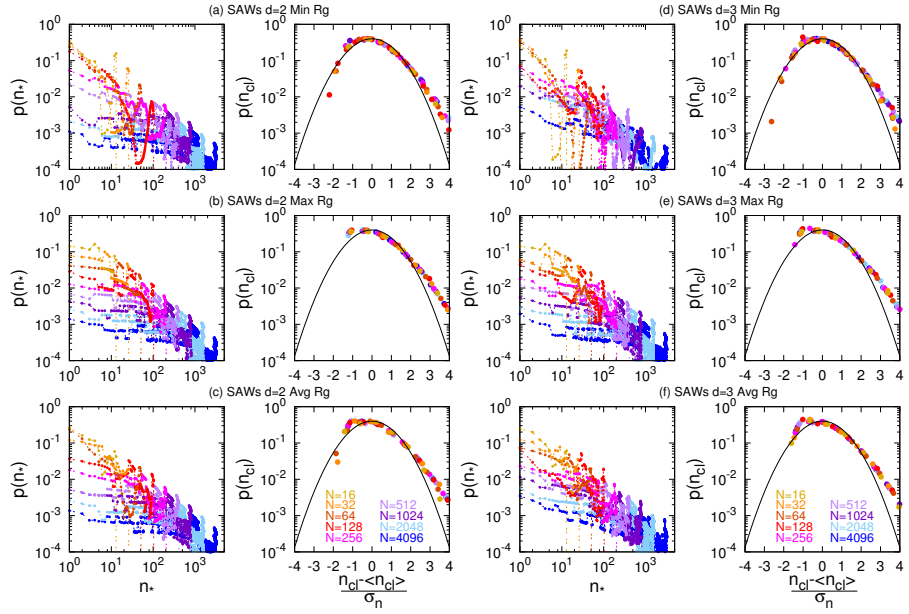

Figure 3.10: Characterization of clusters of spins with equal sign on single polymer conformations with different gyration radii R_g and at temperature $T_{1/2}$ for which the ensemble-average magnetization per monomer $\langle m(T = T_{1/2})\rangle = 1/2$: results for $2d$ and $3d$ SAW's. $p(n_*)$ is the distribution function for cluster sizes, $n_* = n_+$ or $n_* = n_-$. $p(n_{cl})$ is the distribution function for the number of clusters, n_{cl}, here compared to the Gaussian distribution (black solid line).

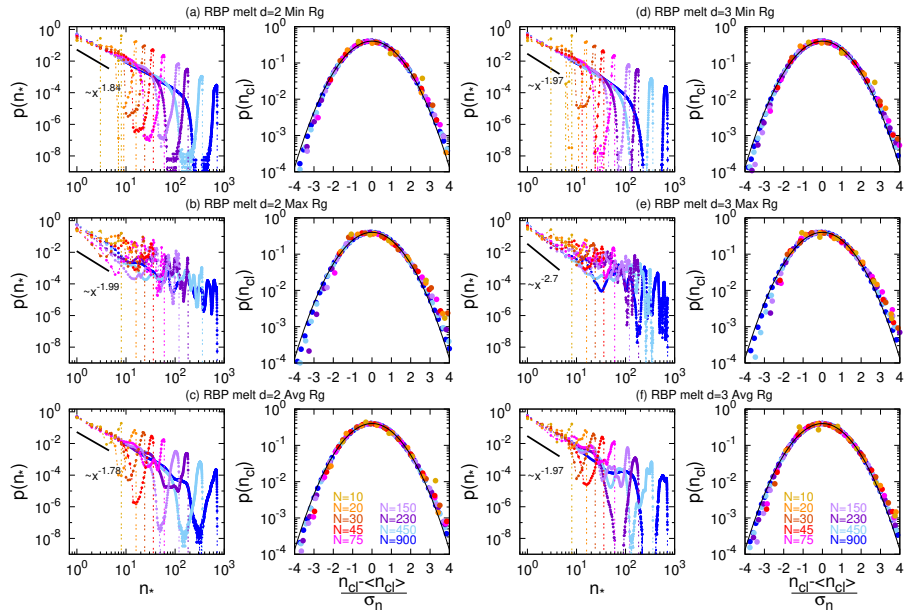

Figure 3.11: Characterization of clusters of spins with equal sign on single polymer conformations with different gyration radii R_g and at temperature $T_{1/2}$ for which the ensemble-average magnetization per monomer $\langle m(T = T_{1/2})\rangle = 1/2$: results for $2d$ and $3d$ randomly branching polymers in melt. Notation and symbols are as in figure 3.10.

have carried out separate analysis for polymer conformations with different gyration radii.

Figures 3.10 and 3.11 display our results for SAW's and randomly branching polymers in melt, respectively. In the former case, $p(n_*)$ converges to an almost-flat distribution in all three cases studied, while $p(n_{cl})$ is cut at small n_{cl} and very different from the Gaussian distribution (black line). Conversely, for branched polymers $p(n_*) \sim n_*^{-\gamma}$ with $1 < \gamma \lesssim 2$ and $p(n_{cl})$ overlaps with the Gaussian distribution.

3.4 Conclusions

In this Chapter we have considered the problem of the classical Ising model on a lattice polymer chain in d dimensions, with nearest-neighbor interactions between spins being ruled by both polymer internal connectivity and chain folding in the embedding space.

The problem has been studied by first employing a mean-field analytical approach (section 3.3.1). This calculation shows that for typical polymers whose fractal dimension $= 1/\nu$ is larger than the space dimension d, the polymer can not sustain the transition to ferromagnetic behavior. The opposite is true for compact polymers, where $1/\nu = d$.

In order to validate the predictions of the mean-field theory, we have performed Monte Carlo computer simulations of the Ising model in single polymer chains in $d = 2, 3$ dimensions: as typical examples of swollen polymers ($1/\nu > d$) we have considered ordinary self-avoiding walks, while the recently introduced randomly branching polymers in melts provide the test case for compact statistics ($1/\nu = d$).

In general agreement with the predictions of the mean-field theory (section 3.3.4, figures. 3.2 to 3.5), we confirm that SAW's do not display the traditional signatures of a ferro-magnetic transition. Conversely, the Ising model in compact polymers displays a marked different behavior compatible with the onset of a phase transition.

To complete the picture, we have then carried out a detailed analysis of the ordered phase on single chain conformations (section 3.3.5). In particular, we underscore that there exist no or only very modest variations for the same observables calculated on SAW's of very distinct shapes (figures. 3.7 and 3.8, top panels), while differences between randomly branching polymers in melt appear much sharper (figures. 3.7 and 3.8, bottom panels).

Chapter 4

General Principles of Microrheology

In this Chapter[1] we will review the principles of microrheology [41, 122, 123, 124, 125, 126] a powerful tool for characterizing the viscoelastic properties of complex fluids. First, we will summarize the main theoretical ideas, afterwards we will concentrate on the scaling theory, developed firstly by Brochard-Wyart and de Gennes [127] for polymer melts and then extended by Rubinstein and co-workers [128, 129].

4.1 Single Particle Tracking

Particle tracking microrheology is a powerful technique for the measurement of viscoelastic properties of complex fluids which can not be investigated with macrorheology and gives information about spatial heterogeneity at a microscale. Microrheology (MR) is based on the tracking of the Brownian motion of fluorescent nanoprobes (an example where the MR methodology has been applied to living cells is reported in figure 4.1) injected inside the sample volume as a proxy for the viscoelastic properties of the embedding medium. Compared to standard (bulk) rheology, microrheology grants systematic screening over wide ranges of length and time scales for the feasibility of designing trackable nanoprobes of linear sizes ranging from only a few nanometers [130] to hundreds of nanometers [123] and microns [131]. Microrheology is nowadays especially suitable for studies of biological materials [126] since, being minimally invasive, it allows to perform experiments *in vivo* and with very small samples [124].

Experimental data for microrheology can be obtained by various means, such as dynamic light scattering (DLS) [132]. More commonly, the motion of the probe in the form of its spatial coordinates can be recorded through direct imaging and transformed into the time mean-square displacement (MSD) of the probe, $\langle \Delta x^2(\tau) \rangle \equiv \frac{1}{\mathcal{T}-\tau} \int_0^{\mathcal{T}-\tau} (\vec{x}(t+\tau) - \vec{x}(t))^2 dt$, where $\mathcal{T}$ is the measurement time and τ the lag-

[1]Part of the material described in this Chapter has been published as a Chapter "Structure and Microrheology of Genome Organization: From Experiments to Physical Modeling" in the book *Modeling the 3D Conformation of Genomes*, CRC Press (2019) [41]

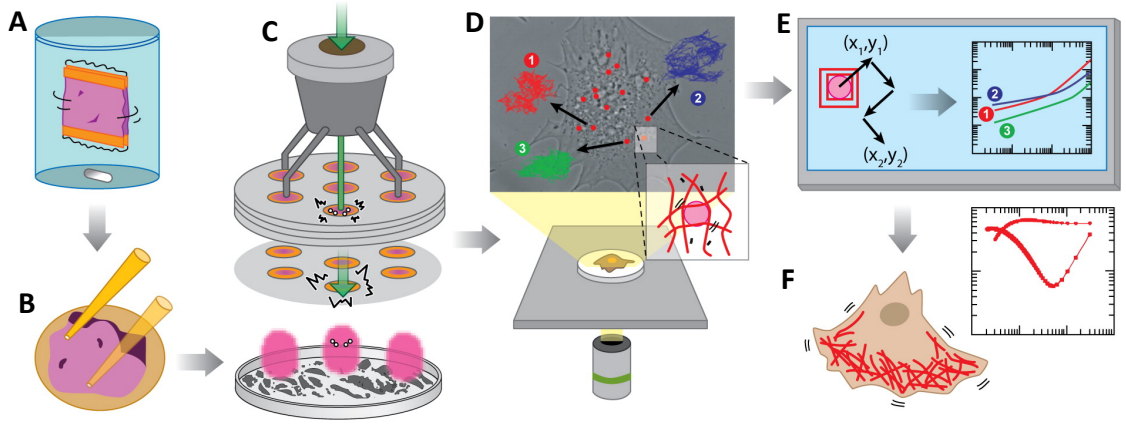

Figure 4.1: Sequential steps in microrheology: (A) After the initial preparation of the sub-micron fluorescent probes, (B) the beads are spread on a grid and (C) ballistically injected inside the cytoplasm where they rapidly disperse. (D) The cells are then placed under a fluorescence microscope and the random motion of the probes is monitored with high spatial and temporal resolutions. Examples of three trajectories are shown in red (1), blue (2), green (3). (E) The recorded time-dependent coordinates, $\vec{x}(t)$, of the probes are transformed into time-lag mean-square displacements (MSDs). (F) Finally, the MSDs of the probes are used to derive the local values of the frequency-dependent storage, $\hat{G}'(\omega)$, and loss, $\hat{G}''(\omega)$, moduli of the cytoplasm and/or the nucleoplasm. Reproduced from reference [122].

time [133]. In fact, the MSD constitutes an important source of information concerning the nature of the environment [133]. For instance, in a thermally fluctuating, purely viscous medium, nanoprobe motion is described by standard diffusion with $\langle x^2(\tau)\rangle \sim D\tau$ where D is the diffusion coefficient. Instead, in complex and disordered media [133, 134, 135], nanoprobes can behave quite differently: in general, $\langle x^2(\tau)\rangle \sim D_\alpha \tau^\alpha$ with $\alpha \neq 1$ and D_α is the "generalized" diffusion coefficient.

Then, the viscoelasticity of the embedding medium and nanoprobe motion are connected by the following mathematical relation [136]:

$$\hat{G}(\omega) = -i\frac{2\kappa_B T}{\pi d\,\omega\,\langle \Delta\hat{x}^2(\omega)\rangle}\,. \tag{4.1}$$

the demonstration of which is given in the Appendix A.3.1.

Here: $i = \sqrt{-1}$ is the imaginary unit; κ_B is the Boltzmann constant; T is the absolute temperature; d is the nanoprobe diameter; $\langle \Delta\hat{x}^2(\omega)\rangle$ is the Laplace-Fourier (LF) transform[1] of $\langle \Delta x^2(\tau)\rangle$ (ω is the frequency). $\hat{G}(\omega) \equiv \hat{G}'(\omega) + i\hat{G}''(\omega)$ is the complex *shear modulus* of the medium: its real ($\hat{G}'(\omega)$) and imaginary ($\hat{G}''(\omega)$) parts correspond to the storage (elastic) and loss (viscous) moduli [2], respectively.

To illustrate the method, we consider the general situation where nanoprobe diffusion is power-law-like [134]: $\langle \Delta x^2(\tau)\rangle = 6D_\alpha\,\tau^\alpha$, where D_α is the (generalized)

[1] The Laplace-Fourier (LF) transform of a generic time-dependent function $f = f(t)$ is defined as $\hat{f}(\omega) \equiv \int_0^\infty e^{-st} f(t)|_{s=i\omega}$ where $i = \sqrt{-1}$.

diffusion coefficient ($0 \leq \alpha \leq 1$) and τ is the lag-time. With the corresponding LF-transform given by $\langle \Delta\hat{x}^2(\omega) \rangle = 6D_\alpha \, \Gamma(\alpha+1) \, (i\omega)^{-(\alpha+1)}$, $\hat{G}'(\omega)$ and $\hat{G}''(\omega)$ are expressed by the simple formulas:

$$\hat{G}'(\omega) = \frac{\kappa_B T}{3\pi d} \, \frac{\cos(\pi\alpha/2)}{D_\alpha \, \Gamma(\alpha+1)} \, \omega^\alpha \,, \quad \hat{G}''(\omega) = \frac{\kappa_B T}{3\pi d} \, \frac{\sin(\pi\alpha/2)}{D_\alpha \, \Gamma(\alpha+1)} \, \omega^\alpha \,. \tag{4.2}$$

The two "special" limits of $\alpha = 0$ and $\alpha = 1$ correspond, respectively, to the well-known cases of $\hat{G}(\omega) = \hat{G}'(\omega) = const = \frac{\kappa_B T}{3\pi d \, D_0}$ and $\hat{G}(\omega) = i\hat{G}''(\omega) = i\frac{\kappa_B T}{3\pi d \, D_1}\omega \equiv i\eta\omega$. In the former case the medium responds as an elastic (Hookean) solid, while in the latter its behavior is as of a classical fluid with "bulk" viscosity $= \eta$. In the intermediate case of $0 < \alpha < 1$ both, $\hat{G}'(\omega)$ and $\hat{G}''(\omega)$, are non-zero and the medium displays intermediate (solid/liquid) properties. The last case is particularly relevant to the cellular context. In fact, a growing number of experimental studies employing single-particle tracking of fluorescently-labeled chromatin loci [137, 138] has demonstrated that loci dynamics is typically subdiffusive [139] and, at least in some cases, ATP-dependent [140, 141]. From the physical point of view, subdiffusion can be ascribed either to the macromolecular crowding of the nucleus [142, 143] which obstructs free chromatin motion or to the polymer-like nature of the chromatin fiber [144], or, most likely, to a combination of both.

4.2 A case study: Scaling Theory for Microrheology in Entangled Polymer Solutions

Along this Chapter we have described the peculiarities of microrheology as a powerful tool capable of detecting a wide range of phenomenology. In particular, this framework can be also employed to investigate the viscoelastic properties of polymeric fluids. In this section we will review a theoretical description of the dynamics of nanoprobes embedded in a polymer solution based on the scaling theory which has been developed firstly by Brochard-Wyart and de Gennes [127] for the case of polymer melts and then extended by Rubinstein and co-workers [128, 129].

Similarly to the experimental set up, nanoparticles are dispersed in a polymer solution: the dynamics of the system is affected by the topological constraints (TCs) of the polymer chains themselves, which prevent single chains to cross each other, and, consequently, also by their long relaxation times. Indeed, the mobility of nanoparticles is strongly coupled to the relaxation dynamics of the surrounding polymers and exhibits a non-trivial scaling behavior which depends on various factors.

Consequently, the scaling theory is founded on the premise that the mobility of the nanoparticles of size d diffusing through the crowding of the polymer liquid with volume fraction ϕ depends on two important length scales:
(a) the *correlation length*, ξ, defined as the average distance between a monomer on one chain to the nearest monomer on another chain;
(b) the *tube diameter*, d_T (or equivalently the entanglement length), for the definition see section 1.1.4.

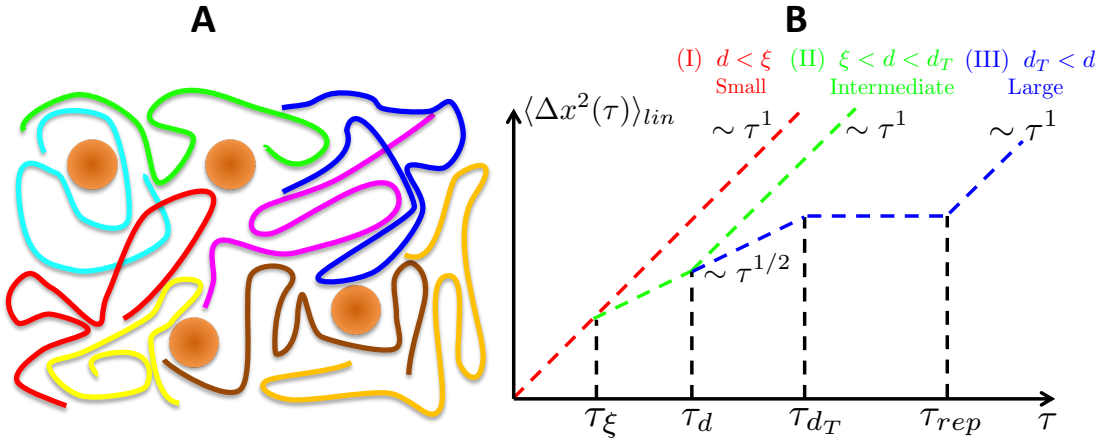

Figure 4.2: (A) Schematic illustration of nanoprobes embedded in a solution of entangled linear polymers. (B) Time mean-square displacement $\langle \Delta x^2(\tau) \rangle_{lin}$ of nanoprobes in solutions of entangled linear polymers , in log-log scales.

In addition, also the specific chain architecture of the surrounding polymers has a crucial effect on the nanoparticles dynamics [10, 145, 146]. In this section we will review the scaling theory focusing on two different cases of study, entangled solutions of linear chains vs. unknotted and unconcatenated ring chains whose different behaviours have a role in the dynamics of nanoparticles. As we have already seen in section 1.1.5, there are relevant differences, entangled unconcatenated ring polymers adopt self-similar, compact conformations and do not perform reptation unlike the entangled linear polymers with almost Gaussian random-walk conformations. Indeed, it has been shown that nanoparticles with sizes larger than the mesh size of the solution move faster in solutions of rings than in solutions of linear chains [10, 145, 146].

4.2.1 Nanoparticle Diffusion in Entangled Linear Polymer Solution

So far we have pointed out that the averaged time (τ) dependent mean square displacement (MSD) $\langle \Delta x^2(\tau) \rangle$ is crucial to capture the physics behind the browian motion of nanoparticles. In this section we focus on the diffusion of nanoparticles in solution of entangled linear polymer. Depending on nanoprobe diameter three regimes (figure 4.2, panel (B)) can be distinguished [128, 129, 145, 146]:

I) **Small nanoparticles**, $d < \xi$.
If the diameter is smaller than the solution correlation length' ξ, nanoparticles interact only with the solvent, and their motion remains diffusive:

$$\langle \Delta x^2(\tau) \rangle \sim D_s \, \tau \sim \frac{\kappa_B T}{\eta_s \, d} \, \tau \, . \tag{4.3}$$

D_s is the diffusion coefficient and η_s is the viscosity of the solvent.

II) **Intermediate nanoparticles**, $\xi \lesssim d \lesssim d_T$. If the diameter is larger than the correlation length but smaller than the tube diameter d_T, nanoparticles motion is now affected by the polymers, showing three different regimes:

$$\langle \Delta x^2(\tau) \rangle_{lin} \sim \begin{cases} D_s\,\tau, & \tau < \tau_\xi \sim \frac{\eta_s \xi^3}{\kappa_B T} \quad \text{(II.a)} \\ D_s \tau_\xi \left(\frac{\tau}{\tau_\xi}\right)^{1/2}, & \tau_\xi < \tau < \tau_d \sim \tau_\xi \left(\frac{d}{\xi}\right)^4 \quad \text{(II.b)} \\ D_s \left(\frac{\xi}{d}\right)^2 \tau, & \tau > \tau_d \quad \text{(II.c)} \end{cases} \tag{4.4}$$

In (II.a), nanoparticles motion is driven only by random collisions with the solvent, as for small nanoparticles. This regime stops at τ_ξ, which corresponds to the relaxation time of a polymer strand of spatial size ξ. Then (II.b), the nanoprobe experiences a time-dependent viscosity $\eta(\tau) \sim \eta_s\, n_{str}(\tau) \equiv \eta_s\, (\tau/\tau_\xi)^{1/2}$, where $n_{str}(\tau)$ is the number of strands which have relaxed at time τ. This regime stops at time τ_d, the relaxation time of a larger polymer strand of spatial size $d = \xi \sqrt{n_{str}(\tau_d)}$. Above τ_d (II.c), nanoparticles dynamics becomes diffusive again with effective viscosity $\sim \eta_s\, n_{str}(\tau_d)$, which is $\sim (d/\xi)^2$ times *larger* than the value in pure solvent.

III) **Large nanoparticles**, $d \gtrsim d_T$.
Even for nanoparticles with diameter larger than the tube diameter, equation (II.a) holds, while the regime described by equation (II.b) stops at $\tau_{d=d_T} = \tau_\xi\, (d_T/\xi)^4$. Above τ_{d_T}, entanglements affect nanoparticles motion which results to be trapped and their MSD exhibits a plateau: $\langle \Delta x^2(\tau) \rangle_{lin} = \langle \Delta x^2(\tau_{d_T}) \rangle_{lin} \approx D_s \left(\frac{\xi}{d_T}\right)^2 \tau_{d_T} \approx \frac{\xi}{d} d_T$ which depends on all three relevant time scales of the system. Neglecting hopping between close-by entanglements, this regime holds until the complete chain reptation at time $\tau \sim \tau_{rep} \sim \tau_e \left(\frac{L_c}{L_e}\right)^3$. The entanglement time τ_e corresponds to the relaxation time scale of a polymer chain with contour length L_e. In contrast, at larger times, nanoparticles dynamics becomes diffusive again, and it MSD is:

$$\langle \Delta x^2(\tau) \rangle_{lin} \approx \frac{\kappa_B T}{\eta_{bulk} d} \tau \approx \frac{\xi}{d} d_T^2 \left(\frac{L_c}{L_e}\right)^{-3} \frac{\tau}{\tau_e}. \tag{4.5}$$

4.2.2 Nanoparticle Diffusion in Unknotted and Unconcatenated Ring Polymer Solution

Nanoparticles dynamics in solution of entangled unconcatenated ring polymers exhibit some differences if compared with the ones in linear chains. Since ring and linear polymers have a similar behaviour on length scales smaller than the tube diameter d_T, the dynamics of nanoparticles with small and intermediate sizes $d < d_T$ can be described by the same equations 4.3 and 4.4 developed for the previous case of nanoparticles embedded in linear chains.

The scenario is different in the case of large nanoparticles, $d \gtrsim d_T$: the dynamics at time scales greater than τ_{d_T} reflects the different spatial organization of rings compared to linear polymers (see figure 4.3).

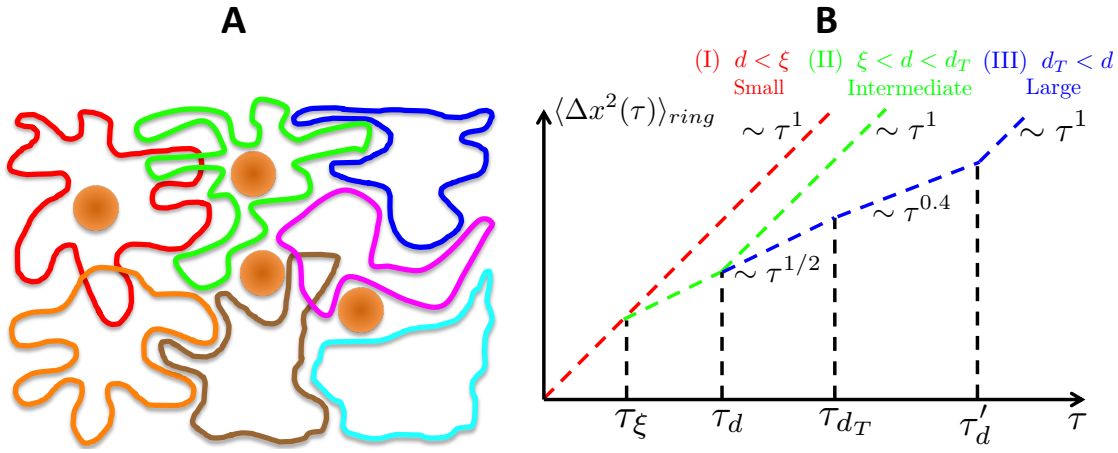

Figure 4.3: (A) Schematic illustration of nanoprobes embedded in a dense solution of ring polymers. (B) Time mean-square displacement $\langle \Delta x^2(\tau) \rangle_{ring}$ of nanoprobes in solutions of ring polymers, in log-log scales.

In this case, by scaling arguments [2], the time-dependent friction $\eta = \eta(\tau) \approx \tau G(\tau)$ where: $G(\tau) \sim \frac{\kappa_B T}{\nu^{2/3} L(\tau)}$ is the stress relaxation modulus, ν is the monomer volume and $L(\tau) \sim L_e \left(\tau/\tau_e\right)^{1/\gamma}$ ($\gamma = 2.33$-2.57, as reported in references [28, 147, 148]) is the contour length of the polymer strand with relaxation time τ. Therefore,

$$\langle \Delta x^2(\tau) \rangle_{ring} \sim \frac{\kappa_B T}{\eta(L(\tau))d}\,\tau \sim \frac{\nu^{2/3} L_e}{d}\left(\frac{\tau}{\tau_e}\right)^{1/\gamma}, \tag{4.6}$$

and nanoprobe diffusion is anomalous with exponent $1/\gamma = 0.39$-0.43. This regime breaks down at $\tau'_d \sim \tau_e \left(d^2/(\ell_K L_e)\right)^{3\gamma/2} = \tau_e \left(d^2/(\ell_K L_e)\right)^{3.50-3.86}$, the relaxation time of a ring strand of spatial extension $\approx d$ in the compact regime. For $\tau > \tau'_d$, nanoprobe diffusion is normal with $\langle \Delta x^2(\tau) \rangle_{ring} \sim \frac{\kappa_B T}{\eta(L(\tau'_d))d}\,\tau$.

In the following Chapters we will discuss the application of microrheology to the dynamics of nanoprobes injected in cell nuclei, and to the case of theoretical models for out-of-equilibrium polymeric systems.

Chapter 5

A Model for the Microrheology of the Nucleus

As explained in Chapter 2, the interior of the nucleus constitutes a complex environment, filled by chromatin and other constituents. Inside this environment, proteins and other bodies move and interact with the different parts of the nuclear regions. In order to quantify how these molecules spread in time, several experimental assays have been developed. Notably, microrheology (described in Chapter 4) appears a promising tool to characterize the response of the bodies immersed in the nucleus.

The content of this Chapter[1] focuses on a possible extension of the study proposed by Valet and Rosa [150] where microrheology has been applied to the polymer model refined by Rosa and Everaers [69], introduced in section 2.2.1 for the description of chromosome territories.

First, we will introduce the major experimental applications of microrheology to the nuclei of eukaryotic cells, then we will review the main results from reference [150], where the viscoelastic properties of the nucleus have been compared to the dynamic behavior of nanoprobes immersed in a ring polymers solution. Although this model is in good quantitative agreement with theoretical expectations and in qualitative agreement with available experiments for nuclear microrheology, it has some limitations, such as, for example, the absence of the typical cage-and-escape dynamics.

To overcome some of these limitations, we will introduce a simple polymer model which takes into account the stable interactions between the chromatin fibers within the interior of the nucleus of the cell and the nucleoskeleton, an ensemble of "extra-chromatin" structures which help ensuring genome stability. Although the role of these interactions appears crucial to the correct behavior of the cell, their impact on chromatin structure and dynamics remains to be elucidated. This model will

[1] The material described in the first part of the current Chapter has been published inside the Chapter "Structure and Microrheology of Genome Organization: From Experiments to Physical Modeling" in the book *Modeling the 3D Conformation of Genomes*, CRC Press (2019) [41]. The results reported in last sections of the present Chapter has been published in: Papale A., Rosa A., *Physical Biology*, vol 16, p 066002 (2019) [149].

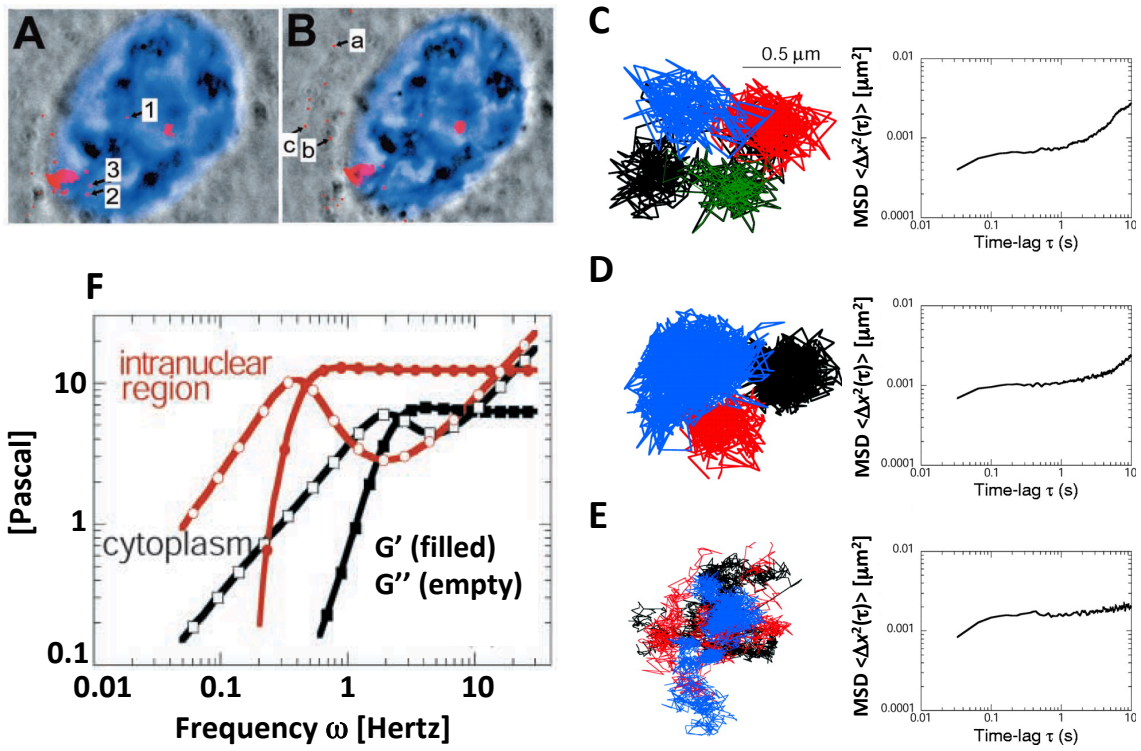

Figure 5.1: Microrheology of mammalian cells (Swiss 3T3 fibroblasts (mouse)). (A,B) Spatial localization of injected spherical nanoprobes (in red, nanosphere diameter = 100nm) within the cell. DAPI-stained DNA appears in blue and identifies the nucleus. The rest of the cell appears in gray. (1-3) and (a-c) are nanoprobes within the nucleus and the cytoplasm, respectively. (C-E) Typical trajectories (left) and corresponding mean-square displacements (right) for nanoprobes within the nucleus (C,D) and the cytoplasm (E). Different colors correspond to different nanospheres. (F) Corresponding storage ($\hat{G}'(\omega)$, filled symbols) and loss ($\hat{G}''(\omega)$, empty symbols) moduli (see section 4.1 for definitions). Reproduced from reference [123].

consider the two generic properties of chain-vs-chain mutual uncrossability and the presence of stable binding interactions to an extra-chromatin nuclear matrix.

5.1 Microrheology of the Nucleus

In general, the nucleus of eukaryotic cells is crowded with chromatin, proteins and other complexes: while the former is typically confined to specific regions of the nucleus, the latter are mostly mobile so to target selected chromatin sequences. How proteins or complexes diffuse inside the nucleus is enormously important. Microrheology can give an important contribution clarify this phenomenon.

To our knowledge, the first microrheological studies in living cells are ascribable to Tseng *et al.* [123, 151] (see figure 5.1) who measured the viscoelastic properties of the cytoplasm and the intranuclear region of mouse cells (Swiss 3T3 fibroblasts).

Yellow-green fluorescent spherical nanoprobes of 100nm diameter were microinjected within the cytoplasm and their trajectories tracked inside the nucleus and the perinuclear region of the cytoplasm, see figure 5.1 panels A and B. There are important differences in the two situations. Nanospheres fluctuating in the crowded nuclear region have trajectories which do not overlap, (see figure 5.1 panels C and D, left), showing **caged-and-escape** motion. On the contrary, (see figure 5.1 panel E, left), nanospheres moving inside the cytoplasm show extensive overlap. The corresponding mean square displacements (MSDs) reflect these differences (see figure 5.1 panels C-E, right): MSD of nanoprobes diffusing inside the nucleus grows with τ on short time scales ($[0 - 0.1]$ seconds), then shows a plateau ($[0.1 - 1]$ s), and finally grows again at large lag-times, in agreement with the "caged-and-escape" motion between confining domains of average linear size $\approx$ 290nm. Conversely, the plateau displayed by cytoplasmic nanospheres takes a higher value and reflects the restricted motion inside the cell. Finally, MSDs were used to calculate the complex shear modulus (figure 5.1 panel F) using 4.2. whose real ($G'(\omega)$, full symbols) and imaginary ($G''(\omega)$, open symbols) parts correspond to the storage and loss moduli of the medium embedding the nanoprobes. Qualitatively, the curves for the cytoplasm and the nucleoplasm have similar shapes. Quantitatively, by comparing the plateau values for $G'(\omega)$ the nucleoplasm is $\approx 2\times$ stiffer under shear than the cytoplasm. Moreover, the low viscosity of the cytoplasm compared to the nucleus should facilitate the transport of proteins and molecules from and to the nucleus. At the same time, nuclear viscosity, higher if compared to cytoplasm, might play an active role in chromosome reorganization during interphase.

While the work by Tseng *et al.* focuses on passive diffusion within the cytoplasm or the nucleus, the motion of a large number of macromolecular nuclear bodies and subnuclear organelles like transcription compartments (TCs), promyelocytic leukemia (PML) nuclear bodies or Cajal bodies (CBs) which are involved in transcriptional regulation or RNA processing results from the combination of both, passive and active (*i.e.*, energy-consuming) processes [152, 153, 154]. Moreover, recent work in bacteria [140] suggests that consumption of ATP increases the mobility of cellular bodies and chromatin more steeply with temperature in untreated cells than in ATP-depleted cells.

In order to understand the role of active processes on nuclear dynamics and the motion of nuclear bodies, Hameed *et al.* [131] compared the passive motion of nanoprobes to the driven motion of transcription compartments (TCs). TCs are chromatin domains with an open chromatin structure which partially colocalize to active "transcription factories". During this process and at physiological temperatures (37°C), they undergo directed movements which are influenced by ATP-dependent chromatin remodeling processes [155], and which are suppressed at lower, non-physiological temperatures.

To characterize the motion of TCs, Hameed *et al.* tracked nanoprobes of linear size = 1μm microinjected within the nuclei of HeLa cells at 25°C by using a protocol similar to the one by Tseng *et al.* (figure 5.2 panel A). The results are in quantitative agreement with those reported in the former work, in particular nanoprobe motion is caged within domains of linear size $\approx$ 250nm (figure 5.2 panel B), a value remark-

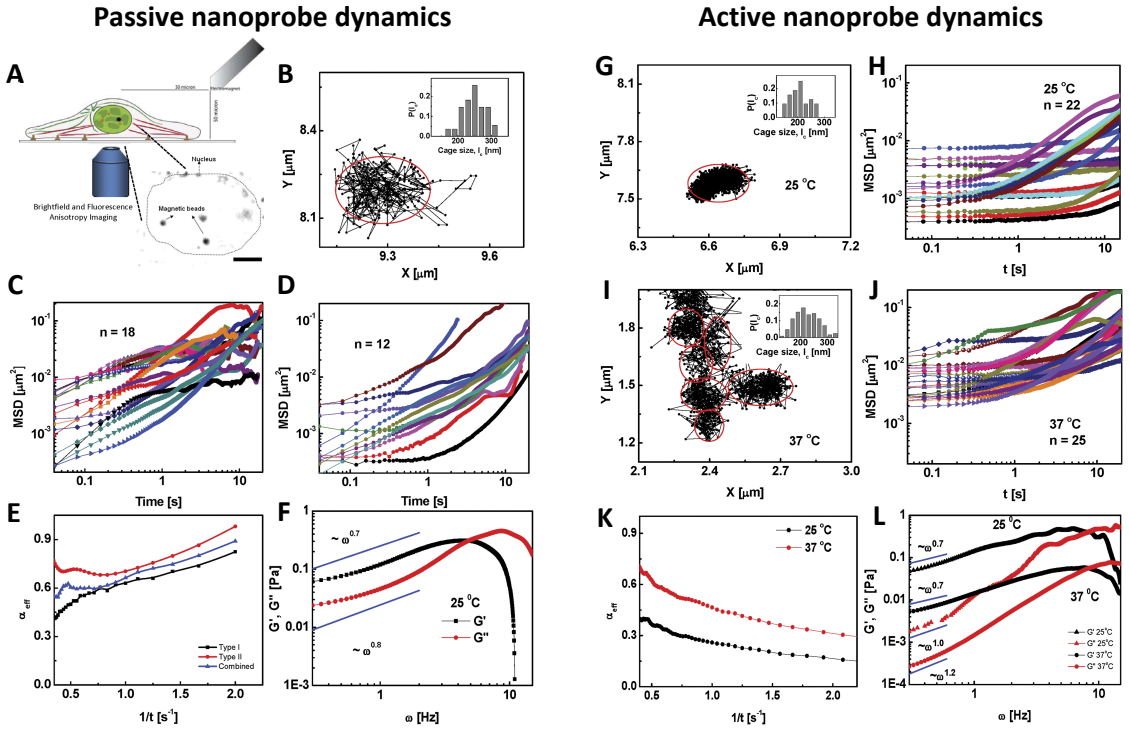

Figure 5.2: Microrheology of mammalian nuclei (live HeLa cells (human)): passive (A-F) *vs.* active (G-L) dynamics. (A) Schematic illustration of the experimental setup used for single-particle tracking. (B) Typical trajectory of a nanoprobe at 25°C showing diffusion in a confined cage. Inset: Histogram of cage sizes l_c. (C,D) Time mean-square displacements (MSDs) for different nanoprobes, displaying behavior I (C, plateauing at large times) and II (D, monotonically increasing). (E) Mean effective exponents α_{eff} ($\mathrm{MSD}(\tau) \sim \tau^{\alpha_{eff}}$) as a function of inverse time for trajectories I and II and their combination. (F) Storage and loss moduli, $G'(\omega)$ and $G''(\omega)$ as functions of frequency ω. At low ω's the nucleus is elastic ($G' > G''$) while becoming increasingly viscous at higher ω's. (G) Typical trajectory of a transcription compartment (TC) at 25°C showing diffusion in a confined cage as for microinjected beads. Inset: Histogram of cage sizes l_c. (H) Time MSDs for different TCs at 25°C. (I) Typical trajectory of a TC at 37°C showing diffusion in confined cages intermitted with jumps even across long distances. (J) Time MSDs for different TCs at 37°C. (K) Mean effective exponents α_{eff} as functions of inverse time for the two temperatures. (L) Storage and loss moduli, $G'(\omega)$ and $G''(\omega)$, as functions of frequency ω for the two temperatures. Reproduced from reference [131].

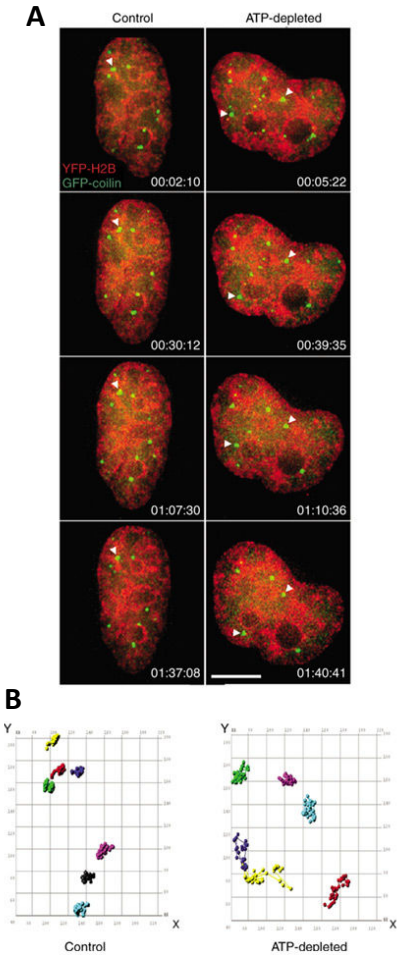

Figure 5.3: Diffusion of Cajal bodies (CBs) through the nuclear interchromatin space is an APT-dependent process. (A) Examples of consecutive temporal frames of nuclei of HeLa live cells: a healthy (control) nucleus (left) *vs.* an ATP-depleted nucleus (right). CBs are stained green, while chromosomal DNA is stained red. Consecutive positions of CBs are indicated by the white arrowheads. CBs in ATP-depleted nuclei show higher mobility and they are no longer associated with dense chromatin regions. Scale bar $= 10\mu$m. (B) Reconstructed trajectories of individual CBs. Different colors correspond to different CBs. Reproduced from reference [153].

ably close to the one ($\approx$ 290nm) measured by Tseng *et al.* in murine fibroblasts. Furthermore, single trajectories can be clustered into two groups according to the long-time behaviors of corresponding MSDs: in the first group, MSDs are plateauing at large times while in the second they steadily increase (figure 5.2 panels C-E). The analysis is finally completed by computing the storage and loss moduli, $G'(\omega)$ and $G''(\omega)$ (figure 5.2 panel F): the nucleus behaves like a "power-law" solid ($G' > G''$) at low frequencies (again, in qualitative agreement with the experiments by Tseng *et al.*) crossing to viscous-like behavior at large frequencies. The procedure was then repeated at 37°C with analogous results.

Next, passive nanoprobe motion was compared to the motion of TCs at the same two temperatures. As anticipated above, at the non-physiological temperature of 25°C, TC motion loses directionality and becomes similar to passive motion of nanoprobes with analogous confinement and dispersion of MSD curves (figure 5.2 panels G and H). Conversely, trajectories taken at 37°C display "mixed" behavior of confined motion and jumps between close-by cages (figure 5.2 panels I and J), analogous to the results for passive nanoprobes in murine fibroblasts discussed before and significantly larger mobility (figure 5.2 panel K). Accordingly (figure 5.2 panel L), curves for storage and loss moduli at 25°C are qualitatively similar to the

ones for passive nanoprobes, while at the higher temperature they show a drastic change with the nuclear environment becoming sensibly much softer to TC motion. The temperature dependent behavior is dramatically affected by ATP-depletion and perturbations to chromatin remodeling processes [131], suggesting that TC motion is partially stimulated by an active component.

Interestingly, the dynamic behavior of TCs constrasts analogous results [153] for the motion of Cajal bodies (CBs) in healthy (normal) and ATP-depleted nuclei. CBs are dynamic structures implicated in RNA-related metabolic processes. They can diffuse inside the nucleus, merge or split to form larger or smaller CBs and even associate/dissociate with/from specific genomic loci [153]. These processes were investigated in normal cells and in ATP-depleted cells in order to quantify the role of ATP in CB dynamics (see figure 5.3). Typically, CBs show anomalous diffusion while moving within interchromatin nuclear compartment. Quite unexpectedly, upon ATP depletion CBs tend to diffuse faster and they are no longer associated with dense chromatin regions. In conclusion, the association between CB and chromatin is an active process needing ATP.

To summarize, these results illustrate the prominent role of microrheology in the characterization of nuclear organization and how this influences the motion of nuclear bodies which participate to the correct functioning of cellular processes.

5.2 A Model for the Microrheology of the Nucleus

As we have reviewed so far, microrheology has given essential information for the comprehension of nucleus. In particular, Tseng *et al.* [123] and Hameed *et al.* [131], separately, reported a consistent value of $250 - 290$nm value for nanoprobe-caging domains within nuclei of different types of cells and organisms (see section 5.1), suggesting a common origin for the domains. As pointed out by Valet and Rosa [150], this value is also surprisingly close to the nominal tube diameter, $d_T \approx 245$nm, predicted by the "topological" polymer model describing chromosome territories (see section 2.2.1).

Moreover, as we discussed in section 4.2, topological constraints by polymer fibers are likely to induce confinement of dispersed nanoprobes of diameter d if $d \gtrsim d_T$ [128, 129, 145]. Motivated by this phenomenon, Valet and Rosa [150] employed large-scale numerical simulations to study the effect of polymer entanglement on the diffusion of nanoprobes of diameter d, and therefore obtain quantitative information for the viscoelastic properties of the nucleoplasm approximated by a semi-dilute solution of chromatin fibers. Different nanoprobes were considered, with d ranging from 30nm (the fiber diameter) to 300nm (slightly above d_T).

Theoretical considerations and numerical simulations [12, 69, 71] suggest that the microscopic state of interphase chromosomes resemble the one of unconcatenated ring polymers in dense solutions. They had taken advantage of the recent multi-scale method [18] which combines efficiently Monte Carlo and Molecular Dynamics and construct a single, giant ring polymer which maps to a whole mammalian chromosome ($\approx 10^8$bps). It is important to remark that the construction is devised

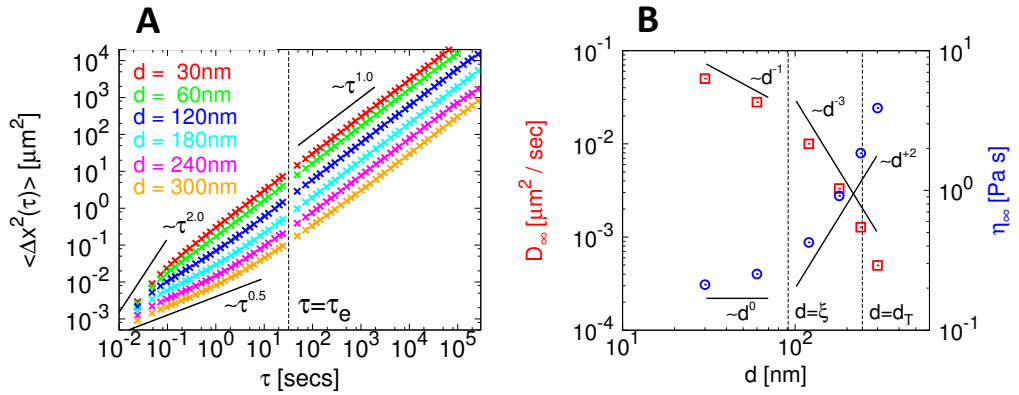

Figure 5.4: Viscoelasticity of model interphase chromosomes analysed by microrheology. (A) Time mean-square displacement, $\Delta x^2(\tau)$, of nanoprobes with varying diameter d. Vertical dashed lines mark the position of chromatin entanglement time $\tau_e \approx 32$ seconds [69]. (B) Asymptotic diffusion coefficient (□), $D_\infty \equiv D(\tau \to \infty)$, and particle viscosity (○), $\eta_\infty \equiv \eta(\tau \to \infty)$, as functions of nanoprobe diameter, d. Solid lines are for theoretical predictions in the non-entangled regime, see section 4.2. Polymer-mediated effects start at nanoprobe diameter $d \approx \xi \approx 90$nm. The largest nanoprobe diameter is of the order of the tube diameter, $d_T \approx 245$nm, of the chromatin solution. Reproduced from reference [150].

to model polymers *in bulk* [18] through the implementation of *periodic boundary conditions* and that *no explicit confinement* is imposed on the polymer.

The main results have been reported in figure 5.4: panel (A) contains the nanoprobe time mean-square displacement, $\langle \Delta x^2(\tau) \rangle$ while in panel (B) the asymptotic diffusion coefficient ($D_\infty \equiv D(\tau \to \infty)$) and viscosity ($\eta_\infty \equiv \eta(\tau \to \infty)$) *vs.* nanoprobe diameter are plotted.

The data demonstrate that for d smaller than the polymer correlation length $\xi \approx 90$nm and neglecting the short-time ballistic regime ($\langle \Delta x^2(\tau) \rangle \sim \tau^2$), nanoprobe motion is not or only weakly coupled to chromosome dynamics, implying $\langle \Delta x^2(\tau) \rangle \equiv 6 D_\infty \tau$ with "standard" behaviors $D_\infty \sim d^{-1}$ and $\eta_\infty \sim d^0$. Viceversa, for $d > \xi$ coupling to chromosome dynamics induces nanoprobe subdiffusion ($\langle \Delta x^2(\tau) \rangle \sim \tau^{1/2}$) at small τ and consequent "anomalous" behaviors $D_\infty \sim d^{-3}$ and $\eta_\infty \sim d^2$, in agreement with the theoretical results summarized in section 4.2.

The analysis focuses also on some peculiarities which are reported in figure 5.5: the distribution functions for D_∞ (see panels A and B) and, even more interesting, the distribution functions for particle displacements $\Delta x(\tau) \equiv |x(\tau' + \tau) - x(\tau')|$ at different lag-times τ (see panels C-D). In general, D_∞ and $\Delta x(\tau)$ appear Gaussian-distributed (black lines). With one notable exception: for $\tau \ll \tau_e$ and large nanoprobes, $P(\Delta x(\tau))$ appears significantly different from the Gaussian function. This follows from the presence of surrounding polymers exerting constraints and inducing spatial correlations [150] on nanoprobe displacement.

Finally, by using the fundamental relation of microrheology connecting the complex shear modulus to nanoprobe mean-square displacement (equation. 4.1), theo-

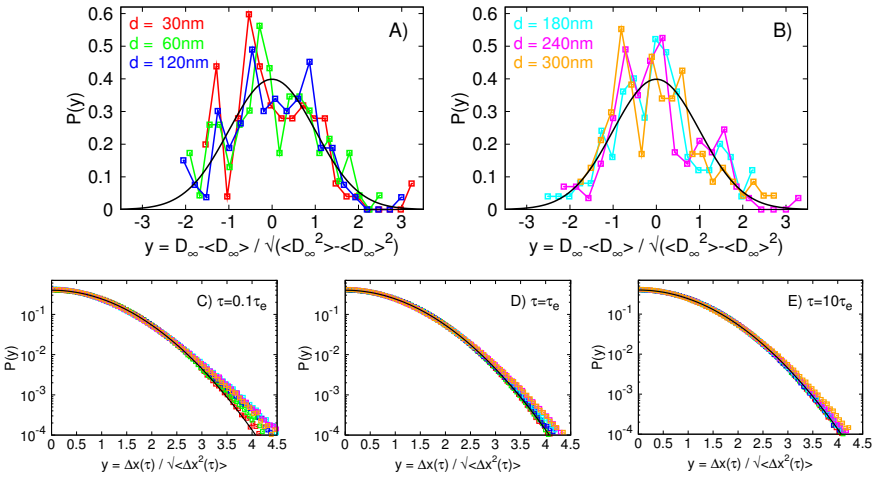

Figure 5.5: (A,B) Distribution functions for the asymptotic diffusion coefficients, D_∞. The shape of the distributions compares well to the Gaussian function (black line). (C,D,E) Distribution functions for one-dimensional nanoprobe displacements, $\Delta x(\tau) \equiv |x(t+\tau) - x(t)|$, at different lag-times τ. The x-axis have been rescaled according to the corresponding standard deviations $\sqrt{\langle \Delta x^2(\tau) \rangle}$ and the curves compared to the normal form of the Gaussian function describing ordinary diffusion [156]. At $\tau \ll \tau_e$, $P(\Delta x(\tau))$ shifts from Gaussian to non-Gaussian behavior at increasing nanoprobe diameters. Universal Gaussian behavior is recovered at all d's at $\tau \gg \tau_e$. Color code is as in figure 5.4.

retical predictions for the storage and loss moduli at frequency ω can be extracted and then compared to available experimental results, see Table 5.1. In spite of its simplicity, the polymer model is in reasonable agreement with experiments. The main difference is that experiments predict nuclei with $\hat{G}' > \hat{G}''$ (*i.e.* more solid- than liquid-like), while the polymer model predicts the opposite. Since nanoprobes with diameters larger than d_T should experience a more solid-like behavior, this difference can be ascribed to the size of the simulated nanoprobes which is just about d_T. It would be interesting to test then if larger nanoprobes would go more towards the observed experimental behavior.

At the same time, other factors which have not been taken into account because of the initial intention to keep the polymer model as simple as possible could contribute as well to explain deviations from experiments.

Obviously, due to the complexity of the genome and the simplicity of the model, it is no surprise that there is still much work ahead which remains to be done in order to arrive to a satisfactory picture of genome organization in terms of polymer physics. An evident inconsistency between the outcome of microrheology experiments and the results of polymer model developed by Valet and Rosa is in the latter showing no sign of a plateau in the time MSD or the storage modulus $G'(\omega)$ in spite of the very similar sizes of nanoprobes used. It can be clearly observed comparing figure 4.1 (from reference [123]) to figure 5.4,

			0.1 Hz		1 Hz		10 Hz	
d [nm]	D_∞ [$\times 10^{-3}\mu\mathrm{m}^2 \cdot \mathrm{s}^{-1}$]	η_∞ [Pa · s]	$\hat{G}'$ [Pa]	$\hat{G}''$ [Pa]	$\hat{G}'$ [Pa]	$\hat{G}''$ [Pa]	$\hat{G}'$ [Pa]	$\hat{G}''$ [Pa]
30	50.0	0.21	–	0.0214	–	0.2045	–	2.0651
60	28.0	0.25	0.0004	0.0238	0.0079	0.2532	–	2.2061
120	10.0	0.42	–	0.0423	0.0712	0.3948	0.7009	2.3778
180	3.3	0.92	0.0086	0.0882	0.2260	0.6865	1.6126	2.8336
240	1.3	1.81	0.0349	0.1469	0.4959	1.0163	2.6690	3.5608
300	0.5	3.86	0.0747	0.2972	0.8674	1.4476	3.7901	4.5105

Microrheology of the nucleus: theoretical predictions from reference [150]

d [nm]	Organism	Frequency [Hz]	$\hat{G}'$ [Pa]	$\hat{G}''$ [Pa]
100	Swiss 3T3 fibroblasts (mouse) [123]	$1-10$	≈ 10	$\approx 3-10$
1000	HeLa cells (human) [131]	1	≈ 0.1	≈ 0.05

Microrheology of the nucleus: experiments

Table 5.1: Microrheology of the nucleus: theoretical modeling (top) *vs.* experiments (bottom). Asymptotic diffusion coefficients (D_∞), viscosities (η_∞) and selected values for storage ($\hat{G}'(\omega)$) and loss ($\hat{G}''(\omega)$) moduli. The symbol "–" means no data are available.

Indeed, this model describes simply the diffusion of the chromatin fibers within the interior of the nucleus of the cell. The interactions between chromatin fibers and the various structures within the nucleus also cover an important role and their inclusion could make the model more coherent with experimental data.. This point will be extensively discussed in details in the following sections.

5.3 Biophysical Motivation: the Nucleoskeleton

In next section we will introduce a simple extension of the polymer model by Valet and Rosa for chromatin fibers in interphase which can overtake some limitations of the model which has been described in the last section. We took inspiration from the interactions observed between the chromatin fibers within the interior of the nucleus of the cell with the nucleoskeleton.

The so-called "nucleoskeleton" [157, 158] has been variously described as an ensemble of extensive, "extra-chromatin" structures percolating through the nucleus and constraining the position of chromatin in space. Although a more rigorous definition of the nucleoskeleton is still elusive (to some extent, even its existence has been questioned several times [157, 158] due to the often harsh conditions used in experiments aiming at detecting its presence) a certain number of structures with an active role in it have been identified so far. In particular, "C"-techniques [13, 159] have detected systematic interactions between chromatin fibers and the nuclear envelope at complex protein networks called nuclear lamina [160, 161] (see figure 5.6, panel A). At the same time, high-resolution confocal imaging of nascent RNA transcripts are compatible with a model where chromatin is locally bound to immobile structures called transcription factories [162] (see figure 5.6, panel B). Then, by a combina-

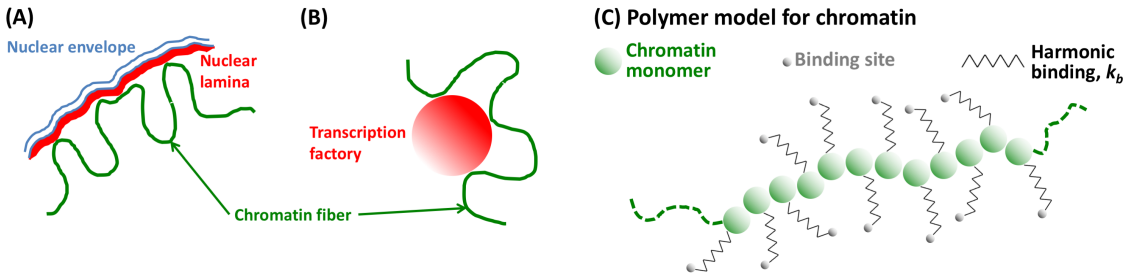

Figure 5.6: (A, B) Schematic picture illustrating two common situations where chromatin fibers have been reported to bound to extra-chromatin sub-nuclear structures taking part in the "nucleoskeleton": respectively, the internal wall of the nuclear envelope through the nuclear lamina [160, 161, 164] and the so-called transcription factories within which the transcription machinery is believed to be allocated [162]. (C) Illustration of the bead-spring polymer model introduced in this work with the purpose of understanding how such mechanical constraints may turn to affect the internal chromosome structure: big green circles are for chromatin monomer particles, small grey circles are for fixed attachment points, the wavy lines are for the harmonic potential modeling the strength of the interaction.

tion of molecular and imaging approaches a significant amount of nuclear RNA is reported to bind to chromatin-scaffold proteins. These "hybrid" protein/RNA structures form a nuclear mesh which plays a crucial role in regulation of chromatin structure during interphase [163].

Taken together, these results point towards a picture where chromatin is far from being free, its motion being restricted by local interactions to specific sub-nuclear structures. Importantly, based on increasing evidence showing that any deviation from this architecture produces serious if not lethal consequences on the whole organism, these interactions underpin fundamental biological roles: as an example, laminopathies are a particular class of genetic diseases displaying the disruption of contacts between certain chromatin loci and the nuclear lamina [165] which turn to affect the normal course of chromosomal conformations.

As we discussed in Chapter 2, the intrinsic local folding and mechanical properties of the chromatin fiber are known [160, 166, 167] to influence genome function: arguably, these properties are not only the direct consequence of the physico-chemical properties of the fiber itself but they also follow from the detailed pattern of interactions between the chromatin and the sub-nuclear structures which constitute the nucleoskeleton. How all this is mutually connected and, most importantly, what are the relative biological implications is not clear yet: motivated by that, here in the following section we will present a theoretical framework aiming at the understanding of how interactions of tunable strength turn to affect the local organization and dynamics of chromatin fibers. More specifically, we will focus on the discussion of the physical consequences of restricting chromatin motion without altering significantly its large-scale folding.

In the model described in section 5.2, the authors, Valet and Rosa, have made

the hypotesis that nanoprobes are temporarily slowed down by topological constraints (or, entanglements [1, 2]) arising from the mutual structural interplay of the polymer-like chromatin fibers filling [42] the nucleus. This hypotesis seems partially in agreement with experimental works where, in spite of the different cell types and nanoprobe sizes effectively employed, nanoprobe motion appears to be invariably "caged" at a characteristic length-scale of about $250 - 290$nm [123, 131, 151], a peculiarity which is not present in the model. In the next section, we will move from this premise and consider the more general situation where chromatin fibers move under the constraint of being subject to (more or less) loose spatial constraints: the purpose is to provide a physically-motivated picture aiming at elucidating the role of such spatial constraints on nanoprobe diffusion within the nucleus and, hence, the overall chromatin viscoelastic properties.

5.4 The Model

The numerical model for the chromatin fibers and the nanoprobes employed here has been adapted with a few minimal variations from the computational set-up described in detail in previous publications, see [18, 68, 69, 74, 150].

We have already described how chromatin-chromatin interactions are modeled according to the generalized Kremer-Grest-like [168] bead-spring model for semi-dilute polymer solutions introduced by Rosa and Everaers in section 2.2.1 (see Refs. [18, 69, 74] for the original work and reference [68] for a generalized implementation of the model). The model takes into account linear connectivity, stiffness and local topology conservation of the chromatin fiber (for further details on the model see appendix A.4). In the model, the energy scale is set by the thermal energy $\epsilon = \kappa_B T$ with $T = 300$ K, the fundamental length-scale by the fiber diameter $\sigma = 30$ nm $= 3000$ basepairs (bps) and the chromatin stiffness is given by the fiber Kuhn length [2] $\ell_K = 300$ nm. The overall density of the system is $= 0.012$ bp/nm^3. As in reference [150], our system is made of a single model chromosome made of $N = 39154$ chromatin monomers of diameter σ, which corresponds to a total contour length of $\approx 10^8$ bps, *i.e.* the size of a mammalian chromosome [42].

The spatial constraints arising from dynamic interactions between the chromatin fiber and the nuclear bodies forming the "nucleoskeleton" are phenomenologically taken into account simply by forcing the dynamic motion of the i-th bead ($i = 1, ..., N$) of spatial coordinate $\vec{r}_i$ to remain bound to an equilibrium position $\vec{r}_i^{eq}$ whose coordinates are *fixed* in space, see figure. 5.6, panel C. This is implemented by the following harmonic potential:

$$U_b = \frac{k_b}{2} (\vec{r}_i - \vec{r}_i^{eq})^2 \ . \tag{5.1}$$

This choice has been made in order to keep our working hypotheses as simple as possible since the nature of the "nucleoskeleton" remains still under debate. Notice that we have chosen the same coupling constant k_b *for all monomers*. We have considered the three different values of the elastic binding constant $k_b \sigma^2/\epsilon =$

$0.2, 2.0, 20.0$ or, in real units, $k_b = 8.9 \cdot 10^{-4}, 8.9 \cdot 10^{-3}, 8.9 \cdot 10^{-2}$ pN/nm. Generalizations to situations where each monomer is characterized by its own k_b are straightforward: qualitatively, we expect to obtain results in line with those reported here. For reference, we have compared the obtained results to those obtained in the original model, reported in refence [150] and corresponding to the unconstrained case of $k_b\,\sigma^2/\epsilon = 0$.

Then, the viscoelastic properties of the different chromatin systems have been explored by monitoring the diffusion of $N_{\rm np} = 100$ non-sticky, athermal (*i.e.*, purely repulsive) nanoprobe particles with increasing diameters $d/\sigma = 1, 2, 4, 6, 8, 10$ corresponding to $30, 60, 120, 180, 240, 300$ nm respectively. We stress that even the largest nanoprobes remain significantly smaller than the estimated linear size ($2-3$ μm) of a single territory, thus the adopted protocol is compatible with our goal of modeling the "bulk" of the nucleus.

5.4.1 Molecular Dynamics Simulations

The static and kinetic properties of chains and nanoprobes are studied using fixed-volume and constant-temperature Molecular Dynamics (MD) simulations with implicit solvent and periodic boundary conditions. MD simulations are performed using the LAMMPS package [169]. The equations of motion are integrated using a velocity Verlet algorithm, in which all beads are weakly coupled to a Langevin heat bath with a local damping constant $\Gamma = 0.5\tau_{\rm MD}^{-1}$ where $\tau_{\rm MD} = \sigma(m/\epsilon)^{1/2}$ is the Lennard-Jones time and $m = 1$ is the conventional mass unit for monomer and colloidal probes. After mapping to real time units $\tau_{\rm MD} \approx 0.02$ seconds, see reference [69] for details. The integration time step is set to $\Delta t = 0.012\,\tau_{\rm MD}$ and the length of each MD run is equal to $2.4 \times 10^7 \tau_{MD}$ or ≈ 6 days in real time.

The initial configuration has been prepared coherently with the procedure reported in refence [150], so that we can make an accurate comparison. Then, the equilibrium positions $\vec{r}_i^{\,eq}\,(i = 1, ..., N)$ of equation (5.1) correspond to the initial positions of the monomers at the end of the numerical algorithm leading to the construction of the ring: this guarantees that during the run the whole chromosome always fluctuates around its "equilibrium" position. We remark that as the process of constructing the ring is *stochastic* and *unbiased*, the set of positions $\vec{r}_i^{\,eq}$ appear to be distributed uniformly inside the simulation box.

Finally, we complete the system by adding $N_{\rm np} = 100$ nanoprobes. This was achieved by inserting them at random positions within the simulation box, and using a gentle insertion procedure [150] which guarantees that the system is only minimally perturbed. The details of the numerical implementation of the chromatin-nanoprobe and nanoprobe-nanoprobe interactions are the same as in reference [150].

5.4.2 Results and Discussion

Chromosome folding during interphase is surprisingly well described in terms of a polymer-like solution of chromatin fibers in semi-dilute conditions [39, 68, 69, 73, 74,

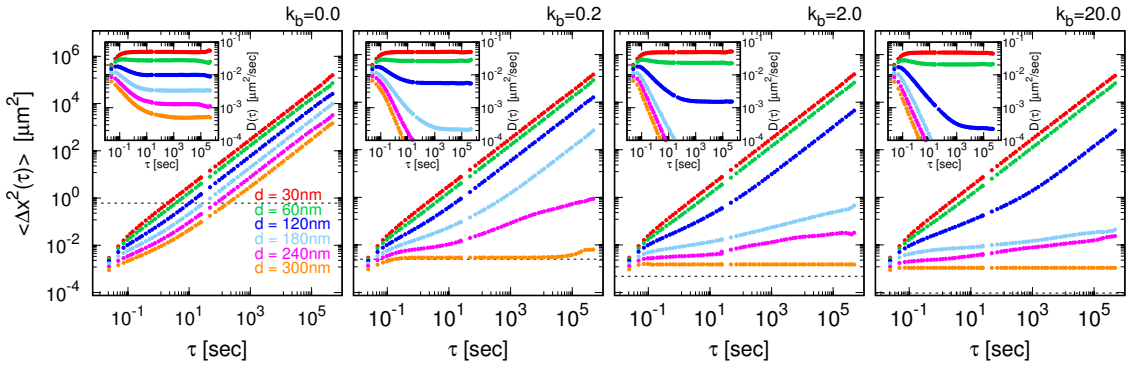

Figure 5.7: Lag-time dependence of nanoprobe mean-square displacement $\langle \Delta x^2(\tau) \rangle$ (see equation 5.5) for different nanoprobe diameters (d) and spring strengths (k_b, in units of $\epsilon/\sigma^2 = 4.4 \cdot 10^{-3}$pN/nm) modeling spatial constraints on the chromatin fiber (see equation 5.1). Horizontal lines correspond to the stationary mean-square spatial fluctuations of chromatin monomers. (Insets) Corresponding time-dependent diffusion coefficient, $D(\tau) \equiv \langle \Delta x^2(\tau) \rangle / 6\tau$.

170, 171, 172]. Here, we adopt this view with the addiction of permanently restraining the motion to chromatin fibers through tunable harmonic interactions to fixed nuclear locations, see equation 5.1: these interactions have never been considered before and are meant to describe (in a simplified way) the action of extra-chromatin constraints imposed by the nucleoskeleton (see the Introduction). Thus, the motion of single chromatin fibers is not only restricted by the presence of the surrounding chromatin chains but, obviously, it is hindered further due to the presence of these "external" interactions.

The Mean-Square Displacement

To characterize nanoprobe motion, we consider the time mean-square displacement for the np-th nanoprobe defined as:

$$\Delta x^2_{\rm np}(T;\tau) \equiv \frac{1}{T-\tau} \int_0^{T-\tau} \left(\vec{x}_{\rm np}(t+\tau) - \vec{x}_{\rm np}(t) \right)^2 dt \tag{5.2}$$

where τ is the lag-time and T is the total measurement or observation time. Separate time and ensemble averages of expression are, respectively, defined as:

$$\langle \Delta x^2_{\rm np}(\tau) \rangle \equiv \lim_{T\to\infty} \Delta x^2_{\rm np}(T;\tau)\,, \tag{5.3}$$

$$\langle \Delta x^2(T;\tau) \rangle \equiv \frac{1}{N_{\rm np}} \sum_{\rm np=1}^{N_{\rm np}} \Delta x^2_{\rm np}(T;\tau)\,. \tag{5.4}$$

Accordingly, simultaneous time- and ensemble-average is given by:

$$\langle \Delta x^2(\tau) \rangle \equiv \lim_{T\to\infty} \frac{1}{N_{\rm np}} \sum_{\rm np=1}^{N_{\rm np}} \Delta x^2_{\rm np}(T;\tau)\,. \tag{5.5}$$

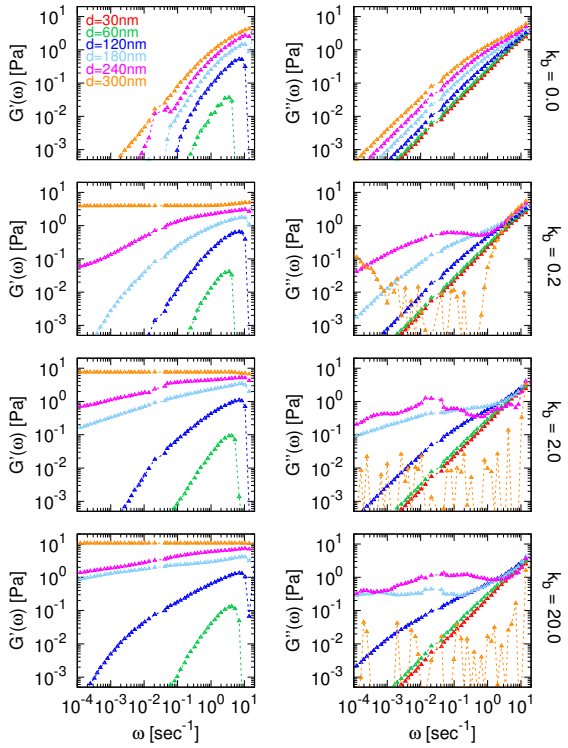

Figure 5.8: Storage ($\hat{G}'(\omega)$) and loss ($\hat{G}''(\omega)$) moduli (in Pascal ([Pa]) units) as a function of frequency ω computed according to the numerical method by Mason, see Appendix A.3.2. A simple smoothing procedure has been carried on to reduce the effect of the noise of the data. Color code is the same as in figure 5.7.

Obviously, in equations (5.3) and (5.5) it is implicitly assumed that the trajectories are long enough such that the "$T \to \infty$"-limit is a reasonable approximation.

The displacements for the different set-up's considered in this work are showed in figure 5.7, while the insets display the corresponding time-dependent diffusion coefficient $D(\tau) \equiv \langle \Delta x^2(\tau) \rangle / 6\tau$. The motion of the two smallest nanoprobes considered here ($d = 30$nm and $d = 60$nm) is mostly reflecting the interaction with the solvent [150], consequently any restriction on chromatin dynamics does have limited influence on those. Conversely, larger nanoprobes appear remarkably slower if not completely caged (see the case of the largest nanoprobes with $d = 300$nm). The transition to nanoprobe "slowdown" induced by restricting or blocking chromatin activity appears on the same length-scale (≈ 100nm) of chromatin stiffness [69] or the chromatin correlation length [41], *i.e.* where polymer effects as opposed to solvent effects start [150] dominating nanoprobe motion. Nonetheless, nanoprobes of intermediate diameters are still able to diffuse in spite of the fact that the mean-square spatial fluctuations ($\langle (\vec{r}_i - \langle \vec{r}_i \rangle)^2 \rangle$) of chromatin monomers are sensibly suppressed (see horizontal lines in the different panels of figure 5.7).

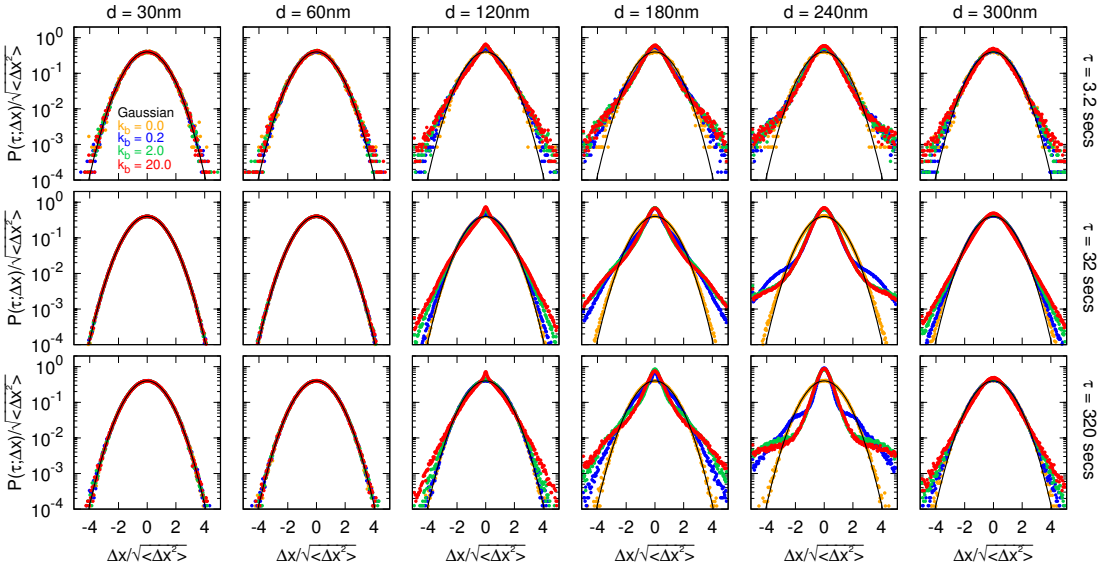

Figure 5.9: Probability distribution function of one-dimensional nanoprobes displacements, $P(\tau;\Delta x)$ (equation. 5.6) at the three representative lag-times $\tau = 3.2, 32, 320$ seconds and for different nanoprobe diameters (d). Different colors correspond to the different spring strengths (k_b, in units of $\epsilon/\sigma^2 = 4.4 \cdot 10^{-3}$pN/nm) modeling spatial constraints on the chromatin fiber (see equation. 5.1). Black solid lines correspond to the Gaussian distribution function typical of normally-diffusive processes.

Shear Modulus

By employing the method developed by Mason in reference [173] (for technical details see Appendix A.3.2), we have computed the storage ($\hat{G}'(\omega)$) and loss ($\hat{G}''(\omega)$) moduli in the frequency domain, see figure 5.8. Obviously, the behavior of the two functions reflects the corresponding $\langle \Delta x^2(\tau) \rangle$: with the exception of the case where chromatin is unconstrained ($k_b = 0$) or for small nanoprobes ($d \leq 60$nm), the elastic component of chromatin invariably dominates over its viscous counterpart (*i.e.*, $\hat{G}'(\omega) > \hat{G}''(\omega)$) and the nucleus behavior is akin to behave solid-like.

Correlation Functions

A more insightful view into nanoprobe motion is given by the probability distribution function of *one-dimensional* displacements Δx at the given lag-time τ, which corresponds to the self-part of so-called van-Hove function [174]. This is defined as:

$$P(\tau;\Delta x) \equiv \langle (\Delta x - (x(t+\tau) - x(t))) \rangle . \tag{5.6}$$

Inspired by previous work [146] and also to provide an immediate intuition on its behavior in time, we have calculated $P(\tau;\Delta x)$ for the three representative cases of $\tau = 3.2, 32, 320$ seconds.

In particular, the different cases considered in this work, in comparison to the Gaussian distribution (black solid lines) have been plotted in figure 5.9. For small

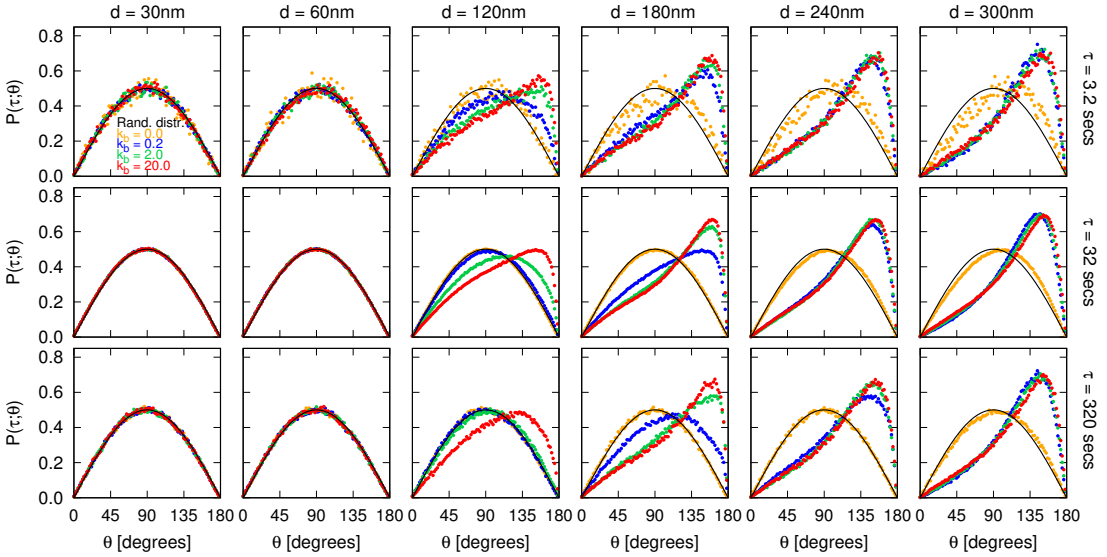

Figure 5.10: Probability distribution functions $P(\tau;\theta)$ for the angle θ between pairs of oriented, τ-lagged nanoprobe spatial displacements taken consecutively along the trajectory. Color code and notation are as in figure 5.9. Black solid lines are for the curve $P(\tau;\theta) = \sin\theta/2$ for randomly orientated vectors.

nanoprobes with $d \leq 60$nm at any k_b and for larger nanoprobes at $k_b = 0$, we see that $P(\tau;\Delta x)$ is Gaussian at all times. Conversely, blocking chromatin activity deforms the distributions for thicker nanoprobes ($d > 60$nm) by inducing *heavy-tail* correlations.

The physical origin of these correlations stems from nanoprobe being trapped within the polymer matrix. A simple way [146, 150] to show it is by considering the probability distribution functions for the angle θ between oriented nanoprobe spatial displacements separated by lag-time τ, which is defined as:

$$P(\tau;\theta) \equiv \left\langle \theta - \cos^{-1}\left(\frac{\vec{x}(t+2\tau)-\vec{x}(t+\tau)}{||\vec{x}(t+2\tau)-\vec{x}(t+\tau)||} \cdot \frac{\vec{x}(t+\tau)-\vec{x}(t)}{||\vec{x}(t+\tau)-\vec{x}(t)||} \right) \right\rangle . \qquad (5.7)$$

Finnally, figure 5.10 summarizes our results for $P(\tau;\theta)$ for the different set-up's and the same lag-times used in figure 5.9 in comparison to the "random" distribution $P(\theta) = \sin\theta/2$ (black solid lines). As expected, while non-trapped nanoprobes display randomly-correlated displacements semi- and completely trapped nanoprobes show pronounced correlations. Clearly these correlations mirror the behaviors of corresponding $P(\tau;\Delta x)$'s (see figure 5.9), in particular they emerge whenever nanoprobe size is larger than chromatin stiffness. In this respect, for moderate chromatin anchoring ($k_b = 0.2\,\epsilon/\sigma^2$) nanoprobes of intermediate sizes ($d = 120$nm and $d = 180$nm) display a (slow) drift to uncorrelated motion, although much longer trajectories seem to be required in order to reach the asymptotic regime.

The presence of heavy-tail correlations in the van-Hove function is in general associated to heterogeneous single-particle dynamics in glassy and jammed systems [146, 174, 175]. To check for spatial heterogeneity, we consider the curves

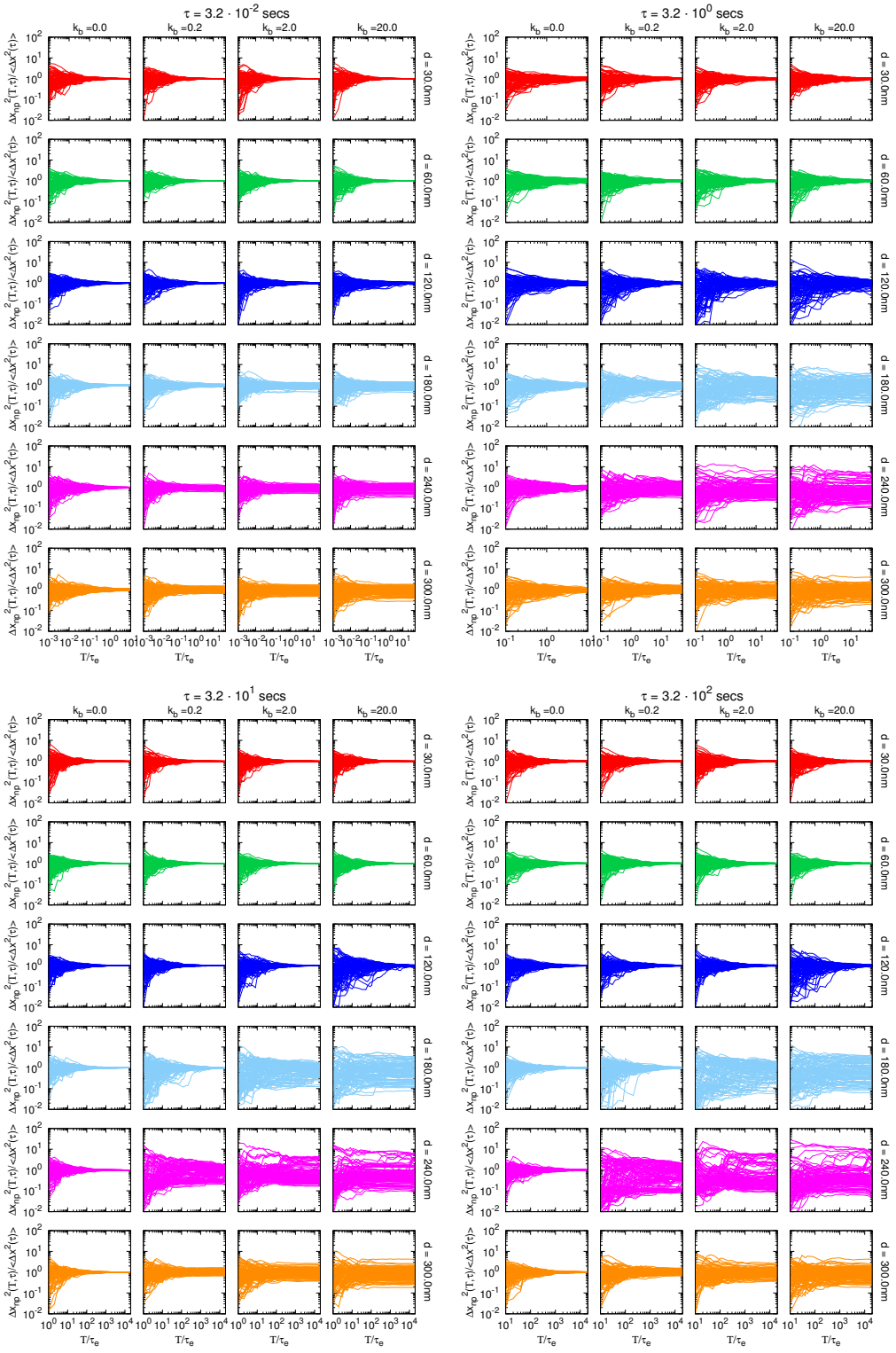

Figure 5.11: Spatial heterogeneity of mean-square displacements $\Delta x^2_{\mathrm{np}}(T;\tau)/\langle \Delta x^2(\tau)\rangle$ *vs.* the measurement time T at representative lag-times τ, for the different nanoprobe diameters (d) and spring strengths (k_b) modeling spatial constraints on the chromatin fiber (see equation (5.1)).

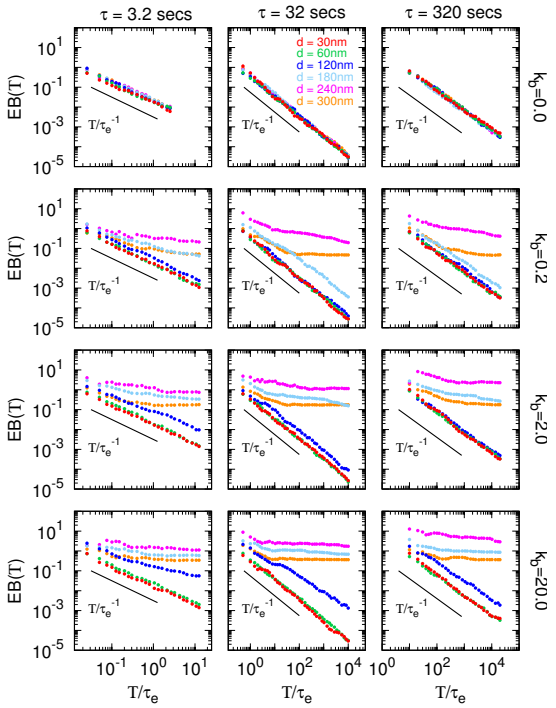

Figure 5.12: Ergodicity breaking parameter, EB(T) (see Eq. (5.8)), *vs.* the measurement time T at representative lag-times τ, for the different nanoprobe diameters (d) and spring strengths (k_b) modeling spatial constraints on the chromatin fiber (see Eq. (5.1)). Color code is as in figure 5.7.

$\Delta x^2_{\rm np}(T;\tau)/\langle\Delta x^2(\tau)\rangle$ as functions of the measurement time T for the entire set of $N_{\rm np}$ nanoprobes. For ergodic systems, at any chosen lag-time τ we expect that the different curves should all narrow towards ≈ 1 in the limit of large measurement time T, while heterogeneity arising from nanoprobe trapping should manifest in the spread of the different curves around the mean value. Figure 5.11 shows that this is indeed the case, in particular we report consistent spread between the different curves which remain stably separated whenever chromatin motion is hampered.

Finally, to better quantify regression to equilibrium and ergodicity breaking, we introduce the so-called ergodicity breaking parameter [146, 175, 176]:

$$\mathrm{EB}(T;\tau) \equiv \frac{\left\langle \left(\Delta x^2(T;\tau)\right)^2 \right\rangle}{\left\langle \Delta x^2(T;\tau)\right\rangle^2} - 1\,. \tag{5.8}$$

For standard diffusive processes, $EB(T;\tau)$ decays as $\sim T^{-1}$, whereas in nonergodic systems $EB(T;\tau) \sim T^0$. Figure 5.12 shows that, in general, this is indeed the case: in particular, because of the caging induced by restrained chromatin motion nanoprobes with diameters larger than the chromatin Kuhn length display dynamic behavior consistent with theoretical expectations.

5.5 Conclusions

In this Chapter, we have described a simple polymeric model to model the viscoelastic properties of nuclei of eukaryotic cells. In particular, we reported the main results obtained carrying out a systematic numerical study. We have reconsidered the parameter-free polymer model outlined in 5.2 [68, 69, 74] which describes the crumpled structure of chromatin fibers inside a chromosome territory. The main difference is that the motion of each chromatin filament is constrained by means of two different mechanisms: the nearby fibers *and* the additional contribution of external, restraining forces. In particular, this last "ingredient" is motivated by the experimentally demonstrated situations where chromatin motion is restricted due to its binding to the nucleoskeleton.

In the framework of microrheology, we showed that chromatin stiffness (or Kuhn length, ℓ_K) sets the length-scale above which nanoprobe motion becomes a reliable sensor for detecting spatial constraints on the chromatin fiber. In particular, due to restrictions on chromatin behavior, motion of nanoprobes of diameter larger than ℓ_K becomes manifestly obstructed (figures 5.7 and 5.8). This phenomenon brings with it two important consequences:

1. distribution functions of spatial displacements show heavy-tail behavior (see figure 5.9) and non-random directional correlations (see figure 5.10);

2. nanoprobe motion is no longer ergodic and manifests some distinctive features which typically arise in glassy systems, such as heterogeneous behavior (see figure 5.11) and ergodicity breaking (see figure 5.12).

We stress that these results depend uniquely on the particular microscopic state associated to the bulk of interphase chromosomes and on the presence of constraints on the fiber, otherwise they should be independent on the fine details of the chromosome model: in fact, adopting a model for chromatin of finer resolution (10nm-fiber [177] instead of 30nm-fiber as chosen in this work) has poor impact on the average properties of the simulated chromosome conformations [68]. In the biophysical context, experimental works measuring the viscoelastic properties of the nucleus are in very limited number, owing to the fact that introducing nanoprobes inside the nucleus is an invasive procedure which, not infrequently, leads to cell death [131]. Yet, there have been reported cases [122, 131] of successful insertion of passive nanoprobes in the intranuclear medium. Interestingly, these studies suggest that the nucleus behaves like a viscoelastic medium with $\hat{G}'(\omega)$ in the range of a few pascal and significantly larger than $\hat{G}''(\omega)$ for frequencies up to ≈ 10 sec^{-1}. The results showed in this Chapter demonstrate that a polymer model of chromatin fibers which takes into account the presence of extra bonds to an immobile nuclear matrix is able to capture remarkably well these experimental observations. These observations suggest then, that the presence of a certain amount of bonds to an extra-chromatin matrix may help maintaining the three-dimensional folding of chromosomes *in-vivo*.

Chapter 6

Microrheology in out-of-equilibrium polymer melts

The content of this Chapter[1] focuses on the application of microrheology to investigate the viscoelastic properties of out-of-equilibrium polymeric solutions composed of a mixture of polymers coupled to different Langevin thermostats, a well-known case of study in the context of Active Matter. In particular, we will explore the effects that polymers with different topologies produce on the diffusion of nanoprobes: to fix the ideas, based on the work by Nahali and Rosa [146] and the theoretical analysis reported in section 4.2, we will concentrate on melts of linear vs. ring chains.

The Chapter is organized as follows: in section 6.1 we will provide a short introduction to the concept of *Active Matter* and the out-of-equilibrium dynamics which emerges in mixtures of active and passive particles [178, 179, 180, 181]. Then, in section 6.3 we will review some results for models describing the dynamics of entangled, active polymers and related applications the field of biological systems [182, 183, 184].

Finally, in section 6.4, we present the preliminary analysis of our results.

6.1 An introduction to Active Matter

Active Matter is a rapidly growing field in Theoretical Physics and has found particularly interesting applications in the fields of collective behaviours the out-of-equilibrium statistical physics of biological systems [185, 186, 187]. In general, the constituents of active systems are self-driven units which consume or dissipate energy to move or to perform mechanical work. In living matter, the source of energy is, typically, the hydrolysis of nucleoside tri-phosphate (NTP, such as ATP or GTP) molecule into its di-phosphate form.

The interaction of active particles among themselves and with the environment that surrounds them affect their dynamics and originate collective motions. Active

[1] The material described in the present Chapter is based on the preliminary results of an ongoing project.

systems exhibit a range of different and intriguing phenomena, including pattern formation, out-of-equilibrium order-disorder transitions, emergent structures due to collective behavior, peculiar probability distributions or unexpected rheological properties. The complexity of such phenomena represents an obstacle to develop a theoretical description of generic active systems since thermal equilibrium concepts could be ill defined, and, in a large number of cases, requires the development of ad-hoc theories.

From the theoretical point of view, two classes of models have been considered within the context of active matter:

- the vectorial class, particles dynamics is described by a direction that randomizes through various mechanisms (examples are the Viscsek model [188], Active Brownian particles [189] and Run and Thumble [190]);
- the class regarding models with scalar activity: active particles are associated to enhanced thermal-like fluctuations moving within passive particles [178, 179, 180].

Here, we will focus on the second category of models, in particular we discuss models which are constituted by a mixture of active/passive particles and polymers. This kind of out-of-equilibrium models has been studied both theoretically, by Grosberg and Joanny in the dilute regime [178] and with a field theory approach by Wittkowski *et al.*[180], and numerically by Weber *et al.*[179]

6.2 Mixtures of Particles with Different Diffusivities

As simplest case, we consider a general model consisting of a mixture of two particle types which differs for their diffusion constants, interacting by a pure repulsive potential. By definition, a homogeneous system of gas-like particles at equilibrium is characterized by the fact that the particles have all the same temperature. In contrast, according to this model, active (or "hot") particles are associated to a fictitious thermostat with temperature T_{hot} and diffuse within passive (or "cold") particles associated to a fictitious thermostat reference temperature T_{cold}. This system, even in the dilute regime, is out-of-equilibrium: a local current of energy arises from the hotter to the colder reservoir through the local interactions between particles, violating the detailed balance. This flow vanishes only when the two temperatures are equal and the system falls in equilibrium again. As pointed out by Weber *et al.* [179], the difference in the diffusivity leads the system to a dynamical phase separation: the mixture of particles, when the difference in the diffusion constants is large enough, spontaneously segregates from a random initial condition into a solid-like phase composed by the particles with the lower diffusion constant (cold particles) surrounded by a gas-like phase of mainly hot particles.

In details, Weber *et al.* considered a 2-dimensional model with only an harmonic repulsive potential which, in principle, allows overlaps between particles and

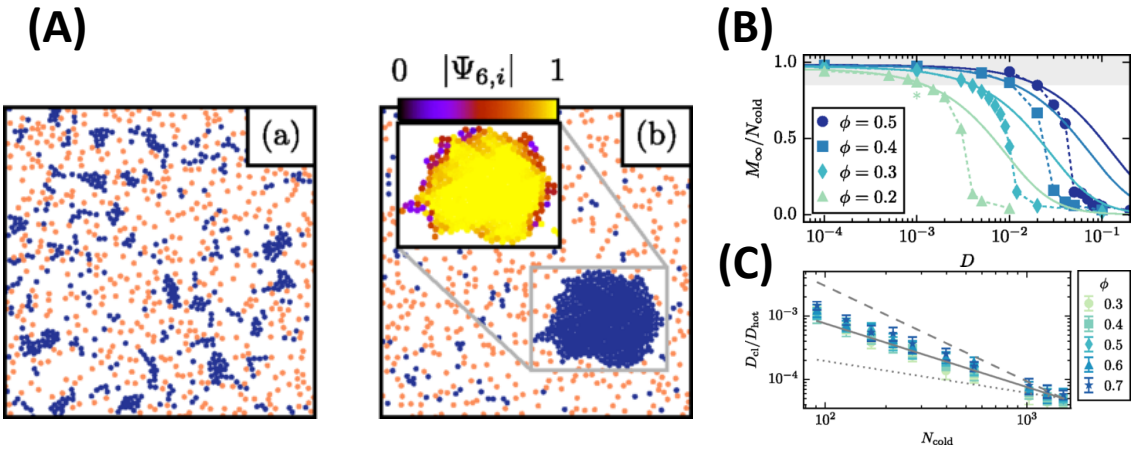

Figure 6.1: (A) Snapshots of particle configurations in a binary mixture of 500 hot particles (orange, light gray) and 500 cold particles (blue, dark gray) at early times (a) and when the cluster dynamics reaches dynamical stability (b). The diffusion constant ratio is $D = D_{cold}/D_{hot} = 10^{-3}$. (B) Fraction of cold particles belonging to the largest cluster of the system, M_∞/N_{cold}, which have been averaged after saturation, as a function of the diffusion constant ratio D. The graph is relative to a system with $N_{cold} = N_{hot} = 300$ particles. (C) Diffusion constant D_{cl} for a saturated cluster of cold particles in units of D_{hot} as a function of the number of cold particles N_{cold}. The graph reports the results for various packing fractions ϕ indicated Moreover, three straight lines guide to reading the power law scalings $D_{cl}/D_{hot} \sim N_{cold}^{-k}$: $k = 1.5$ (dashed), $k = 1.0$ (solid), $k = 0.5$ (dotted). Reproduced from reference [179]

enhances the depletion effect of cold particles. Indeed, the particle dynamics is determined by its intrinsic diffusion and by particle collisions and lead to an effective diffusivity and to a dynamical phase separation (see figure 6.1, panel A). However, the phase separation occurs only under a critical value of the ratio between the diffusion constants $D = D_{cold}/D_{hot}$: even for dilute systems with low density, the observed critical ratio implies differences of temperature of various orders of magnitude which is almost impossible to be realized experimentally. For the right value of D, from a mixed and random initial configuration, cold particles build up small clusters, which grow and/or merge until almost all cold particles converge in the largest cluster (see figure 6.1, panel B). In any case, the space of parameters for this model is very complex, indeed this behavior obviously depends on several parameters, like the shape of interaction, the diffusivities or the packing fraction ϕ.

In the work by Weber *et al.*, the saturation of the size of the cluster is an artifact arising from the finite size of computer simulations: for larger systems, multiple clusters of cold particles would keep growing and then merge in bigger clusters or coalesce during their collective diffusion. It is interesting to underline that the diffusion constant of saturated clusters results to be inversely proportional to the number of cold particles N_{cold} which constitute it (see figure 6.1, panel C).

6.3 Activity-Based Segregation in Polymers Mixtures

There are many examples of systems at the interface between polymer physics and active matter and various models and approaches have been developed to analyse them [187, 191]. In particular, in this section we focus on the general properties of polymeric systems composed of a mixture of polymers with different thermal activities [182, 183, 184, 192, 193]. Indeed, while the critical ratio of diffusion constants $D = D_{cold}/D_{hot}$ is necessarily low for simple particles to observe a clear phase separation (as seen in figure 6.1), in the case of polymers, the ordered phase may be experimentally realized, as the critical ratio decreases with their length [192].

Smrek and Kremer [192] generalized the previous model to polymeric systems composed of a mixture of polymers with different thermal activities through a rigorous theoretical approach to entangled polymer solutions. Along the line of the previous section, they showed that two sets of chains which have different temperatures undergo *out-of-equilibrium* phase separation similarly to classical *equilibrium* phase separation observed in polymer mixtures [2].

In particular, Smrek and Kremer proposed to consider only a small activity difference and they showed that the critical ratio $D = D_{cold}/D_{hot}$ decreases with the length of polymers, analogously to the Flory-Huggins theory for equilibrium phase separation of polymer mixtures [2]. The critical Flory interaction parameter χ has been defined to quantify the asymmetry of the interaction between the two polymer species and it drives their segregation. For polymer mixtures, the parameter results inversely proportional to the polymer length N. The competition between the interaction, which tends to separate polymers is proportional to MN, and the entropy, which favors the mixing is proportional to number of chains M, implies a resulting $1/N$ dependence of the critical interaction parameter found in Flory-

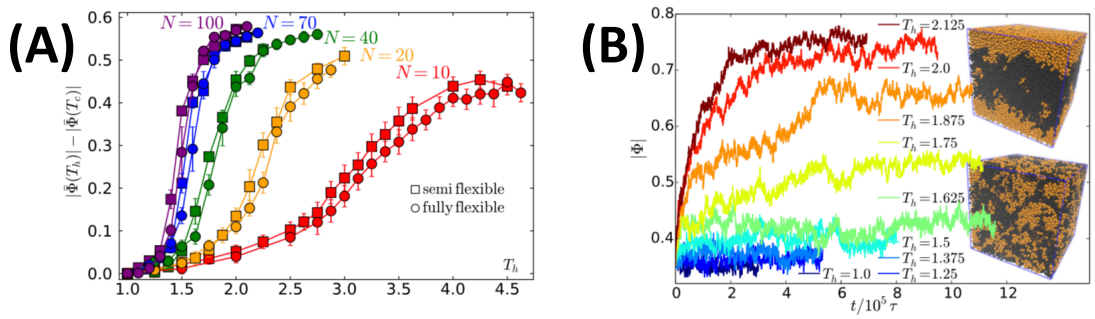

Figure 6.2: (A) The order parameter $|\bar{\Phi}|$ averaged over time and space as function of the hot temperature T_h. Various polymer sizes N are showed. Semiflexible (squares) and fully flexible (circles) chains have been compared: transition temperature is smaller for semi-flexible polymers. (B) Order parameter $|\Phi|$ as function of time for fully flexible chains in the case $N = 40$ for different T_h. Snapshots of the phase separated (top) and mixed (bottom) cases are showed in the insets. Hot (cold) particles are black (yellow). Reproduced from reference[192]

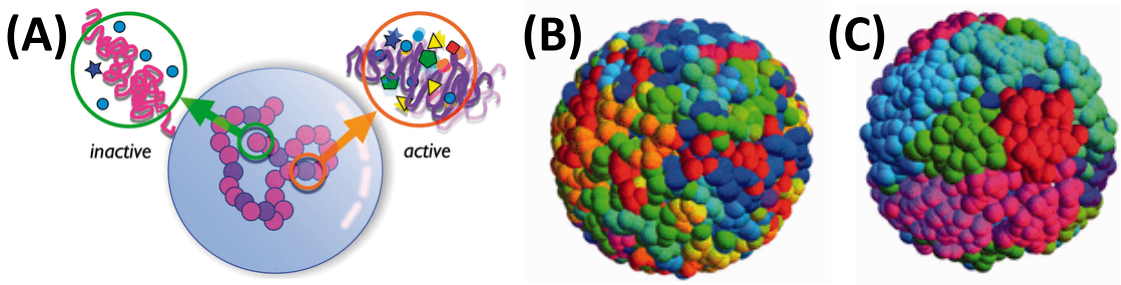

Figure 6.3: (A) Schematic of the activity-base coarse-grained model [182]: each monomer can be active and inactive, according to its gene density (mapped form experimental data). (B) and (C) The surface configuration of monomers, each chromosome has a different color: a snapshot of the model without permanent loops is plotted in (B) whereas the configurations in (C) is a snapshot of the model combining loops and activity. The simple active mechanism is not enough to achieve a spatial segregation(B); including the random loops, chromosome territories emerge (C). Reproduced from reference [182]

Huggins theory.

To generalize this argument to polymeric system with thermal activity, Smrek and Kremer [192] investigated numerically polymer melts of standard fully flexible and weakly semiflexible bead spring systems [168] with density $\rho = 0.85\sigma^{-3}$ interacting with hard-core repulsive potential. In particular, they considered linear chains with increasing lengths, from $N = 10$, up to $N = 200$. "Cold" chains have been coupled with a Langevin thermostat with temperature $T_c = 1.0\epsilon$ (Lennard-Jones units), while "hot" polymers to a Langevin thermostat with temperature $T_h > T_c$. According to this model a single chain can be only completely hot or cold.

Analogously to the work on simple particles by Weber *et al.* which has been showed in the previous section, they observed a phase separation between cold and active polymers. The phase separation has been characterized using the order parameter Φ based on the normalized number difference of the hot and the cold beads, whose dependency on polymer lengths and active temperatures is plotted in figure 6.2, panel A. In particular, they showed a decreasing of the critical temperature above which the segregation is stabilized related to the increase of the polymers length. Moreover, they compared the semi- and fully flexible systems showing that the stiffness affects the critical temperature ratio. Again, the hot polymers presents an effective interaction which leads to an enhanced excluded volume effect and to higher pressure. The resulting effect is a limitation of dynamics of the passive and more compact polymers.

A few recent studies [131, 140] have demonstrated that chromosome activity and chromosome dynamics consist of the subtle interplay between *passive* thermal diffusion and *active*, ATP-dependent motion triggered by chromatin remodeling and transcription complexes. Stimulated by active processes, chromatin dynamics influences also the motion of dispersed nanoprobes [131]. Taken together, these results suggest that the standard picture adopted so far where chromatin is modeled as a

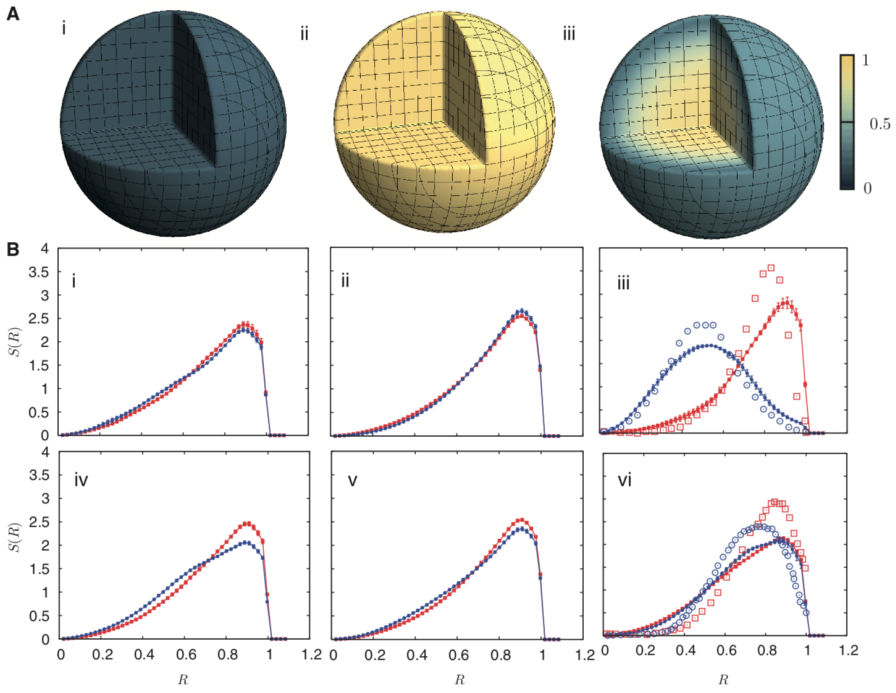

Figure 6.4: (A) Time-averaged local monomer activity distributions: the thermal equilibrium cases with uniform temperatures T_{room} in (i) and $T_a = 20\ T_{room}$ in (ii); the non-uniform activity case in (iii). (B) The activity-based segregation has been quantified studying the functions $S_i(R) = 4\pi R^2 P_i(|\vec{R}|)$ where $P_i(|\vec{R}|)$ is the probability of finding a monomer of chromosome i at a radial vector $\vec{R}$ from the origin. (i)–(iii) data for the chromosome pairs 18 (red-filled squares) and 19 (blue-filled circles); (iv)–(vi) data for the chromosome pairs 12 (red-filled symbols) and 20 (blue-filled symbols). As in panel A, the first columns are with uniform temperatures T_{room} and T_a while panels (iii) and (vi) show these distributions in the case where activity is non-uniform, illustrating that these distributions are non-trivially structured, being enhanced toward the nuclear interior in the case of the more active chromosome. Reproduced from reference [182]

passive polymer is an oversimplification.

The first attempt to include activity in a numerical polymer model for eukaryotic chromosomes was due to Ganai *et al.* [182] who argued that the emergence of chromosome territories and the non-random chromosome distribution within the nucleus is the result of differences in *non-equilibrium* activity across chromosomes originating in the local energy consuming due to the inhomogeneous distribution of ATP-dependent chromatin remodeling and transcription machinery on each chromosome (see figure 6.3, panel A).

In this model, unlike the work by Smrek and Kremer, a single chain is no more completely hot or cold: each monomer represents 1Mb domain and has been associated to its own activity. They computed the number of genes in each 1 Mb monomer unit from experimental data: single monomers containing a number of genes greater

than a certain cutoff are active, whereas the others are passive. Active and passive monomers have been associated to a local effective temperature: cold monomers are associated to the room temperature T_{room}, while hot monomers to a temperature T_a. Since the hydrolysis of a single ATP molecule liberates an energy of approximately $20k_BT_{room}$, with k_B the Boltzmann constant, the active temperature T_a has been chosen between T_{room} and 20 T_{room}. However, Smrek and Kremer argued that this assumption for the effective temperature T_a could be questioned: the hydrolysis of a single molecule of ATP releases energy of about $20k_BT_{room}$ which is not completely converted in an enhanced kinetic energy of the DNA. Moreover, this level of activity implies an activity temperature T_a which is greater than 10^4K, beyond a biologically relevant scale.

Ganai *et al.* consider the spherical chromatin domain (SCD) model [194], a generalization of the bead and springs model which includes confinement in a hard sphere and a small number of permanent loops connecting randomly chosen pairs of monomers (see figure 6.3, panel C). The introduction of random loops is necessary for the compact form of chromosomes while their inhomogeneous activity leads to the spatial segregation and to the territorial organization according to their overall activity (see figure 6.4).

6.4 Microrheology in Polymers Mixtures

As in the afore mentioned case of transcription or in the recently proposed looping extrusion mechanism [195], active processes play a fundamental role in chromosome organization. It would be interesting, then, to explore to which extent the viscoelastic properties of polymeric systems are changed by the presence of out-of-equilibrium mechanisms. Indeed, Microrheology, as we have already seen in the previous Chapters 4 and 5, is a powerful tool to investigate the viscoelastic properties of complex fluids. In this section, we will apply the microrheology framework to out-of-equilibrium polymeric systems, in continuity with the methodology used in the previous Chapter.

In particular, we will present a numerical analysis of the diffusion of nanoprobes in polymer solutions with special emphasis on the role played by the topology of polymers. To this purpose, we will compare solutions of linear vs. ring polymers in analogy to the work by Nahali and Rosa [146] and referring to the theoretical works [196, 128].

Analougsly to the work by Smrek and Kremer [192, 193], we consider out-of-equilibrium systems composed by a mixture of active and passive polymers. In that work, the mixture of active passive polymers have been investigated at high density ($\rho = 0.85\sigma^{-3}$) while we decided to restrict our analysis in the case where $\rho = 0.3\sigma^{-3}$. The motivations for this choice arise from the considerations by Nahali and Rosa [146] where the nanoprobe diffusion has been investigated in entangled polymer solutions of linear and unconcatenated ring chains. The dynamics of linear and ring shows substantial differences and, according to their results, the nanoprobe diffusion is definitely affected by chain architecture. More important, at density $\rho = 0.3\sigma^{-3}$,

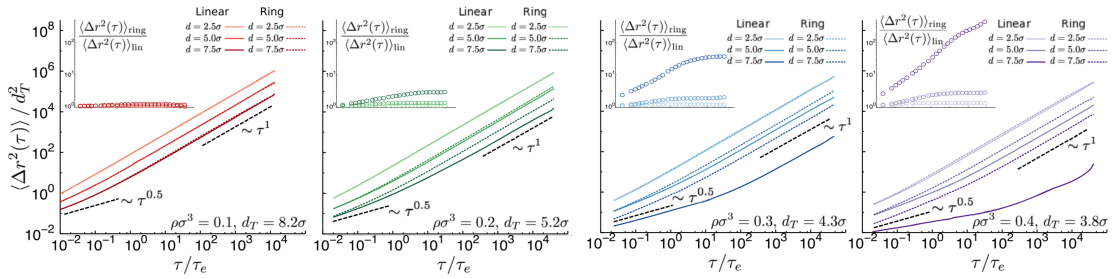

Figure 6.5: Mean-square displacements as functions of lag-time τ for nanoprobes of diameters $d/\sigma = 2.5, 5.0, 7.5$. Solid (dashed) lines indicate entangled solutions of linear polymers (unconcatenated ring polymers). In the insets the ratios between MSD of ring and linear polymers are plotted: nanobrobes in the rings systems diffuse faster when their diameter d is larger than the tube diameter d_T of the corresponding polymer solution. Reproduced from reference [146]

the various regimes can be clearly observed increasing the size of nanoprobes, as can be seen in figure 6.5. In particular, nanobrobes in systems composed by ring polymers diffuse faster when their diameter d is larger than the tube diameter d_T of the polymer solution itself.

As in the previous section, we will refer to the polymers coupled with the thermostat with higher temperature as *hot polymers*, and the polymers with the temperature of reference $T_{cold} = 1.0\epsilon$ (Lennard-Jones units) as *cold polymers*.

6.4.1 Model and Simulation Details

We investigate entangled polymer solutions constituted by a mixture of active and inactive polymers performing Molecular Dynamics simulations. We focus on the dependency of the viscoelastic properties on the activity and on the nanoprobes sizes. We consider two class of systems charaterized by two different polymer topologies, linear and unconcatenated ring chains. For reference, we will compare the obtained results to those obtained for the same systems at equilibrium, reported in refence [146].

As in the work by Smrek and Kremer [192], we consider a generalized Kremer-Grest-like [168] bead-spring model which has been described in appendix A.4. The model includes excluded volume interactions between beads (inter- and intra-chain) described by a shifted and truncated Lennard-Jones (LJ) potential while the chain connectivity (both ring and linear chains) is obtained with a FENE bond potential. Indeed, in the model, the energy scale is set by the thermal energy $\epsilon = \kappa_B T$ and the length scale is set by σ both of which are set to unity in our simulations. Consequently, all quantities are reported in reduced LJ units for consistency.

As motivated in the previous section, the overall density of the systems is $\rho = 0.3$ σ^{-3} which corresponds to the Kuhn segment density $\rho_K l_K^3 = 30$.

The potential describing the nanoprobe-nanoprobe and nanoprobe-monomer interactions is described by the model potentials introduced by Everaers and Ejtehadi [197], as in the models described in Chapter 5.

The static and kinetic properties of chains and nanoprobes are studied using fixed-volume and constant-temperature Molecular Dynamics (MD) simulations with implicit solvent and periodic boundary conditions. MD simulations are performed using the LAMMPS package [169]. The equations of motion are integrated using a velocity Verlet algorithm, in which all beads are weakly coupled to a Langevin heat bath with a local damping constant $\Gamma = 0.5\tau_{\mathrm{MD}}^{-1}$ where $\tau_{\mathrm{MD}} = \sigma(m/\epsilon)^{1/2}$ is the Lennard-Jones time and $m = 1$ is the conventional mass unit for monomer and colloidal probes. The integration time step is set to $\Delta t = 0.006\tau_{\mathrm{MD}}$. The length of each MD run is equal to $2.4 \times 10^7 \tau_{MD}$ plus 5×10^6 equilibration steps.

Then, the viscoelastic properties of the different chromatin systems have been explored by monitoring the diffusion of nanoprobe particles with increasing diameters $d/\sigma = 2.5, 5.0, 7.5$, comparable with the tube diameter $d_T = 4.3\sigma$.

The initial configurations for entangled linear polymers and unconcatenated ring polymers are obtained from the equilibrated configurations computed in reference [146] where the properties of the homogeneous systems have been extensively analysed: in particular the entanglement time $\tau_e \approx 490\tau_{MD}$, the correlation length $\xi \approx 1.3\sigma$ and the tube diameter $d_T = 4.3\sigma$. Our systems are composed by $N_{pol} = 80$ ring or linear chains of $N_{mon} = 500$ monomers of diameter σ; $N_{pol}/2$ hot polymers are associated to the thermostat corresponding to the higher temperature T_{hot} while the reaming $N_{pol}/2$ cold polymers to the thermostat at the reference temperature $T_{cold} = 1.0\epsilon$. In particular, we consider several cases with a normalized difference of temperature between the two thermostat $\Delta T = (T_{hot} - T_{cold})/T_{cold} = 0.0, 0.5, 1.0$.

6.4.2 Results and Discussion

The status of out-of-equilibrium of the system is a consequence of two causes, the thermal activity and the polymeric nature of the system. The thermal activity generates a permanent current exchanging energy from the hot polymers to cold ones which pushes the system towards a dynamical phase separation. The second cause is also related to thermal activity: the initial configurations are obtained at equilibrium and then led out-of-equilibrium by the thermal activity which affects their slow relaxation dynamics. As we will show in this section, the effective dynamics of polymers depends on their topologies and affects the diffusive dynamics of nanoprobes embedded in the mixture. We begin our investigation with the analysis of the static and dynamical properties of polymers, comparing entangled polymer solutions of linear and unconcatenated ring chains. Then, we will consider the nanoprobes properties.

Polymers Properties

In order to study the influence of the activity on the averaged and static properties of polymers, we consider various observables.

The mean-square gyration radius $\langle R_g^2 \rangle$ at various active temperatures gives a measure of the effective spatial occupation of each type of polymer. Indeed, the mean-square gyration radius, normalized with the value of the same system at equi-

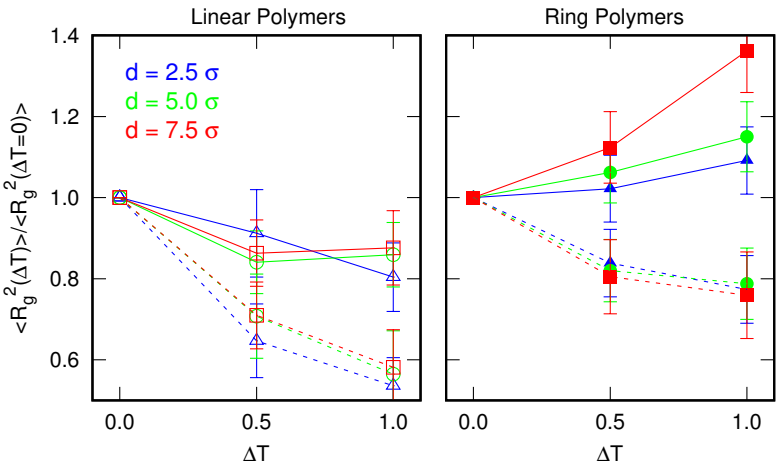

Figure 6.6: Ratio between the value of the mean-square gyration radius $\langle R_g^2(\Delta T)\rangle$ of hot (cold) polymers diffusing in the mixtures with ΔT and the value corresponding to the uniform system with $\Delta T = 0$. Continuous lines refer to cold polymers and dashed lines to hot polymers. The error bars are computed averaging on single configuration before, and then over time.

librium, exhibits a different dependence on the normalized difference of temperature between the two thermostat ΔT for the two chain architectures. The results are plotted in figure 6.6: continuous lines refer to cold polymers while dashed lines to hot polymers. Increasing ΔT, passive polymers show a strong tendency to became more compact independently of the polymer type. Instead, active polymers have an opposite behavior: they also tend to compact with a smaller extent in the case of linear chains (see figure 6.6, panel A) while in the case of the ring chains the radius of active polymers grows substantially as the temperature difference ΔT increases (see figure 6.6, panel B).

Then, we consider the pair correlation functions of monomers, $g_{cold,cold}(x)$, $g_{hot,hot}(x)$ and $g_{cold,hot}(x)$, where x is the distance between two monomers, to quantify how the density varies as a function of distance relating polymers of the same (or different) type. The various graphs reported in figure 6.7 show small differences by varying ΔT. Only the function $g_{hot,cold}(x)$ is slightly reduced when the activity of polymers increases and indicates a small tendency of the system to demix, in particular in a more marked way for the linear chains.

In addition, we consider the overlap functions $q_{cold,cold}(L_c)$, $q_{hot,hot}(L_c)$ and $q_{cold,hot}(L_c)$ of polymers which is defined as a normalized local density: for each chain, the distance x between two monomers separated by a given contour length L_c is computed; the overlap function is defined as the overall monomer density within a sphere with center in the first monomer and radius x (a schematic representation is depicted in figure 6.9). This observable can quantify if chains with the same (or different) temperature are mixed together. In figure 6.8, we can observe the overlap functions in the various cases. As suggested by the pair correlation functions, overlap functions do not change substantially. We note that only the systems containing the largest

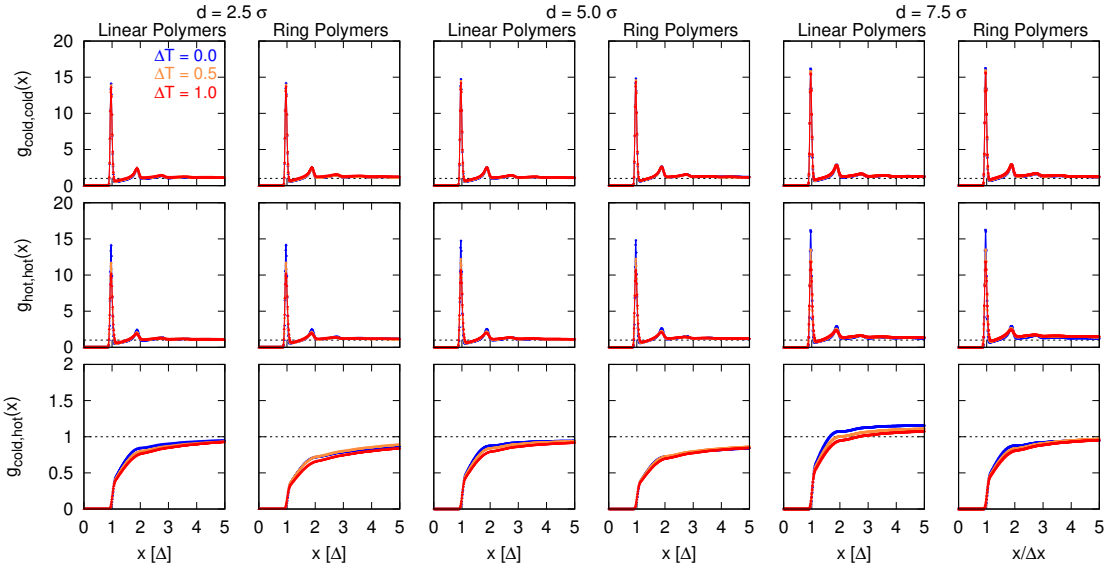

Figure 6.7: Pair correlation functions of monomers $g_{cold,cold}(x)$, $g_{hot,hot}(x)$ and $g_{cold,hot}(x)$ computed for each type of polymer where x is the distance between two monomers. We compare different values normalized difference of temperature $\Delta T = 0.0, 0.5, 1.0$. Various diameters values of nanoprobe diameter have been considered $d/\sigma = 2.5, 5.0, 7.5$.

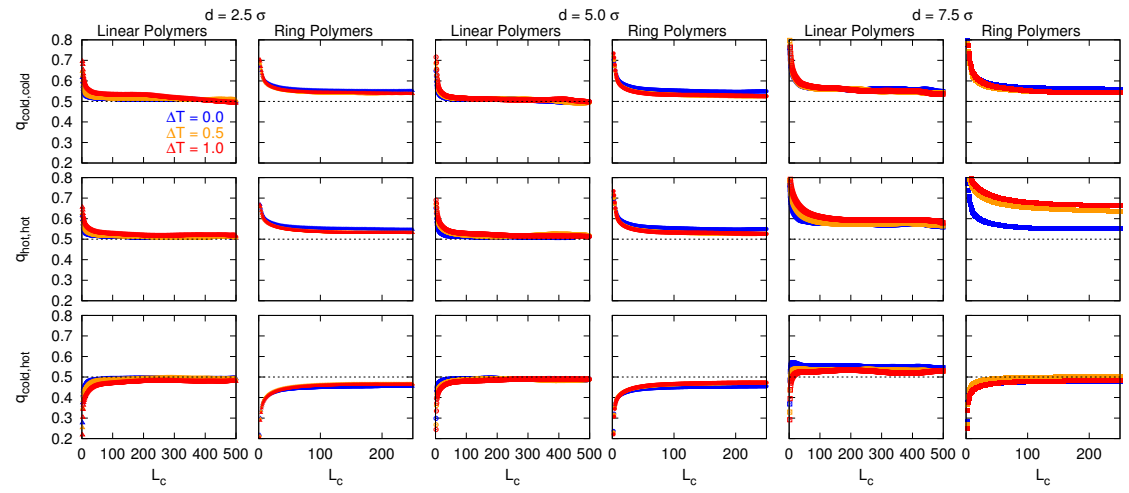

Figure 6.8: Averaged overlap functions $q_{cold,cold}(L_c)$, $q_{hot,hot}(L_c)$ and $q_{cold,hot}(L_c)$ as a function of contour length L_c. We compare different values normalized difference of temperature $\Delta T = 0.0, 0.5, 1.0$. Various diameters values of nanoprobe diameter have been considered $d/\sigma = 2.5, 5.0, 7.5$.

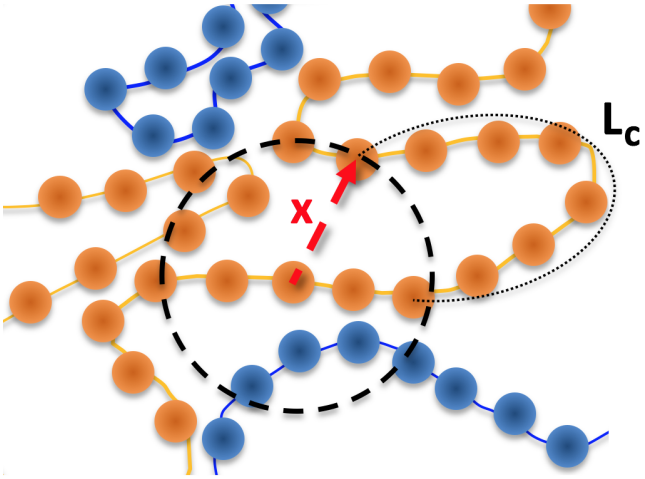

Figure 6.9: Schematic representation of the overlap functions. Given two monomers separated by a given contour length L_c and a spatial distance x, the overlap function is defined as the overall monomer density within the sphere with center in the first monomer and radius x.

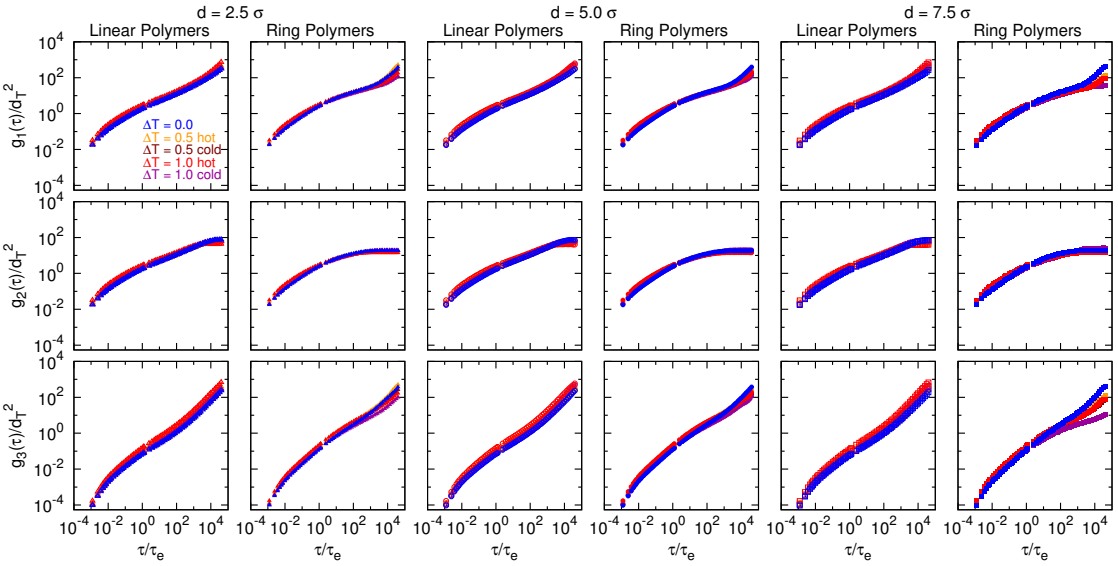

Figure 6.10: Polymers mean-square displacement $g_1(\tau)$, $g_2(\tau)$ and $g_3(\tau)$ *v.s.* time. We compare different values normalized difference of temperature $\Delta T = 0.0, 0.5, 1.0$. For each value of ΔT two curves are plotted, referring to hot and cold polymers. For $\Delta T = 0.0$ only one curve is present. Various diameters values of nanoprobe diameter have been considered $d/\sigma = 2.5, 5.0, 7.5$. All the panels are defined along the same range.

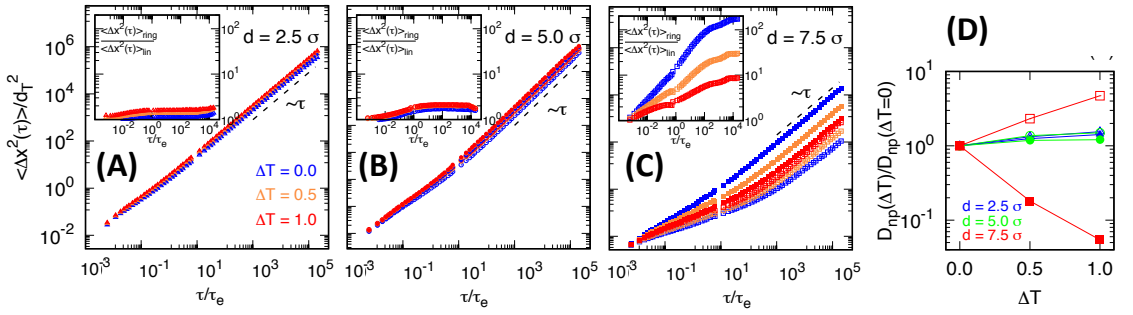

Figure 6.11: (A), (B) and (C): Lag-time dependence of mean-square displacements $\langle \Delta r^2_{np}(\tau) \rangle$ of nanoprobes for different diameters ($d/\sigma = 2.5, 5.0, 7.5$, indicated respectively with triangles, circles and squares). Data refers to entangled linear polymers (blank points) and unconcatenated ring polymers (full points) for various differences of temperature ΔT. Insets contain the ratios $\langle \Delta r^2(\tau) \rangle_{lin} / \langle \Delta r^2(\tau) \rangle_{ring}$. The diffusion of nanoprobes with diameter greater than the tube diameter is affected more clearly by the difference of temperature. (D): Ratios between diffusion coefficient $D_{np}(\Delta T)$ of nanoprobes in a system with a given different of temperature ΔT and the diffusion coefficient of nanoprobes in an homogeneous system.

size nanoprobes, $d = 7.5\sigma$, exhibits a peculiar behaviour, we will analyse deeper in the following discussion on the nanoprobes dynamics.

Now, we discuss the dynamical properties of polymers for each set of parameters. We compare the mean square displacement (MSD) of both cold and active polymers, performing time and ensemble averages. We compute the mean-square displacement of monomers in the global center of mass reference system $g_1(\tau)$, in the single polymer center of mass reference system $g_2(\tau)$ and the mean-square displacement of the centers of mass of polymers $g_3(\tau)$. The functions are plotted in figure 6.10. In general, the differences are marginal. The curves show that systems with higher global effective temperatures exhibit greater diffusion, as the equilibrium cases would suggest, and in the same way, hot polymers diffuse more than cold polymers. Moreover, even chain architectures have a small effect. The $g_3(\tau)$ functions are more interesting to highlight the differences in the dynamical behavior of the polymer systems, particularly in the case of ring chains: counter-intuitively, the diffusive motion of polymers (both cold and hot) slows down when the activity is increased despite the higher temperature of overall systems would suggest the opposite tendency.

Nanoprobes Properties

To characterize nanoprobe motion, we consider the time and ensemble averages of the mean-square displacement for nanoprobes as defined in equation 5.5. The displacements for the different set-up's considered in this work are showed in figure 6.11, while the insets display the corresponding ratio between displacements computed for ring and linear chains $\langle \Delta x^2(\tau) \rangle_{ring} / \langle \Delta x^2(\tau) \rangle_{lin}$ which grows with the nanoprobes size. The motion of the two smallest nanoprobes considered $d/\sigma = 2.5, 5.0$ are in

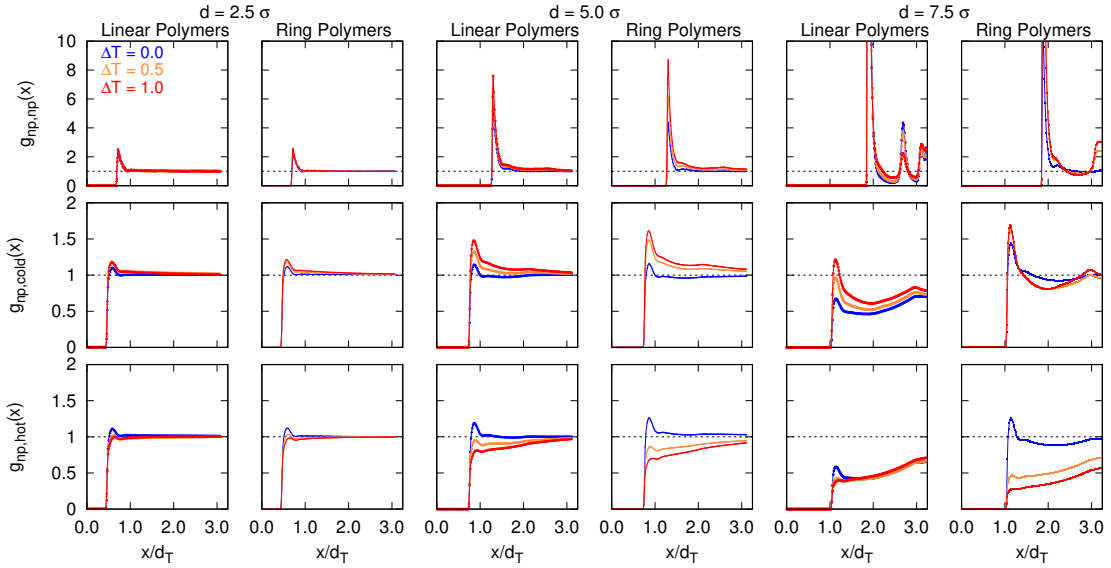

Figure 6.12: Pair correlation functions of nanoprobes $g_{np,np}(x)$, $g_{np,cold}(x)$ and $g_{np,hot}(x)$, where x is the distance between two nanoprobes or a nanoprobe and a monomer. The plots are scaled using the tube diameter d_T as typical length scale of the system. We compare different values normalized difference of temperature $\Delta T = 0.0, 0.5, 1.0$. Various diameters values of nanoprobe diameter have been considered $d/\sigma = 2.5, 5.0, 7.5$.

good agreement with the results obtained by Nahali and Rosa [146]. For $d = 7.5\sigma$, the behavior is unexpected and surprising. In the case of linear polymers melt, the diffusion coefficient of nanoprobes increase with the temperature, as expected considering the corresponding rise in the effective temperature of the full system. On the contrary, the nanoprobes diffusing in the melt of ring polymers have the opposite behavior: their diffusion slows down when the temperature is increased despite the injection of energy due to the thermal energy of polymers with a greater temperature. The diffusion coefficients computed are summarized in figure 6.11, panel D.

Then, we consider the pair correlation functions of nanoprobes, $g_{np,np}(x)$, $g_{np,cold}(x)$ and $g_{np,hot}(x)$, which have been plotted in figure 6.12. According to $g_{np,cold}(x)$ and $g_{np,hot}(x)$, nanoprobes are mainly attached to cold polymers and this tendency increase with the normalized difference of temperature ΔT. The opposite behavior can be observed for hot polymers. Moreover, this effect is more enhanced for solutions of ring polymers and for bigger nanoprobes.

A more insightful view into nanoprobe motion is given by the self-part of so-called van-Hove function [174], defined with equation 5.6. We have calculated $P(\tau; \Delta x)$ for the three representative cases $\tau/\tau_e = 10^{-3}, 1, 10^3$ and compared them to to the Gaussian distribution (black solid lines). As we can see in figure 6.14, the van-Hove function exhibits a sort of *shape transition*: for small nanoprobes with $d = 2.5, 5.0\sigma$ with any ΔT and for any chain architecture, the van-Hove function is a Gaussian. Instead, in the case $d = 7.5\sigma$, the scenario changes: for melts of

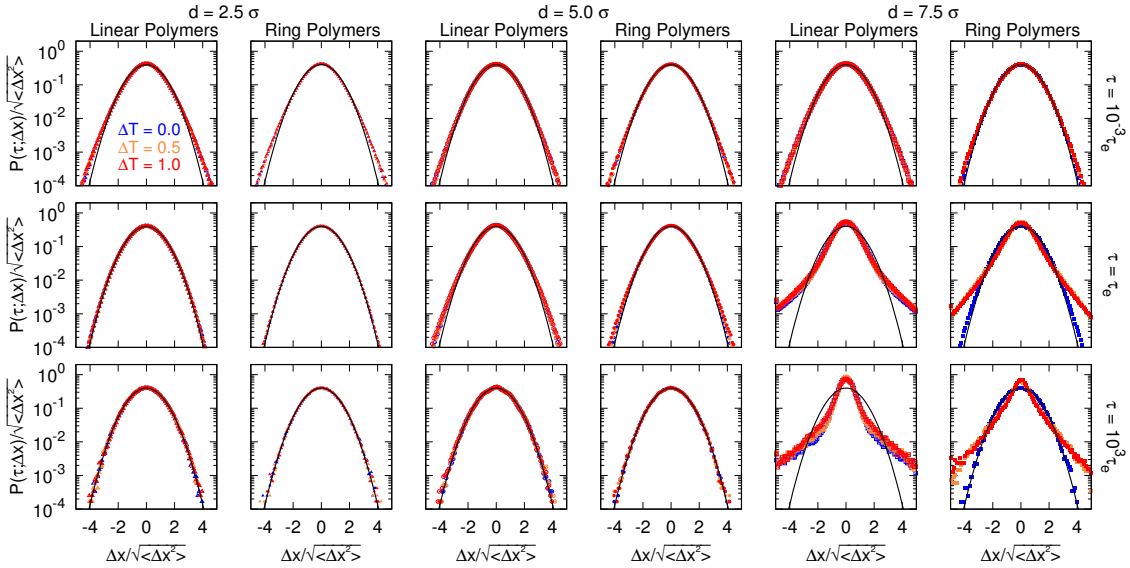

Figure 6.13: Probability distribution function of one-dimensional nanoprobes displacements, $P(\tau;\Delta x)$ (equation. 5.6) at the three representative lag-times $\tau/\tau_e = 10^{-3}, 1, 10^3$ and for different nanoprobe diameters (d). Black solid lines correspond to the Gaussian distribution function typical of normally-diffusive processes. Different colors correspond to the various differences of temperature $\Delta T = 0.0, 0.5, 1.0$.

linear chains, for short time $P(\tau;\Delta x)$ is still Gaussian while for $\tau = \tau_e$ or $10^3\tau_e$ the distributions exhibit *heavy-tail* correlations even in the case $\Delta T = 0$. In the melts of ring polymers, the case $\Delta T = 0$ shows a Gaussian distribution for any time, while for $\tau = \tau_e$ or $10^3\tau_e$, even a small activity affects $\Delta T > 0$, $P(\tau;\Delta x)$ which deviates from the Gaussian distribution showing heavy-tail correlations.

A simple way to have more information is by considering the probability distribution functions for the angle θ between oriented nanoprobe spatial displacements separated by lag-time τ, which has been already defined as equation 5.7. The distribution $P(\tau;\theta)$ for the different set-up's and the same lag-times used in figure 6.13 are plotted in figure 6.14. The distributions are compared with the "random" distribution $P(\theta) = \sin\theta/2$ (black solid lines). Clearly these correlations mirror the behaviors of corresponding $P(\tau;\Delta x)$'s (see figure 6.11), in particular they emerge whenever nanoprobe size is larger than the tube diameter d_T.

The presence of heavy-tail correlations in the van-Hove function is in general associated to heterogeneous single-particle dynamics in glassy and jammed systems [146, 149, 174, 175]. To check for spatial heterogeneity, we consider the curves $\Delta x^2_{\rm np}(T;\tau)/\langle\Delta x^2(\tau)\rangle$ as functions of the measurement time T for the entire set of $N_{\rm np}$ nanoprobes. For ergodic systems, at any chosen lag-time τ we expect that the different curves should all narrow towards ≈ 1 in the limit of large measurement time T, while heterogeneity arising from nanoprobe trapping should manifest in the spread of the different curves around the mean value. Figure. 6.15 shows that for small nanoprobe size, the ergodicity is not affected by the thermal activity. On the contrary, for $d = 7.5\sigma$, the different curves which remain stably separated since the

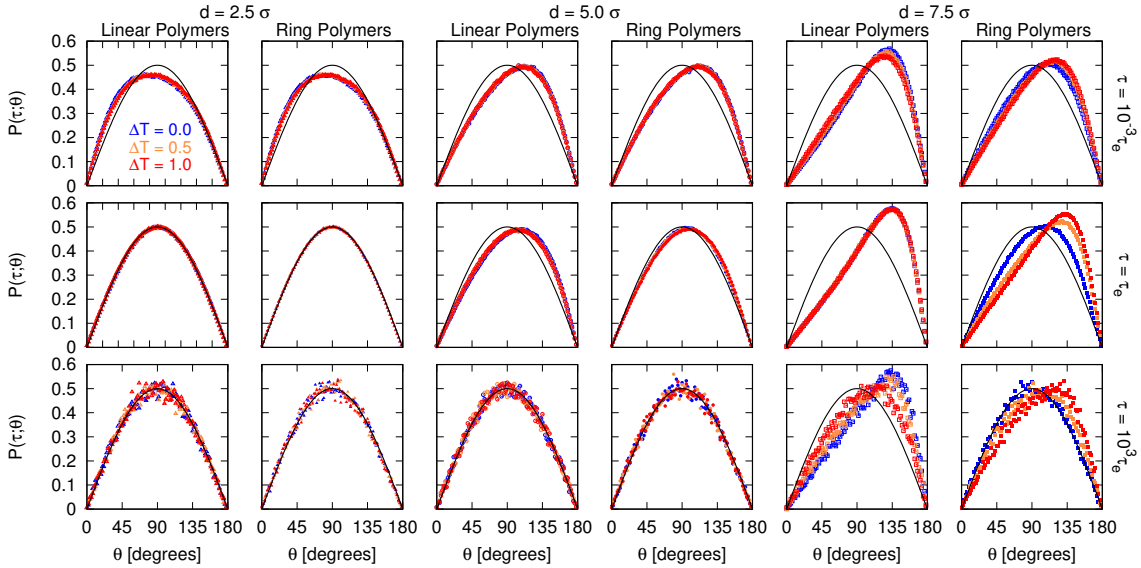

Figure 6.14: Probability distribution functions $P(\tau;\theta)$ for the angle θ between pairs of oriented, τ-lagged nanoprobe spatial displacements at the three representative lag-times $\tau/\tau_e = 10^{-3}, 1, 10^3$ taken consecutively along the trajectory. Black solid lines are for the curve $P(\tau;\theta) = \sin\theta/2$ for randomly orientated vectors. Different colors correspond to the various differences of temperature $\Delta T = 0.0, 0.5, 1.0$.

nanoprobe size is bigger than the tube diameter d_T of the solution, independently of the activity.

6.5 Conclusions

In this Chapter, we have described the viscoelastic properties of a minimal numerical model for polymer solutions composed by mixture of active/passive polymers. The numerical approach to microrheology is similar to the one described in Chapter 5, while the polymer model was inspired by the work [146] where the density of the solution is considerably high and, thus, excluded volume and topological constraints between the different chains can be simulated more effectively.

We observed that, even with small activity, active and passive polymers have a certain tendency to demix although this effect remains small. In spite of this, the nanoprobe dynamics is affected and displays non trivial effects related to the topology of the polymer chains.

The more surprising phenomenon regards how nanonoprobes diffuse: in the case of linear polymers melt, the diffusion coefficient of nanoprobes increase with the difference of temperature while in the melt of ring polymers it has the opposite behavior and nanoprobes diffusion slows down (see figure 6.11). This aspect seems to be coherent with the pair correlation functions (see figure 6.12), which indicate that the dynamics of nanobres is more coupled with cold polymers in the case of ring polymers.

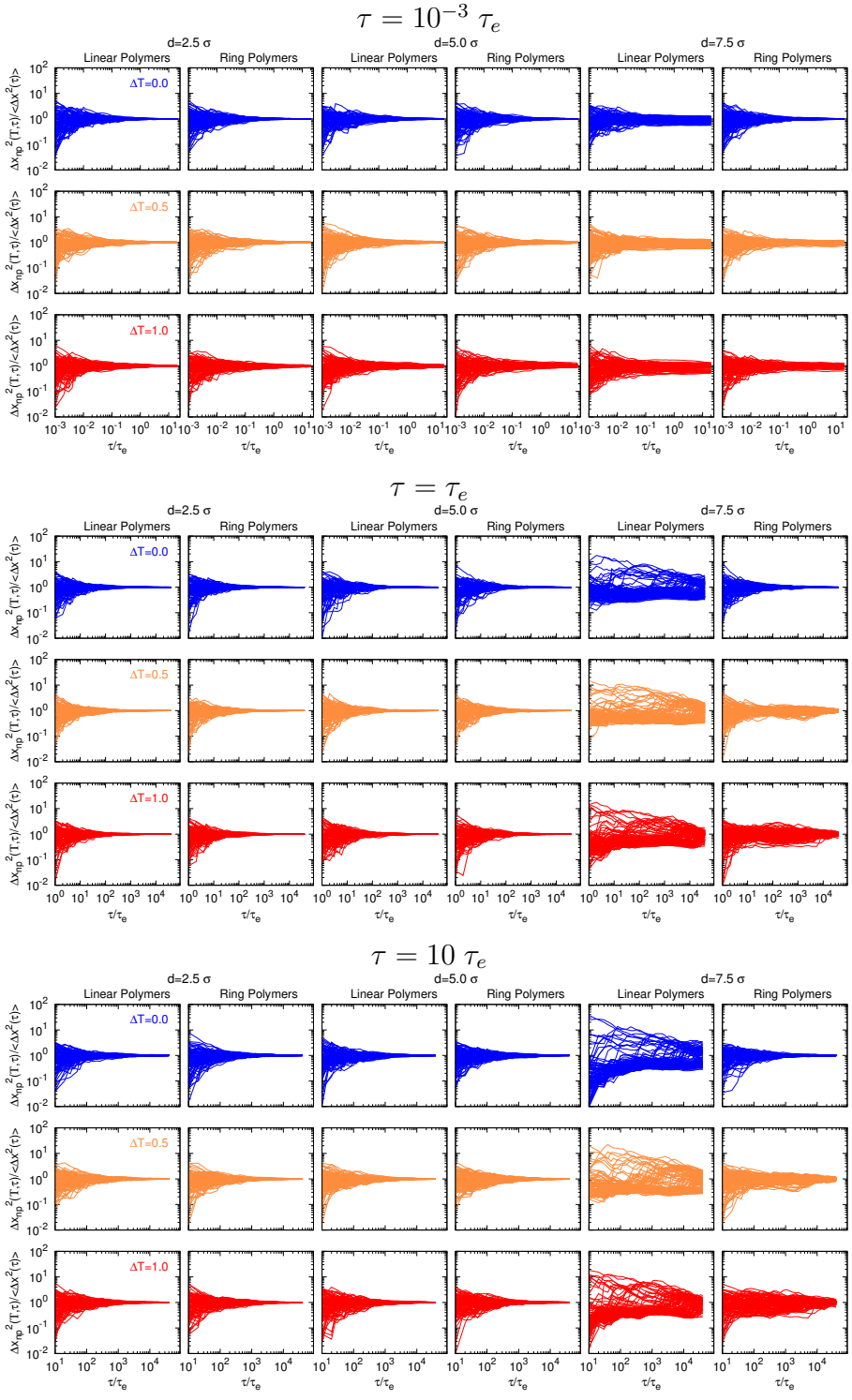

Figure 6.15: Spatial heterogeneity of mean-square displacements $\Delta x^2_{\mathrm{np}}(T;\tau)/\langle\Delta x^2(\tau)\rangle$ *vs.* the measurement time T at the three representative lag-times $\tau/\tau_e = 10^{-3}, 1, 10$, for the different nanoprobe diameters (d) and different activities ΔT. Different colors correspond to the various differences of temperature $\Delta T = 0.0, 0.5, 1.0$.

We showed that the tube diameter d_T sets the length-scale above which nanoprobe motion becomes more affected by the dynamics of polymers due to difference of temperature which lead the system out-of-equilibrium. In particular, distribution functions of spatial displacements show heavy-tail behavior (see figure 6.13) and non-random directional correlations (see figure 6.14) and the nanoprobe motion is no longer ergodic and manifests some distinctive features which typically arise in glassy systems, such as heterogeneous behavior (see figure 6.15).

Chapter 7

Conclusions

In this Thesis, we have investigated the physical properties of certain particular realizations of melts of entangled polymers. Although the motivation behind these studies has to be found in our interest to understand the generic features of chromosome organization during interphase, we employ tools and methodologies which are fully general and, so, they go beyond this specific biological problem.

Specifically, we have studied the following problems:

1. In Chapter 3 and inspired by previous work on the relationship between chromosome structure and epigenetic domains, we have introduced and analyzed physical properties of the classical Ising model with nearest-neighbor interaction for spins located at the monomers of long linear and branched polymer chains in dilute solutions and melts in 2 and 3 dimensions. The reasons that motivated us to study this problem were the following: the analogy between the large scale behavior of chromosome conformations and the folding of branched crumpled polymers in dense solutions (see Chapter 1) and recent works on polymer models for chromatin where epigenetic states are treated as internal degrees of freedom coupled through local nearest-neighbor interactions (see Chapter 3). We have compared results for two ensembles of polymers with very different single chain properties: swollen, self-avoiding linear polymer chains in good solvent conditions and compact, space-filling randomly branching polymers in melt. By employing a mean-field approach and Monte Carlo computer simulations, we show that swollen polymers cannot sustain an ordered phase. On the contrary, compact polymers may indeed produce an observable phase transition. Finally, we briefly consider the statistical properties of the ordered phase by comparing polymer chains within the same universality class but characterized by very different shapes.

2. In the second part of the Thesis, we have reviewed (Chapter 5) recent literature concerning the applications of microrheology for exploring the viscoelastic properties of the nuclei of the eukaryotic cells.

   Motivated by this phenomenology, we have performed numerical simulations of a generic polymer model for chromatin fibers in interphase which includes

the presence of stable binding interactions to an extra-chromatin nuclear matrix. To study how these constraints affect chromatin structure from small to large scales, we employ extensive molecular dynamics computer simulations and we monitor the motion of nanoprobes of different sizes embedded within the polymer medium. Our results demonstrate that nanoprobes undergo hampered motion whenever their linear size becomes larger than chromatin stiffness. This transition is also displaying certain features which typically belong to the realm of glassy systems, namely long-tail correlations in the distribution functions of nanoprobe spatial displacements and heterogeneous behavior accompanied by ergodicity breaking.

3. Finally, in Chapter 6, we have applied microrheology to study the internal structure of out-of-equilibrium entangled polymer solutions. More specifically, in our approach we have considered mixtures of active and passive polymers originating by the coupling to different Langevin thermostats in molecular dynamics computer simulations. By tracking the motion of nanoprobes embedded in the solution we show that nanoprobe dynamics depends upon the topology of the polymer chains considered. In fact, while the diffusion of nanoprobes increases in a mixture of linear chains as the difference of temperature grows, it surprisingly slows down when nanoprobes are embedded in a ring polymers melt.

To conclude, we have obtained novel results on a number of different projects which are deeply related to the physics of entangled polymer solutions and the physics of chromosome structure. Of course, our models contains a certain number of approximation and additional research work is necessary to improve and generalize our results.

Appendix A

Methods

A.1 Self-Avoiding Walks and Randomly Branching Polymers in Melts

In this section we report the main features for Self-avoiding walks (SAW) and Randomly branching polymers (RBP) in melts which has been used in chapter 3. Examples have been plotted in figure 3.6.

A.1.1 Self-Avoiding Walks

The average linear size or gyration radius of self-avoiding linear walks (SAW's) with excluded volume interactions (good solvent conditions [2]) in d dimensions increases with the number of monomers N as $R_g \sim N^{\nu}$ with $\nu = 3/(d+2)$ and, hence, single polymer conformations are not space-filling.

Spatial conformations of single SAW's in 2 and 3 dimensions were generated according to the dynamical Metropolis Monte Carlo algorithm known as the *pivot* algorithm, see for details reference [117]. Briefly, a single polymer chain made of $N+1$ monomers ($= N$ bonds) is initially arranged along a straight line on the $2d$ or $3d$ cubic lattices. Then, one of the monomers of the chain is chosen randomly and the shortest of the two sub-chains centered on the selected monomer reoriented along a randomly chosen direction. If the move causes an overlap between any of the possible $N(N+1)/2$ pairs of monomers it is rejected, otherwise the conformation is accepted and the algorithm applied again. The route to equilibrium is monitored by calculating the auto-correlation time [117] of the gyration radius. By applying repeatedly the described algorithm, we have generated ensembles of 10^4 statistically independent self-avoiding polymer chains made of $16 \leq N \leq 4096$ bonds.

A.1.2 Randomly Branching Polymers in Melts

At odds with SAW's, the average gyration radius of randomly branching polymers (RBP's) in melt conditions increases with the number of monomers N as

$R_g \sim N^\nu$ with $\nu = 1/d$ [18, 17, 23], thus they constitute typical examples of compact, space-filling polymers.

Spatial conformations of RBP's made of $N + 1$ monomers in $2d$ and $3d$ melts composed of M chains were generated according to the lattice tree model as described in references [23, 115, 118]. In detail, we have simulated RBP's with volume interactions by employing a slightly modified version of the "amoeba" Monte Carlo algorithm [198] for trees on the cubic lattice with periodic boundary conditions. In the model, connected nodes occupy adjacent lattice sites. As there is no bending energy term, the lattice constant equals the Kuhn length, l_K, of linear paths across ideal trees. The functionality of nodes is restricted to the values $f = 1$ (a leaf or branch tip), $f = 2$ (linear chain section) and $f = 3$ (branch point). Here, we consider $2d$ and $3d$ trees in melt with Kuhn density $\rho_K l_K^d = 2$. We have considered polymer chains made of $10 \leq N \leq 900$ bonds, with a total number of chains in the range $32 \leq M \leq 384$ and 100 independent melt configurations. For more details on the polymer model and the quantitative analysis of chains statistics, the interested reader is invited to look into former works, references [23, 115, 118].

A.2 MonteCarlo Algorithm for Ising Model: the Wolff Algorithm

Here, we report the Wolff Algorithm [119], used for performing Monte Carlo simulations in Chapter 3, which is a cluster algorithm more efficient if compared with standard single-spin-flip algorithms.

In general, we consider a lattice composed by N sites with spin variables $\sigma_i \in \{+1, -1\}$. Choosing a random initial spin $\sigma^{(0)}$, we construct a cluster by adding, with probability p, neighboring spins $\sigma_i^{(1)}$ which have the same orientation of $\sigma^{(0)}$. Recursively, we include in the cluster, with the same probability p, also the spins $\sigma_i^{(2)}$, first-neighbors of $\sigma_i^{(1)}$ and with its same orientation. When this procedure is interrupted, the spins which belong to the cluster are flipped. This procedure changes the configuration (A) to the configuration (B), as depicted in figure A.1. The probability to include a spin p is a parameter chosen in order to respect the detailed balance between the configurations (A) and (B).

For the configurations (A) and (B), the a priori construction probabilities are $\Theta(A \to B)$ and $\Theta(B \to A)$, the acceptance probabilities $P(A \to B)$ and $P(B \to A)$, and the Boltzmann weights $\pi(A)$ and $\pi(B)$. All together have to respect the detailed balance condition:

$$\pi(A) \cdot \Theta(A \to B) \cdot P(A \to B) = \pi(B) \cdot \Theta(B \to A) \cdot P(B \to A).$$

The a priori probability $\Theta(A \to B)$ corresponds to the probability of building a cluster up to a certain level instead of continuing with the process by including more spins. Indeed, the a priori probability is the product of probability to build the interior cluster, times the stopping probability at the boundary. Indeed, the boundary of the cluster ∂C, has n_1 edge connections between neighboring spins

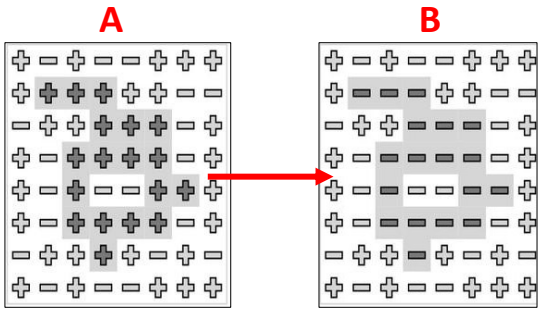

Figure A.1: Example of flipping of a cluster using Wolff algorithm. Reproduced from reference [120] with modifications.

with the same sign ($++$ or $--$) and n_2 with opposite sign ($+-$ or $-+$). As a result, the a priori probability is $\Theta(A \to B) = \Theta_{in} \cdot (1-p)^{n_1}$, where $(1-p)$ is the probability of the n_1 spins to not be included in the cluster. For the opposite procedure $\Theta(A \to B) = \Theta_{in} \cdot (1-p)^{n_2}$ since, n_2 are the opportunities to grow the cluster which has not been accepted.

Then the detailed balance condition results:

$$e^{-\beta(n_2-n_1)} \cdot (1-p)^{n_1} \cdot P(A \to B) = e^{-\beta(n_1-n_2)} \cdot (1-p)^{n_2} \cdot P(B \to A).$$

Consequently, the acceptance probability is

$$\begin{aligned} P(A \to B) &= min\left[1, \frac{e^{-\beta(n_1-n_2)} \cdot (1-p)^{n_2}}{e^{-\beta(n_2-n_1)} \cdot (1-p)^{n_1}}\right] \\ &= min\left[1, \left(\frac{e^{-2\beta}}{1-p}\right)^{n_1} \cdot \left(\frac{1-p}{e^{-2\beta}}\right)^{n_2}\right]. \end{aligned}$$

This general algorithm recovers the Wolff Algorithm when the acceptance probability is chosen appropriately as $p = 1 - e^{-2\beta}$: the resulting acceptance probability $P(A \to B)$ is then equal to one. In this way, the recursive process involves only the construct a cluster, which is automatically flipped.

A.3 Microrheology

Microrheology [136] is a technique used to compute the complex shear modulus $\tilde{G}(\omega) = G'(\omega) + iG''(\omega)$ of a medium tracking the diffusive thermal motion of nanoprobes injected in such medium. In this Appendix we report some theoretical considerations which can be useful to clarify some aspects analyzed along this Thesis.

A.3.1 Shear Modulus

Here we demonstrate the equation 4.1 for the computation of the complex shear modulus $\tilde{G}(\omega)$. Firstly, we consider he diffusive thermal diffusion of nanoprobes

injected in the medium. The motion of each of these particles can be described through a generalized Langevin equation:

$$M\frac{d\mathbf{v}\left(t\right)}{dt}=-\int_{0}^{t}\gamma\left(t-\tau\right)\mathbf{v}\left(\tau\right)d\tau+\boldsymbol{\eta}\left(t\right) \tag{A.1}$$

where M is the mass of the particle, v its velocity and $\eta(t)$ is the stochastic force describing the interaction with the surrounding medium. The function $\gamma(t)$ represents the (time-dependent) memory kernel. By using the fluctuation-dissipation relation

$$\left\langle \boldsymbol{\eta}\left(t\right)\cdot\boldsymbol{\eta}\left(t'\right)\right\rangle =6k_{B}T\gamma\left(t-t'\right)$$

and the Laplace transform of equation A.1, we get:

$$Ms\tilde{\mathbf{v}}\left(s\right)-M\mathbf{v}\left(0\right)=-\tilde{\gamma}\left(s\right)\tilde{\mathbf{v}}\left(s\right)+\tilde{\boldsymbol{\eta}}\left(s\right)$$

$$\tilde{\mathbf{v}}\left(s\right)=\frac{M\mathbf{v}\left(0\right)+\tilde{\boldsymbol{\eta}}\left(s\right)}{Ms+\tilde{\gamma}\left(s\right)}.$$

Then, we use the equipartition theorem, which sets the relation between average square velocity and thermal energy,

$$M\left\langle \mathbf{v}\left(t\right)\mathbf{v}\left(t\right)\right\rangle =3k_{B}T\ \ \forall t$$

where $\kappa_B T$ is the Boltzmann factor at absolute temperature T, Finally, taking the thermal average, we get

$$\left\langle \tilde{\mathbf{v}}\left(s\right)\cdot\mathbf{v}\left(0\right)\right\rangle =\frac{M\left\langle \mathbf{v}\left(0\right)^{2}\right\rangle +\left\langle \tilde{\boldsymbol{\eta}}\left(s\right)\cdot\mathbf{v}\left(0\right)\right\rangle }{Ms+\tilde{\gamma}\left(s\right)}=\frac{3k_{B}T}{Ms+\tilde{\gamma}\left(s\right)}$$

where $\langle\tilde{\boldsymbol{\eta}}\left(s\right)\cdot\mathbf{v}\left(0\right)\rangle)=0$. The motion of the nanoprobes in the medium can be described through the mean-square displacement $\langle\Delta x^{2}(\tau)\rangle\equiv\langle\left(\mathbf{x}\left(t+\tau\right)-\mathbf{x}\left(t\right)\right)^{2}\rangle$ or $\langle\Delta x^{2}(\tau)\rangle=2\int_{0}^{\tau}\left(\tau-t\right)\left\langle \mathbf{v}\left(t\right)\cdot\mathbf{v}\left(0\right)\right\rangle dt$.

The Laplace transform of the memory kernel $\tilde{\gamma}\left(s\right)$ can be expressed as a function of the Laplace transform of the mean-square displacement $\langle\Delta\tilde{x}^{2}(s)\rangle=\frac{2}{s^{2}}\langle\tilde{\mathbf{v}}\left(s\right)\cdot\mathbf{v}\left(0\right)\rangle$:

$$\tilde{\gamma}\left(s\right)=\frac{6k_{B}T}{s^{2}\delta\tilde{x}^{2}\left(s\right)}-Ms.$$

We further assume that the memory kernel $\tilde{\gamma}\left(s\right)$ is proportional to the bulk frequency-dependent viscosity of the fluid, $\tilde{\eta}\left(s\right)$:

$$\tilde{\eta}\left(s\right)=\frac{\tilde{\gamma}\left(s\right)}{\nu\pi a}$$

where the parameter ν is related to the boundary condition at the particle surface ($\nu=2$ slip boundary condition, $\nu=3$ slip boundary condition) and a is the nanoprobe diameter. Finally the Laplace transform of the shear modulus $\tilde{G}\left(s\right)=s\cdot\tilde{\eta}\left(s\right)$ is:

$$\tilde{G}\left(s\right)=\frac{s}{\nu\pi a}\left[\frac{6k_{B}T}{s^{2}\langle\Delta\tilde{x}^{2}(s)\rangle}-Ms\right]\approx\frac{6k_{B}T}{\nu\pi as\langle\Delta\tilde{x}^{2}(s)\rangle},$$

where, in the second expression, the inertia term is neglected. The complex shear modulus $\hat{G}(\omega)$ defined in the Fourier-frequency space ω is obtained from $\tilde{G}(s)$ by analytical continuation and substituting the variable s with $i\omega$:

$$\hat{G}(\omega) = -i\frac{6k_BT}{\nu\pi a\omega\langle\Delta\tilde{x}^2(s=i\omega)\rangle}$$

which is called Laplace-Fourier (LF) transform. $\hat{G}(\omega)$ connects the strain induced in the material by an externally applied stress with time periodicity $= 2\pi/\omega$. In particular,

$$\hat{G}(\omega) \equiv \hat{G}'(\omega) + i\hat{G}''(\omega)\,, \tag{A.2}$$

where $\hat{G}'(\omega)$ and $\hat{G}''(\omega)$ are, respectively, the storage (elastic) and loss (viscous) moduli [2].

Equations (A.3.1) and (A.2) are best illustrated by a practical example. We consider the minimalistic model of a nanoprobe diffusing with diffusion coefficient $D = \frac{\kappa_B T}{3\pi\eta d}$ (η is the macroscopic viscosity of the medium) in a confined spherical domain of linear size Δ. In this case,

$$\langle\Delta x^2(\tau)\rangle = \Delta^2\left(1 - e^{-6D\tau/\Delta^2}\right) = \begin{cases} \Delta^2\,, & \tau\to\infty \\ 6D\tau\,, & \tau\to 0 \end{cases} \tag{A.3}$$

and the Laplace transform is:

$$\langle\Delta\tilde{x}^2(\omega)\rangle = -\frac{6D}{\omega(\omega - i\,6D/\Delta^2)}\,. \tag{A.4}$$

Thus, according to equations. (A.3.1) and (A.2) we get:

$$\begin{aligned} \hat{G}'(\omega) &= \frac{2\kappa_B T}{\pi d\Delta^2}\,, \\ \hat{G}''(\omega) &= \eta\,\omega\,. \end{aligned} \tag{A.5}$$

As expected, the functional forms of $\hat{G}'(\omega)$ and $\hat{G}''(\omega)$ mirror the intuitive fact that at low (respectively, high) frequency the medium behaves as a classical solid (resp., liquid) [122].

A.3.2 Numerical Computation of the Shear Modulus

According to the fundamental relation of microrheology, Eq. (A.3.1), the Laplace-Fourier (LF) transform of the nanoprobe mean-square displacement, $\langle\Delta\hat{x}^2(\omega)\rangle$, determines completely the complex shear modulus. Computing this quantity with good accuracy is not straightforward. Here we adopt the numerical method described by Mason [173]. This approach is the same used by Rubinstain et al. in reference [196] to compare the stress relaxation function $G(t)$ computed with the Green-Kubo formula with the effective stress relaxation function compute using the Stokes-Einstein

relation from the mean square displacement of diffusing nanoparticles. According to his approach, the storage and loss moduli are given by the (approximate) equations:

$$\hat{G}'(\omega) = |\hat{G}(\omega)|\cos(\pi\alpha(\omega)/2) \quad (A.6)$$

$$\hat{G}''(\omega) = |\hat{G}(\omega)|\sin(\pi\alpha(\omega)/2) \quad (A.7)$$

with

$$|\hat{G}(\omega)| = \left.\frac{2\kappa_B T}{\pi d\langle\Delta x^2(\tau)\rangle\Gamma(1+\alpha(\omega))}\right|_{\tau=1/\omega} \quad (A.8)$$

$$\alpha(\omega) = \left.\frac{d\log\langle\Delta x^2(\tau)\rangle}{d\log\tau}\right|_{\tau=1/\omega}. \quad (A.9)$$

$\Gamma = \Gamma(x)$ is the ordinary Euler's gamma function.

With the purpose of clarity it is important to specify the *notation* that will be used: $\tilde{G}(s) = s\mathcal{L}\{G_r(\tau)\}$ where $\mathcal{L}$ denotes the unilateral Laplace transform: $\mathcal{L}\{G_r(\tau)\} \equiv \tilde{G}_r(s) \equiv \int_0^\infty d\tau G_r(\tau)e^{-s\tau}$, which implies that, in general, $G_r(\tau) \neq G(\tau)$.

The procedure to estimate equation A.6 and A.7 involves several steps:

1. Given the mean square displacement $\langle\Delta x^2(\tau)\rangle$, we compute logarithmic derivative:
$$\alpha(s) \equiv \left.\frac{d\,ln\langle\Delta x^2(\tau)\rangle}{d\,ln\,\tau}\right|_{\tau=s}. \quad (A.10)$$
α can assume a values between zero (elastic confinement) and one (viscous diffusion) for thermally driven particles; it will be 2 in the ballistic regime.

2. Evaluation of the Laplace transform of the mean square displacement:
$$s\langle\Delta\tilde{x}^2(\tau)\rangle \approx \langle\Delta x^2(1/s)\rangle\Gamma[1+\alpha(s)] \quad (A.11)$$
where Γ is the gamma function, α function has been computed in the previous step.

3. Computation of the Laplace transform of the shear modulus $\tilde{G}(s)$ using equation A.3.1:
$$\tilde{G}(s) \approx \left.\frac{k_B T}{\pi a\langle\Delta x^2(\tau)\rangle\Gamma[1+d\,ln\langle\Delta x^2(t)\rangle/d\,ln\,\tau]}\right|_{\tau=s}. \quad (A.12)$$

4. Computation of the Fourier transform of the shear modulus using equations A.6 and A.7:
$$G'(\omega) = |G^*(\omega)|cos(\pi\alpha(\omega)/2) \quad (A.13)$$
$$G''(\omega) = |G^*(\omega)|sin(\pi\alpha(\omega)/2) \quad (A.14)$$
$$|G^*(\omega)| \approx \frac{k_B T}{\pi a\langle\Delta r^2(\omega)\rangle\Gamma[1+\alpha(\omega)]} \quad (A.15)$$

5. Computation of the logarithmic derivative of the shear modulus $\tilde{G}(s)$:

$$\beta(\tau) \equiv \frac{d\, ln\langle \tilde{G}(s)\rangle}{d\, ln\, s}\Big|_{s=1/\tau} \tag{A.16}$$

.

6. Computation of the inverse transform of $\tilde{G}(s)/s$:

$$G_r(\tau) \approx \tilde{G}(1/\tau)/\Gamma[1-\beta(\tau)] \tag{A.17}$$

which is valid when $\beta < 1$.

A.4 Molecular Dynamics Simulation: the Kremer-Grest Polymer Model

Kremer and Grest introduced a bead-spring model [168] which has been adopted as a standard model for studying generic polymer properties using Molecular Dynamics simulations. According to this model, a polymer chain composed by N beads connected by $N-1$ bonds with a suitable bending rigidity. The interaction between beads is described by:

$$\mathcal{H}_{INT} = \frac{1}{2}\sum_{i}^{N}\sum_{j\neq i}^{N} U_{LG}(r_{i\,j}) + \sum_{i\in pol}^{N-1} U_{FENE}(r_{i\,i+1}) + \sum_{i} U_{KP}(\theta_i)$$

The potential describing the excluded volume interactions between beads, avoiding overlaps, is the *shifted and truncated Lennard-Jones (LJ) potential*, or Weeks-Chandler-Andersen potential (WCA):

$$U_{LJ}(r) = \begin{cases} 4\epsilon\left[\left(\frac{\sigma}{r}\right)^{12} - \left(\frac{\sigma}{r}\right)^{6} + \frac{1}{4}\right] & r \leq r_c \\ 0 & r > r_c \end{cases}$$

where r is the distance between two monomers, $r_c = 2^{1/6}\sigma$ is the cutoff distance, corresponding to the minimum, in order to have only the repulsive contribution and ϵ is the interaction strength. The energy scale is $\epsilon = \kappa_B T$ and the length scale is σ.

The bonding potential between monomers which are nearest-neighbors along the same polymer chain is the *finitely extensible non-linear elastic potential* (FENE):

$$U_{FENE}(r) = \begin{cases} -0.5\kappa R_0^2 \ln\left(1-(r/R_0)^2\right) & r \leq r_c \\ \infty & r > r_c \end{cases}$$

where $\kappa = 30\epsilon/\sigma^2$ is the spring constant and $R_0 = 1.5\sigma$ is the maximum extension of the elastic FENE bond.

The triplets of consecutive beads are involved in the *Kratky-Porod potential* (KP), which controls polymer stiffness of the chain:

$$U_{KP}(\theta) = \kappa_\theta\,(1-\cos\theta)$$

where θ is the angle defined by adjacent bonds and $\kappa_\theta = 5\kappa_B T$ is the bending constant.

In Chapters 5 and 6 we have considered the diffusion of nanoprobes embedded in a solution of polymers. These nanoprobes have been modeled as colloids. In analogy with the work by Valet and Rosa [150], the potential accounting the nanoprobe-nanoprobe and nanoprobe-monomer interactions is described by the potentials introduced by Everaers and Ejtehadi [197] . The nanoprobe-nanoprobe is:

$$\begin{cases} U_{cc}(r) = U_{cc}^A(r) + U_{cc}^R(r) & r \leq r_{cc} \\ 0 & r > r_{cc} \end{cases}$$

where $U_{cc}^A(r)$ and $U_{cc}^B(r)$ are respectively the attractive and the repulsive contributions:

$$U_{cc}^A(r) = -\frac{A_{cc}}{6}\left[\frac{2a^2}{r^2-4a^2} + \frac{2a^2}{r^2} + \ln\left(\frac{r^2-4a^2}{r^2}\right)\right]$$

$$U_{cc}^B(r) = \frac{A_{cc}}{37800}\frac{\sigma^6}{r}\left[\frac{r^2-14ar+54a^2}{(r-2a)^7} + \frac{r^2+14ar+54a^2}{(r+2a)^7} - 2\frac{r^2-30a^2}{r^7}\right]$$

where $A_{cc} = 39.478\kappa_B T$, considering non-sticky, athermal probe particles with diameters $d/\sigma = 2.5, 5.0, 7.5$ (corresponding to $r_{cc}/\sigma = 3.08, 5.60, 8.08$).

Finally, the nanoprobe-monomer potential is:

$$\begin{cases} U_{mc}^B(r) = \frac{2a^3\sigma^3 A_{mc}}{9(a^2-r^2)^3}\left[1 - \frac{5a^6+45a^4r^2+63a^2r^4+15r^6}{15(a-r)^6(a+r)^6}\right] & r \leq r_{mc} \\ 0 & r > r_{mc} \end{cases}$$

where $A_{mc} = 75.358\kappa_B T$, $r_{mc}/\sigma = 2.11, 3.36, 4.61$.

The time evolution of polymer dynamics according the Kremer-Grest polymer model is performed by numerical integration of the Newton equations of motion of the Langevin dynamics. For each particle i, the dynamics of its position $\vec{x}_i$ evolves according the equation:

$$m\frac{d^2\vec{x}_i}{dt^2} = -\nabla\mathcal{H}_{INT} - \gamma\frac{d\vec{x}_i}{dt} + \vec{\eta}_i(t)$$

where m is the mass, γ is the friction and the $\vec{\eta}_i(t)$ is the thermal noise. In particular, the thermal noise $\vec{\eta}_i(t)$ describes the stochastic collisions of particle i with the surrounding fluid and is a Gaussian variable such that:

$$\langle \eta_{i,\alpha}(t) \rangle = 0$$

which holds $\forall t$ and where α is the axis orientation, $\alpha = x, y, z$. Moreover

$$\langle \eta_{i,\alpha}(t) \cdot \eta_{j,\beta}(t') \rangle = 2k_B T\gamma\delta_{ij}\delta_{\alpha\beta}\delta\left(t - t'\right).$$

In the Molecular Dynamics simulation which we have performed in Chapters 5 and 6, the Langevin equation is integrated numerically using LAMMPS [169] with the standard velocity Verlet algorithm.

Acknowledgements

Men at some time are masters of their fates.
The fault, dear Brutus, is not in our stars,
but in ourselves, that we are underlings.
[W. Shakespeare, Julius Caesar]

First and foremost I want to thank my supervisor, Angelo Rosa, for the continuous and patient support during these four years. His invaluable help and immense knowledge guided me through this PhD.

Then, I would like to thank Prof. Marco Baiesi and Prof. Daniel Jost for accepting to read and evaluate this manuscript.

I would also like to thank all the SBP people I have had the opportunity to meet over the years, in particular Giulia, Lucia, Stefano, Elena and Saltala.

My time at Sissa was made enjoyable in large part due to the many friends and groups that became a part of my life. I would like to mention and thank all of you. In particular:

Francesca, for your support, since the day you found me in room 132;

Martina, because despite everything we are going to touch the 10th;

Mara, for your extraordinary help (and obviously, also Sirio deserves a special mention);

Daniele, for having taught me the meaning of "sticazzi";

All that people I have met as students' representative, in particular Alessandro (Presidente!), Alessandro ("Non siamo mica ad Harvard!"), Gabriele, Veronica, Claudio and all the others. And clearly all professors with whom I had the pleasure of arguing;

All CM guys, Francesco, Luca, juraj, Daniele, Glen and Paolo, which almost adopted me during my first year;

Beatrice, Francesco, Marco Lorenzo, Francesco and all the others, even if you do not move an inch from Varese.

Lastly, I would especially like to thank my family for all their love and encouragement.

As conclusion I would like to remember Bruno Bassetti, the first person who introduced me to the Ising model. I will never forget his passion and enthusiasm.

Bibliography

[1] M. Doi and S. F. Edwards, *The Theory of Polymer Dynamics*. New York: Oxford University Press, 1986.

[2] M. Rubinstein and R. H. Colby, *Polymer Physics*. New York: Oxford University Press, 2003.

[3] O. Kratky and G. Porod, "Röntgenuntersuchung gelöster Fadenmoleküle," *Rec. Trav. Chim. Pays-Bas.*, vol. 68, pp. 1106–1122, 1949.

[4] N. B. Becker, A. Rosa, and R. Everaers, "The radial distribution function of worm-like chains," *Eur. Phys. J. E*, vol. 32, pp. 53–69, 2010.

[5] P. J. Flory, "The configuration of real polymer chains," *The Journal of Chemical Physics*, vol. 17, no. 3, pp. 303–310, 1949.

[6] P. J. Flory, *Principles of Polymer Chemistry*. Ithaca (NY): Cornell University Press, 1953.

[7] S. M. Bhattacharjee, A. Giacometti, and A. Maritan, "Flory theory for polymers," *Journal of Physics: Condensed Matter*, vol. 25, p. 503101, nov 2013.

[8] R. Everaers, A. Y. Grosberg, M. Rubinstein, and A. Rosa, "Flory theory of randomly branched polymers," *Soft Matter*, vol. 13, pp. 1223–1234, 2017.

[9] P.-G. De Gennes, "Reptation of a polymer chain in the presence of fixed obstacles," *J. Chem. Phys.*, vol. 55, pp. 572–579, 1971.

[10] N. Nahali and A. Rosa, "Density effects in entangled solutions of linear and ring polymers," *Journal of Physics: Condensed Matter*, vol. 28, no. 6, p. 065101, 2016.

[11] M. E. Cates and J. M. Deutsch, "Conjectures on the statistics of ring polymers," *J. Phys. (Paris)*, vol. 47, pp. 2121–2128, 1986.

[12] T. Vettorel, A. Y. Grosberg, and K. Kremer, "Territorial polymers," *Phys. Today*, vol. 62, p. 72, 2009.

[13] E. Lieberman-Aiden, N. L. van Berkum, L. Williams, M. Imakaev, T. Ragoczy, A. Telling, I. Amit, B. R. Lajoie, P. J. Sabo, M. O. Dorschner, R. Sandstrom,

B. Bernstein, M. A. Bender, M. Groudine, A. Gnirke, J. Stamatoyannopoulos, L. A. Mirny, E. S. Lander, and J. Dekker, "Comprehensive mapping of long-range interactions reveals folding principles of the human genome," *Science*, vol. 326, no. 5950, pp. 289–293, 2009.

[14] A. R. Khokhlov and S. K. Nechaev, "Polymer chain in an array of obstacles," *Phys. Lett.*, vol. 112A, pp. 156–160, 1985.

[15] A. Y. Grosberg, S. K. Nechaev, and E. I. Shakhnovich, "The role of topological constraints in the kinetics of collapse of macromolecules," *J. Phys. France*, vol. 49, pp. 2095–2100, 1988.

[16] A. Y. Grosberg, Y. Rabin, S. Havlin, and A. Neer, "Crumpled globule model of the three-dimensional structure of DNA," *Europhys. Lett.*, vol. 23, pp. 373–378, 1993.

[17] A. Y. Grosberg, "Annealed lattice animal model and flory theory for the melt of non-concatenated rings: Towards the physics of crumpling," *Soft Matter*, vol. 10, pp. 560–565, 2014.

[18] A. Rosa and R. Everaers, "Ring polymers in the melt state: The physics of crumpling," *Phys. Rev. Lett.*, vol. 112, p. 118302, Mar 2014.

[19] J. Suzuki, A. Takano, T. Deguchi, and Y. Matsushita, "Dimension of ring polymers in bulk studied by Monte-Carlo simulation and self-consistent theory," *J. Chem. Phys.*, vol. 131, p. 144902, 2009.

[20] J. D. Halverson, W. B. Lee, G. S. Grest, A. Y. Grosberg, and K. Kremer, "Molecular dynamics simulation study of nonconcatenated ring polymers in a melt: I. Statics," *J. Chem. Phys.*, vol. 134, p. 204904, 2011.

[21] T. A. Kavassalis and J. Noolandi, "New view of entanglements in dense polymer systems," *Phys. Rev. Lett.*, vol. 59, pp. 2674–2677, 1987.

[22] N. Uchida, G. S. Grest, and R. Everaers, "Viscoelasticity and primitive-path analysis of entangled polymer liquids: from f-actin to polyethilene," *J. Chem. Phys.*, vol. 128, p. 044902, 2008.

[23] A. Rosa and R. Everaers, "Computer simulations of melts of randomly branching polymers," *The Journal of Chemical Physics*, vol. 145, no. 16, p. 164906, 2016.

[24] J. D. Halverson, K. Kremer, and A. Y. Grosberg, "Comparing the results of lattice and off-lattice simulations for the melt of nonconcatenated rings," *J. Phys. A: Math. Theor.*, vol. 46, p. 065002, 2013.

[25] J. Smrek and A. Y. Grosberg, "Minimal Surfaces on Unconcatenated Polymer Rings in Melt," *ACS Macro Lett.*, vol. 5, pp. 750–754, 2016.

[26] W.-C. Lo and M. S. Turner, "The topological glass in ring polymers," *EPL*, vol. 102, no. 5, p. 58005, 2013.

[27] D. Michieletto, D. Marenduzzo, E. Orlandini, G. P. Alexander, and M. S. Turner, "Threading dynamics of ring polymers in a gel," *ACS Macro Lett.*, vol. 3, no. 3, pp. 255–259, 2014.

[28] T. Ge, S. Panyukov, and M. Rubinstein, "Self-similar conformations and dynamics in entangled melts and solutions of nonconcatenated ring polymers," *Macromolecules*, vol. 49, no. 2, pp. 708–722, 2016.

[29] D. Michieletto, "On the tree-like structure of rings in dense solutions," *Soft Matter*, vol. 12, pp. 9485–9500, 2016.

[30] M. Rubinstein, "Dynamics of ring polymers in the presence of fixed obstacles," *Phys. Rev. Lett.*, vol. 57, pp. 3023–3026, Dec 1986.

[31] S. Nechaev, A. Semenov, and M. Koleva, "Dynamics of a polymer chain in an array of obstacles," *Physica A: Statistical Mechanics and its Applications*, vol. 140, no. 3, pp. 506 – 520, 1987.

[32] B. H. Zimm and W. H. Stockmayer, "The dimensions of chain molecules containing branches and rings," *J. Chem. Phys.*, vol. 17, pp. 1301–1314, 1949.

[33] M. Daoud and J. F. Joanny, "Conformation of branched polymers," *J. Physique*, vol. 42, pp. 1359–1371, 1981.

[34] G. Parisi and N. Sourlas, "Critical behavior of branched polymers and the Lee-Yang edge singularity," *Phys. Rev. Lett.*, vol. 46, pp. 871–874, 1981.

[35] P.-G. De Gennes, "Conformation of a polymer chain in certain mixed solvents," *J. Physique Lett.*, vol. 37, pp. L59–L61, 1976.

[36] C. Lanctôt, T. Cheutin, M. Cremer, G. Cavalli, and T. Cremer, "Dynamic genome architecture in the nuclear space: regulation of gene expression in three dimensions," *Nat. Rev. Genet.*, vol. 8, p. 104, 02 2007.

[37] K. J. Meaburn and T. Misteli, "Chromosome territories," *Nature*, vol. 445, pp. 379 EP –, 01 2007.

[38] J. Dekker, M. A. Marti-Renom, and L. A. Mirny, "Exploring the three-dimensional organization of genomes: interpreting chromatin interaction data," *Nat. Rev. Genet.*, vol. 14, pp. 390–403, 2013.

[39] A. Rosa and C. Zimmer, "Computational models of large-scale genome architecture," *Int. Rev. Cell Mol. Biol.*, vol. 307, pp. 275–350, 2014.

[40] J. Dekker, "Chromosome folding: Contributions of chromosome conformation capture and polymer physics," *Modeling the 3D Conformation of Genomes*, 2019.

[41] A. Papale and A. Rosa, "Structure and microrheology of genome organization: From experiments to physical modeling," *Modeling the 3D Conformation of Genomes*, vol. 25, 2019.

[42] B. Alberts, D. Bray, J. D. Watson, J. Lewis, K. Roberts, and M. Raff, *Molecular Biology of the Cell*. New York: Garland Science, 5^{th} ed., 2007.

[43] T. Cremer and C. Cremer, "Chromosome territories, nuclear architecture and gene regulation in mammalian cells," *Nature Rev. Genet.*, vol. 2, pp. 292–301, 2001.

[44] J. C. Hansen, "Conformational dynamics of the chromatin fiber in solution: Determinants, mechanisms, and functions," *Annu. Rev. Biophys. Biomol. Struct.*, vol. 31, no. 1, pp. 361–392, 2002.

[45] V. Ea, M.-O. Baudement, A. Lesne, and T. Forné, "Contribution of topological domains and loop formation to 3d chromatin organization," *Genes*, vol. 6, no. 3, pp. 734–750, 2015.

[46] K. Luger and J. C. Hansen, "Nucleosome and chromatin fiber dynamics," *Curr. Opin. Struct. Biol.*, vol. 15, no. 2, pp. 188 – 196, 2005.

[47] K. Maeshima, R. Imai, T. Hikima, and Y. Joti, "Chromatin structure revealed by x-ray scattering analysis and computational modeling," *Methods*, vol. 70, no. 2, pp. 154–161, 2014.

[48] K. Maeshima, S. Ide, K. Hibino, and M. Sasai, "Liquid-like behavior of chromatin," *Curr. Opin. Genet. Dev.*, vol. 37, no. Supplement C, pp. 36–45, 2016.

[49] H. D. Ou, S. Phan, T. J. Deerinck, A. Thor, M. H. Ellisman, and C. C. O'Shea, "Chromemt: Visualizing 3d chromatin structure and compaction in interphase and mitotic cells," *Science*, vol. 357, no. 6349, 2017.

[50] V. Récamier, I. Izeddin, L. Bosanac, M. Dahan, F. Proux, and X. Darzacq, "Single cell correlation fractal dimension of chromatin," *Nucleus*, vol. 5, pp. 75–84, 01 2014.

[51] A. Bolzer, G. Kreth, I. Solovei, D. Koehler, K. Saracoglu, C. Fauth, S. Muller, R. Eils, C. Cremer, M. Speicher, and T. Cremer, "Three-dimensional maps of all chromosomes in human male fibroblast nuclei and prometaphase rosettes," *Plos Biol.*, vol. 3, no. 5, pp. 826–842, 2005.

[52] A. Vivante, E. Brozgol, I. Bronshtein, L. Vered, and Y. Garini, "Chromatin dynamics governed by a set of nuclear structural proteins," *Genes, Chromosomes and Cancer*, vol. 58, no. 7, pp. 437–451, 2019.

[53] J. R. Dixon, S. Selvaraj, F. Yue, A. Kim, Y. Li, Y. Shen, M. Hu, J. S. Liu, and B. Ren, "Topological domains in mammalian genomes identified by analysis of chromatin interactions," *Nature*, vol. 485, no. 7398, pp. 376–380, 2012.

[54] J. Dekker, K. Rippe, M. Dekker, and N. Kleckner, "Capturing chromosome conformation," *Science*, vol. 295, p. 1306, 2002.

[55] D. Jost, C. Vaillant, and P. Meister, "Coupling 1d modifications and 3d nuclear organization: data, models and function," *Curr. Opin. Cell Biol.*, vol. 44, pp. 20–27, 2 2017.

[56] J. R. Dixon, I. Jung, S. Selvaraj, Y. Shen, J. E. Antosiewicz-Bourget, A. Y. Lee, Z. Ye, A. Kim, N. Rajagopal, W. Xie, Y. Diao, J. Liang, H. Zhao, V. V. Lobanenkov, J. R. Ecker, J. A. Thomson, and B. Ren, "Chromatin architecture reorganization during stem cell differentiation," *Nature*, vol. 518, no. 7539, pp. 331–336, 2015.

[57] N. Lonfat, T. Montavon, F. Darbellay, S. Gitto, and D. Duboule, "Convergent evolution of complex regulatory landscapes and pleiotropy at *Hox* loci," *Science*, vol. 346, no. 6212, p. 1004, 2014.

[58] A.-L. Valton and J. Dekker, "Tad disruption as oncogenic driver," *Current opinion in genetics & development*, vol. 36, pp. 34–40, 02 2016.

[59] K. Bystricky, P. Heun, L. Gehlen, J. Langowski, and S. M. Gasser, "Long-range compaction and flexibility of interphase chromatin in budding yeast analyzed by high-resolution imaging techniques," *Proc. Natl. Acad. Sci. USA*, vol. 101, pp. 16495–16500, 2004.

[60] R. K. Sachs, G. van den Engh, B. Trask, H. Yokota, and J. E. Hearst, "A random-walk/giant-loop model for interphase chromosomes," *Proc. Natl. Acad. Sci. USA*, vol. 92, pp. 2710–2714, 1995.

[61] J. Mateos-Langerak *et al.*, "Spatially confined folding of chromatin in the interphase nucleus," *Proc. Natl. Acad. Sci. USA*, vol. 106, pp. 3812–3817, 2009.

[62] D. Jost, A. Rosa, C. Vaillant, and R. Everaers, "A polymer physics view on universal and sequence-specific aspects of chromosome folding," in *Nuclear Architecture and Dynamics, Volume 2* (C. Lavelle and J.-M. Victor, eds.), Academic Press, 2017.

[63] L. A. Mirny, "The fractal globule as a model of chromatin architecture in the cell," *Chromosome Res.*, vol. 19, no. 1, pp. 37–51, 2011.

[64] D. Jost, P. Carrivain, G. Cavalli, and C. Vaillant, "Modeling epigenome folding: formation and dynamics of topologically associated chromatin domains," *Nucleic Acids Research*, vol. 42, no. 15, pp. 9553–9561, 2014.

[65] J. D. Olarte-Plata, N. Haddad, C. Vaillant, and D. Jost, "The folding landscape of the epigenome," *Physical Biology*, vol. 13, no. 2, p. 026001, 2016.

[66] G. Tiana, A. Amitai, T. Pollex, T. Piolot, D. Holcman, E. Heard, and L. Giorgetti, "Structural fluctuations of the chromatin fiber within topologically associating domains," *Biophysical Journal*, vol. 110, no. 6, pp. 1234 – 1245, 2016.

[67] L. J. Fetters, D. J. Lohse, D. Richter, T. A. Witten, and A. Zirkel, "Connections between polymer molecular weight, density, chain dimensions, and melt viscoelastic properties," *Macromolecules*, vol. 27, pp. 4639–4647, 1994.

[68] A.-M. Florescu, P. Therizols, and A. Rosa, "Large scale chromosome folding is stable against local changes in chromatin structure," *Plos. Comput. Biol.*, vol. 12, p. e1004987, 06 2016.

[69] A. Rosa and R. Everaers, "Structure and dynamics of interphase chromosomes," *PLOS Computational Biology*, vol. 4, pp. 1–10, 08 2008.

[70] M. Emanuel, N. H. Radja, A. Henriksson, and H. Schiessel, "The physics behind the larger scale organization of dna in eukaryotes," *Phys. Biol.*, vol. 6, no. 2, p. 025008, 2009.

[71] J. D. Halverson, J. Smrek, K. Kremer, and A. Y. Grosberg, "From a melt of rings to chromosome territories: the role of topological constraints in genome folding.," *Rep. Prog. Phys.*, vol. 77, no. 2, p. 022601, 2014.

[72] A. M. Chiariello, C. Annunziatella, S. Bianco, A. Esposito, and M. Nicodemi, "Polymer physics of chromosome large-scale 3d organisation.," *Sci. Rep.*, vol. 6, p. 29775, 2016.

[73] C. A. Brackley, J. Johnson, S. Kelly, P. R. Cook, and D. Marenduzzo, "Simulated binding of transcription factors to active and inactive regions folds human chromosomes into loops, rosettes and topological domains.," *Nucleic Acids Res.*, vol. 44, pp. 3503–3512, May 2016.

[74] A. Rosa, N. B. Becker, and R. Everaers, "Looping probabilities in model interphase chromosomes," *Biophys. J.*, vol. 98, pp. 2410–2419, 2010.

[75] A. Louis, P. Bolhuis, J. Hansen, and E. Meijer, "Can polymer coils be modeled as "soft colloids"?," *Phys. Rev. Lett.*, vol. 85, pp. 2522–2525, 2000.

[76] M. R. Branco and A. Pombo, "Intermingling of chromosome territories in interphase suggests role in translocations and transcription-dependent associations," *Plos Biol.*, vol. 4, no. 5, p. e138, 2006.

[77] R. Cortini, M. Barbi, B. R. Caré, C. Lavelle, A. Lesne, J. Mozziconacci, and J.-M. Victor, "The physics of epigenetics," *Rev. Mod. Phys.*, vol. 88, p. 025002, Apr 2016.

[78] D. Jost and C. Vaillant, "Epigenomics in 3d: importance of long-range spreading and specific interactions in epigenomic maintenance," *Nucleic Acids Research*, vol. 46, no. 5, pp. 2252–2264, 2018.

[79] G. J. Filion, J. G. van Bemmel, U. Braunschweig, W. Talhout, J. Kind, L. D. Ward, W. Brugman, I. J. de Castro, R. M. Kerkhoven, H. J. Bussemaker, and B. van Steensel, "Systematic protein location mapping reveals five principal chromatin types in drosophila cells," *Cell*, vol. 143, no. 2, pp. 212 – 224, 2010.

[80] M. Wigler, D. Levy, and M. Perucho, "The somatic replication of dna methylation," *Cell*, vol. 24, no. 1, pp. 33 – 40, 1981.

[81] R. Lister, M. Pelizzola, R. H. Dowen, R. D. Hawkins, G. Hon, J. Tonti-Filippini, J. R. Nery, L. Lee, Z. Ye, Q.-M. Ngo, L. Edsall, J. Antosiewicz-Bourget, R. Stewart, V. Ruotti, A. H. Millar, J. A. Thomson, B. Ren, and J. R. Ecker, "Human dna methylomes at base resolution show widespread epigenomic differences," *Nature*, vol. 462, no. 7271, pp. 315–322, 2009.

[82] P. A. Jones, "Functions of dna methylation: islands, start sites, gene bodies and beyond," *Nature Reviews Genetics*, vol. 13, pp. 484 EP –, 05 2012.

[83] J. D. McGhee and G. D. Ginder, "Specific dna methylation sites in the vicinity of the chicken β-globin genes," *Nature*, vol. 280, no. 5721, pp. 419–420, 1979.

[84] A. Razin and H. Cedar, "Dna methylation and gene expression," *Microbiological reviews*, vol. 55, pp. 451–458, 09 1991.

[85] T. Mohandas, R. Sparkes, and L. Shapiro, "Reactivation of an inactive human x chromosome: evidence for x inactivation by dna methylation," *Science*, vol. 211, no. 4480, pp. 393–396, 1981.

[86] L. Venolia, S. M. Gartler, E. R. Wassman, P. Yen, T. Mohandas, and L. J. Shapiro, "Transformation with dna from 5-azacytidine-reactivated x chromosomes," *Proceedings of the National Academy of Sciences*, vol. 79, no. 7, pp. 2352–2354, 1982.

[87] E. Li, C. Beard, and R. Jaenisch, "Role for dna methylation in genomic imprinting," *Nature*, vol. 366, no. 6453, pp. 362–365, 1993.

[88] R. K. Chodavarapu, S. Feng, Y. V. Bernatavichute, P.-Y. Chen, H. Stroud, Y. Yu, J. A. Hetzel, F. Kuo, J. Kim, S. J. Cokus, D. Casero, M. Bernal, P. Huijser, A. T. Clark, U. Krämer, S. S. Merchant, X. Zhang, S. E. Jacobsen, and M. Pellegrini, "Relationship between nucleosome positioning and dna methylation," *Nature*, vol. 466, no. 7304, pp. 388–392, 2010.

[89] J. Y. Lee and T.-H. Lee, "Effects of dna methylation on the structure of nucleosomes," *Journal of the American Chemical Society*, vol. 134, pp. 173–175, 01 2012.

[90] J. S. Choy, S. Wei, J. Y. Lee, S. Tan, S. Chu, and T.-H. Lee, "Dna methylation increases nucleosome compaction and rigidity," *Journal of the American Chemical Society*, vol. 132, pp. 1782–1783, 02 2010.

[91] B. Fierz, "Synthetic chromatin approaches to probe the writing and erasing of histone modifications," *ChemMedChem*, vol. 9, no. 3, pp. 495–504, 2014.

[92] A. Papale and A. Rosa, "The ising model in swollen vs. compact polymers: Mean-field approach and computer simulations," *The European Physical Journal E*, vol. 41, p. 144, Dec 2018.

[93] T. Sexton *et al.*, "Three-dimensional folding and functional organization principles of the drosophila genome.," *Cell*, vol. 148, no. 3, pp. 458–472, 2012.

[94] D. Jost, "Bifurcation in epigenetics: Implications in development, proliferation, and diseases," *Phys. Rev. E*, vol. 89, p. 010701, Jan 2014.

[95] W. Lenz, "Beitrage zum verständnis der magnetischen eigenschaften in festen korpern," *Physikalische Zeitschrift*, vol. 21, pp. 613–615, 1920.

[96] E. Ising, "Beitrag zur theorie des ferromagnetismus," *Zeitschrift für Physik*, vol. 31, no. 1, pp. 253–258, 1925.

[97] S. G. Brush, "History of the lenz-ising model," *Rev. Mod. Phys.*, vol. 39, pp. 883–893, Oct 1967.

[98] K. Huang, *Statistical Mechanics*. John Wiley & Sons, 2 ed., 1987.

[99] M. Mezard, G. Parisi, and M. Virasoro, *Spin Glass Theory and Beyond*. Lecture Notes in Physics Series, World Scientific, 1987.

[100] J. J. Hopfield, "Neural networks and physical systems with emergent collective computational abilities," *Proceedings of the National Academy of Sciences*, vol. 79, no. 8, pp. 2554–2558, 1982.

[101] C. Schinckus, "Ising model, econophysics and analogies," *Physica A*, vol. 508, pp. 95–103, 2018.

[102] S. R. A. Salinas, *The Ising Model*, pp. 257–276. New York, NY: Springer New York, 2001.

[103] T. D. Lee and C. N. Yang, "Statistical theory of equations of state and phase transitions. ii. lattice gas and ising model," *Phys. Rev.*, vol. 87, pp. 410–419, Aug 1952.

[104] L. Onsager, "Crystal statistics. i. a two-dimensional model with an order-disorder transition," *Phys. Rev.*, vol. 65, pp. 117–149, Feb 1944.

[105] B. K. Chakrabarti and S. Bhattacharya, "Study of an ising model on a self-avoiding-walk lattice," *Journal of Physics C: Solid State Physics*, vol. 16, no. 29, p. L1025, 1983.

[106] S. Bhattacharya and B. K. Chakrabarti, "Ising model on self-avoiding walk chains," *Zeitschrift für Physik B Condensed Matter*, vol. 57, pp. 151–155, Oct 1984.

[107] B. K. Chakrabarti and S. Bhattacharya, "A real space renormalisation group study of the ising model on self-avoiding walk chains," *Journal of Physics A: Mathematical and General*, vol. 18, no. 6, p. 1037, 1985.

[108] B. K. Chakrabarti, A. C. Maggs, and R. B. Stinchcombe, "Ising model on a self-avoiding walk," *Journal of Physics A: Mathematical and General*, vol. 18, no. 7, p. L373, 1985.

[109] T. Garel, H. Orland, and E. Orlandini, "Phase diagram of magnetic polymers," *The European Physical Journal B - Condensed Matter and Complex Systems*, vol. 12, pp. 261–268, Nov 1999.

[110] S. P. Obukhov, M. Rubinstein, and T. Duke, "Dynamics of a ring polymer in a gel," *Phys. Rev. Lett.*, vol. 73, pp. 1263–1266, 1994.

[111] J. D. Halverson, J. Smrek, K. Kremer, and A. Y. Grosberg, "From a melt of rings to chromosome territories: the role of topological constraints in genome folding," *Rep. Prog. Phys.*, vol. 77, p. 022601, 2014.

[112] A. Colliva, R. Pellegrini, A. Testori, and M. Caselle, "Ising-model description of long-range correlations in dna sequences," *Phys. Rev. E*, vol. 91, p. 052703, May 2015.

[113] M. Aertsens and C. Vanderzande, "The ising model on a saw," *Journal of Physics A: Mathematical and General*, vol. 25, no. 4, p. 735, 1992.

[114] N. Goldenfeld, *Lectures on phase transitions and the renormalization group*. Addison-Wesley, 1992.

[115] A. Rosa and R. Everaers, "Beyond flory theory: Distribution functions for interacting lattice trees," *Phys. Rev. E*, vol. 95, p. 012117, Jan 2017.

[116] A. Rosa and R. Everaers, "Conformational statistics of randomly branching double-folded ring polymers," *The European Physical Journal E*, vol. 42, p. 7, Jan 2019.

[117] N. Madras and A. D. Sokal, "The pivot algorithm: A highly efficient monte carlo method for the self-avoiding walk," *Journal of Statistical Physics*, vol. 50, pp. 109–186, Jan 1988.

[118] A. Rosa and R. Everaers, "Computer simulations of randomly branching polymers: annealed versus quenched branching structures," *J. Phys. A: Math. Theor.*, vol. 49, p. 345001, 2016.

[119] U. Wolff, "Collective monte carlo updating for spin systems," *Phys. Rev. Lett.*, vol. 62, pp. 361–364, Jan 1989.

[120] W. Krauth, *Statistical Mechanics Algorithms and Computations*. Oxford: Oxford University Press, 2006.

[121] M. Bishop and J. P. J. Michels, "Scaling in three-dimensional linear and ring polymers," *J. Chem. Phys.*, vol. 84, pp. 444–446, 1986.

[122] D. Wirtz, "Particle-tracking microrheology of living cells: Principles and applications," *Annu. Rev. Biophys.*, vol. 38, pp. 301–326, 2009.

[123] Y. Tseng, J. S. H. Lee, T. P. Kole, I. Jiang, and D. Wirtz, "Micro-organization and visco-elasticity of the interphase nucleus revealed by particle nanotracking," *Journal of Cell Science*, vol. 117, no. 10, pp. 2159–2167, 2004.

[124] P. Cicuta and A. M. Donald, "Microrheology: a review of the method and applications," *Soft Matter*, vol. 3, pp. 1449–1455, 2007.

[125] P.-H. Wu, C. M. Hale, W.-C. Chen, J. S. H. Lee, Y. Tseng, and D. Wirtz, "High-throughput ballistic injection nanorheology to measure cell mechanics," *Nat. Protocols*, vol. 7, pp. 155–170, 01 2012.

[126] T. A. Waigh, "Advances in the microrheology of complex fluids," *Rep. Prog. Phys.*, vol. 79, no. 7, p. 074601, 2016.

[127] F. Brochard-Wyart and P.-G. De Gennes, "Viscosity at small scales in polymer melts," *Eur. Phys. J. E*, vol. 1, pp. 93–97, 2000.

[128] L.-H. Cai, S. Panyukov, and M. Rubinstein, "Mobility of nonsticky nanoparticles in polymer liquids," *Macromolecules*, vol. 44, pp. 7853–7863, 10 2011.

[129] L.-H. Cai, S. Panyukov, and M. Rubinstein, "Hopping diffusion of nanoparticles in polymer matrices," *Macromolecules*, vol. 48, pp. 847–862, 2015.

[130] G. Guigas, C. Kalla, and M. Weiss, "Probing the nanoscale viscoelasticity of intracellular fluids in living cells," *Biophys. J.*, vol. 93, no. 1, pp. 316–323, 2007.

[131] F. M. Hameed, M. Rao, and G. Shivashankar, "Dynamics of passive and active particles in the cell nucleus," *Plos One*, vol. 7, no. 10, p. e45843, 2012.

[132] A. M. Puertas and T. Voigtmann, "Microrheology of colloidal systems," *J. Phys.-Condens. Matter*, vol. 26, no. 24, p. 243101, 2014.

[133] R. Metzler, J.-H. Jeon, A. G. Cherstvy, and E. Barkai, "Anomalous diffusion models and their properties: non-stationarity, non-ergodicity, and ageing at the centenary of single particle tracking," *Phys. Chem. Chem. Phys.*, vol. 16, pp. 24128–24164, 2014.

[134] M. J. Saxton, "Anomalous diffusion due to obstacles: a monte carlo study.," *Biophys. J.*, vol. 66, pp. 394–401, 1994.

[135] J.-P. Bouchaud and A. Georges, "Anomalous diffusion in disordered media: Statistical mechanisms, models and physical applications," *Phys. Rep.*, vol. 195, no. 4, pp. 127–293, 1990.

[136] T. G. Mason and D. A. Weitz, "Optical measurements of frequency-dependent linear viscoelastic moduli of complex fluids," *Phys. Rev. Lett.*, vol. 74, pp. 1250–1253, 1995.

[137] S. M. Gasser, "Nuclear architecture - Visualizing chromatin dynamics in interphase nuclei," *Science*, vol. 296, pp. 1412–1416, 2002.

[138] K. Bystricky, "Chromosome dynamics and folding in eukaryotes: Insights from live cell microscopy," *FEBS Lett.*, vol. 589, no. 20, Part A, pp. 3014–3022, 2015.

[139] I. Bronshtein, I. Kanter, E. Kepten, M. Lindner, S. Berezin, Y. Shav-Tal, and Y. Garini, "Exploring chromatin organization mechanisms through its dynamic properties," *Nucleus*, vol. 7, no. 1, pp. 27–33, 2016.

[140] S. C. Weber, A. J. Spakowitz, and J. A. Theriot, "Nonthermal atp-dependent fluctuations contribute to the in vivo motion of chromosomal loci," *Proceedings of the National Academy of Sciences*, vol. 109, no. 19, pp. 7338–7343, 2012.

[141] A. Zidovska, D. A. Weitz, and T. J. Mitchison, "Micron-scale coherence in interphase chromatin dynamics," *Proc. Natl. Acad. Sci. USA*, vol. 110, pp. 15555–15560, 09 2013.

[142] D. Marenduzzo, K. Finan, and P. R. Cook, "The depletion attraction: an underappreciated force driving cellular organization," *J. Cell Biol.*, vol. 175, no. 5, pp. 681–686, 2006.

[143] S. Huet, C. Lavelle, H. Ranchon, P. Carrivain, J.-M. Victor, A. Bancaud, R. Hancock, and K. W. Jeon, "Relevance and limitations of crowding, fractal, and polymer models to describe nuclear architecture," *Int. Rev. Cell Mol. Biol.*, vol. 307, pp. 443–479, 2014.

[144] H. Hajjoul, J. Mathon, H. Ranchon, I. Goiffon, J. Mozziconacci, B. Albert, P. Carrivain, J.-M. Victor, O. Gadal, K. Bystricky, and A. Bancaud, "High-throughput chromatin motion tracking in living yeast reveals the flexibility of the fiber throughout the genome," *Genome Res.*, vol. 23, pp. 1829–1838, 2013.

[145] T. Ge, J. T. Kalathi, J. D. Halverson, G. S. Grest, and M. Rubinstein, "Nanoparticle motion in entangled melts of linear and nonconcatenated ring polymers," *Macromolecules*, vol. 50, no. 4, pp. 1749–1754, 2017.

[146] N. Nahali and A. Rosa, "Nanoprobe diffusion in entangled polymer solutions: Linear vs. unconcatenated ring chains," *The Journal of Chemical Physics*, vol. 148, no. 19, p. 194902, 2018.

[147] S. P. Obukhov, M. Rubinstein, and T. Duke, "Dynamics of a ring polymer in a gel," *Phys. Rev. Lett.*, vol. 73, pp. 1263–1266, 1994.

[148] J. Smrek and A. Y. Grosberg, "Understanding the dynamics of rings in the melt in terms of the annealed tree model," *J. Phys.-Condens. Matter*, vol. 27, no. 6, p. 064117, 2015.

[149] A. Papale and A. Rosa, "Microrheology of interphase chromosomes with spatial constraints: a computational study," *Physical Biology*, vol. 16, p. 066002, sep 2019.

[150] M. Valet and A. Rosa, "Viscoelasticity of model interphase chromosomes," *The Journal of Chemical Physics*, vol. 141, no. 24, p. 245101, 2014.

[151] Y. Tseng, T. P. Kole, S.-H. J. Lee, and D. Wirtz, "Local dynamics and viscoelastic properties of cell biological systems," *Curr. Opin. Colloid In.*, vol. 7, no. 3, pp. 210–217, 2002.

[152] M. Carmo-Fonseca, M. Platani, and J. R. Swedlow, "Macromolecular mobility inside the cell nucleus," *Trends Cell Biol.*, vol. 12, no. 11, pp. 491–495, 2002.

[153] M. Platani, I. G. Goldberg, D. Bensaddek, and J. R. Swedlow, "Cajal body dynamics and association with chromatin are atp-dependent," *Nat. Cell Biol.*, vol. 4, pp. 502–508, 2002.

[154] S. M. Görisch, M. Wachsmuth, C. Ittrich, C. P. Bacher, K. Rippe, and P. Lichter, "Nuclear body movement is determined by chromatin accessibility and dynamics," *Proc. Natl. Acad. Sci. USA*, vol. 101, no. 36, pp. 13221–13226, 2004.

[155] D. K. Sinha, B. Banerjee, S. Maharana, and G. V. Shivashankar, "Probing the dynamic organization of transcription compartments and gene loci within the nucleus of living cells," *Biophys. J.*, vol. 95, no. 11, pp. 5432–5438, 2008.

[156] N. G. Van Kampen, *Stochastic Processes in Physics and Chemistry*. Amsterdam: Elsevier, 3 ed., 2007.

[157] T. Pederson, "Half a century of "the nuclear matrix"," *Mol. Biol. Cell*, vol. 11, no. 3, pp. 799–805, 2000.

[158] S. A. Adam, "The nucleoskeleton," *Cold Spring Harb. Perspect. Biol.*, vol. 9, no. 2, p. a023556, 2017.

[159] S. S. P. Rao *et al.*, "A 3d map of the human genome at kilobase resolution reveals principles of chromatin looping," *Cell*, vol. 159, no. 7, pp. 1665–80, 2014.

[160] A. Pombo and N. Dillon, "Three-dimensional genome architecture: players and mechanisms," *Nat. Rev. Mol. Cell Biol.*, vol. 16, pp. 245–257, 2015.

[161] J. Kind, L. Pagie, S. S. de Vries, L. Nahidiazar, S. S. Dey, M. Bienko, Y. Zhan, B. Lajoie, C. A. de Graaf, M. Amendola, G. Fudenberg, M. Imakaev, L. A. Mirny, K. Jalink, J. Dekker, A. van Oudenaarden, and B. van Steensel, "Genome-wide maps of nuclear lamina interactions in single human cells," *Cell*, vol. 163, pp. 134–147, 9 2015.

[162] P. R. Cook, "A model for all genomes: The role of transcription factories," *J. Mol. Biol.*, vol. 395, pp. 1–10, 2010.

[163] R.-S. Nozawa and N. Gilbert, "Rna: Nuclear glue for folding the genome," *Trends Cell Biol.*, vol. 29, no. 3, pp. 201–211, 2019.

[164] I. Bronshtein, E. Kepten, I. Kanter, S. Berezin, M. Lindner, A. B. Redwood, S. Mai, S. Gonzalo, R. Foisner, Y. Shav-Tal, and Y. Garini, "Loss of lamin a function increases chromatin dynamics in the nuclear interior," *Nature Communications*, vol. 6, pp. 8044 EP –, 08 2015.

[165] R. P. McCord, A. Nazario-Toole, H. Zhang, P. S. Chines, Y. Zhan, M. R. Erdos, F. S. Collins, J. Dekker, and K. Cao, "Correlated alterations in genome organization, histone methylation, and dna-iamin a/c interactions in hutchinson-gilford progeria syndrome," *Genome Res.*, vol. 23, no. 2, pp. 260–269, 2013.

[166] B. Bonev and G. Cavalli, "Organization and function of the 3d genome," *Nat. Rev. Genet.*, vol. 17, pp. 661–678, 2016.

[167] J. Dekker, A. S. Belmont, M. Guttman, V. O. Leshyk, J. T. Lis, S. Lomvardas, L. A. Mirny, C. C. O'Shea, P. J. Park, B. Ren, J. C. R. Politz, J. Shendure, S. Zhong, and the 4D Nucleome Network, "The 4d nucleome project," *Nature*, vol. 549, no. 7671, pp. 219–226, 2017.

[168] K. Kremer and G. S. Grest, "Dynamics of entangled linear polymer melts: a molecular-dynamics simulation," *The Journal of Chemical Physics*, vol. 92, no. 8, pp. 5057–5086, 1990.

[169] S. Plimpton, "Fast parallel algorithms for short range molecular dynamics," *J. Comp. Phys.*, vol. 117, pp. 1–19, 1995.

[170] L. R. Gehlen, A. Rosa, K. Klenin, J. Langowski, S. M. Gasser, and K. Bystricky, "Spatially confined polymer chains: implications of chromatin fibre flexibility and peripheral anchoring on telomere–telomere interaction," *J. Phys.: Condens. Matter*, vol. 18, no. 14, pp. S245–S252, 2006.

[171] G. Shi, L. Liu, C. Hyeon, and D. Thirumalai, "Interphase human chromosome exhibits out of equilibrium glassy dynamics," *Nat. Commun.*, vol. 9, no. 1, p. 3161, 2018.

[172] S. K. Ghosh and D. Jost, "How epigenome drives chromatin folding and dynamics, insights from efficient coarse-grained models of chromosomes," *Plos Computat. Biol.*, vol. 14, no. 5, p. e1006159, 2018.

[173] T. G. Mason, "Estimating the viscoelastic moduli of complex fluids using the generalized stokes–einstein equation," *Rheologica Acta*, vol. 39, pp. 371–378, Aug 2000.

[174] P. Chaudhuri, L. Berthier, and W. Kob, "Universal nature of particle displacements close to glass and jamming transitions," *Phys. Rev. Lett.*, vol. 99, p. 060604, Aug 2007.

[175] D. Michieletto, N. Nahali, and A. Rosa, "Glassiness and heterogeneous dynamics in dense solutions of ring polymers," *Phys. Rev. Lett.*, vol. 119, p. 197801, Nov 2017.

[176] J.-H. Jeon, M. Javanainen, H. Martinez-Seara, R. Metzler, and I. Vattulainen, "Protein crowding in lipid bilayers gives rise to non-gaussian anomalous lateral diffusion of phospholipids and proteins," *Phys. Rev. X*, vol. 6, p. 021006, 2016.

[177] G. Ozer, A. Luque, and T. Schlick, "The chromatin fiber: multiscale problems and approaches," *Curr. Opin. Struct. Biol.*, vol. 31, pp. 124–139, 2015.

[178] A. Y. Grosberg and J.-F. Joanny, "Nonequilibrium statistical mechanics of mixtures of particles in contact with different thermostats," *Phys. Rev. E*, vol. 92, p. 032118, Sep 2015.

[179] S. N. Weber, C. A. Weber, and E. Frey, "Binary mixtures of particles with different diffusivities demix," *Phys. Rev. Lett.*, vol. 116, p. 058301, Feb 2016.

[180] R. Wittkowski, J. Stenhammar, and M. E. Cates, "Nonequilibrium dynamics of mixtures of active and passive colloidal particles," *New Journal of Physics*, vol. 19, no. 10, p. 105003, 2017.

[181] A. Y. Grosberg and J.-F. Joanny, "Dissipation in a system driven by two different thermostats," *Polymer Science, Series C*, vol. 60, pp. 118–121, Dec 2018.

[182] N. Ganai, S. Sengupta, and G. I. Menon, "Chromosome positioning from activity-based segregation," *Nucleic acids research*, vol. 42, pp. 4145–4159, 04 2014.

[183] A. Awazu, "Segregation and phase inversion of strongly and weakly fluctuating brownian particle mixtures and a chain of such particle mixtures in spherical containers," *Phys. Rev. E*, vol. 90, p. 042308, Oct 2014.

[184] A. Awazu, "Nuclear dynamical deformation induced hetero- and euchromatin positioning," *Phys. Rev. E*, vol. 92, p. 032709, Sep 2015.

[185] G. I. Menon, *Active Matter*, pp. 193–218. New York, NY: Springer New York, 2010.

[186] M. C. Marchetti, J. F. Joanny, S. Ramaswamy, T. B. Liverpool, J. Prost, M. Rao, and R. A. Simha, "Hydrodynamics of soft active matter," *Rev. Mod. Phys.*, vol. 85, pp. 1143–1189, Jul 2013.

[187] G. De Magistris and D. Marenduzzo, "An introduction to the physics of active matter," *Physica A*, vol. 418, pp. 65–77, 2015.

[188] T. Vicsek, A. Czirók, E. Ben-Jacob, I. Cohen, and O. Shochet, "Novel type of phase transition in a system of self-driven particles," *Phys. Rev. Lett.*, vol. 75, pp. 1226–1229, Aug 1995.

[189] P. Romanczuk, M. Bär, W. Ebeling, B. Lindner, and L. Schimansky-Geier, "Active brownian particles," *The European Physical Journal Special Topics*, vol. 202, no. 1, pp. 1–162, 2012.

[190] A. P. Solon, M. E. Cates, and J. Tailleur, "Active brownian particles and run-and-tumble particles: A comparative study," *The European Physical Journal Special Topics*, vol. 224, pp. 1231–1262, Jul 2015.

[191] R. G. Winkler, J. Elgeti, and G. Gompper, "Active polymers —emergent conformational and dynamical properties: A brief review," *J. Phys. Soc. Jpn.*, vol. 86, no. 10, p. 101014, 2017.

[192] J. Smrek and K. Kremer, "Small activity differences drive phase separation in active-passive polymer mixtures," *Phys. Rev. Lett.*, vol. 118, p. 098002, Mar 2017.

[193] J. Smrek and K. Kremer, "Interfacial properties of active-passive polymer mixtures," *Entropy*, vol. 20, no. 7, p. 520, 2018.

[194] G. Kreth, J. Finsterle, J. von Hase, M. Cremer, and C. Cremer, "Radial arrangement of chromosome territories in human cell nuclei: A computer model approach based on gene density indicates a probabilistic global positioning code," *Biophysical Journal*, vol. 86, no. 5, pp. 2803 – 2812, 2004.

[195] A. Goloborodko, J. F. Marko, and L. A. Mirny, "Chromosome compaction by active loop extrusion.," *Biophys. J.*, vol. 110, no. 10, pp. 2162–2168, 2016.

[196] T. Ge, G. S. Grest, and M. Rubinstein, "Nanorheology of entangled polymer melts," *Phys. Rev. Lett.*, vol. 120, p. 057801, Feb 2018.

[197] R. Everaers and M. R. Ejtehadi, "Interaction potentials for soft and hard ellipsoids," *Phys. Rev. E*, vol. 67, p. 041710, Apr 2003.

[198] W. A. Seitz and D. J. Klein, "Excluded volume effects for branched polymers," *J. Chem. Phys.*, vol. 75, pp. 5190–5193, 1981.